공학박사 학위논문

Synthesis, Characterization, and Application of Microporous Layered Silicate AMH-3 with Selective Ion Exchange and Transport Properties

선택적 이온 교환 및 투과 특성을 지닌 미세다공성 층상실리케이트 AMH-3의 합성, 특성 분석 및 응용에 관한 연구

2018년 2월

서울대학교 대학원

재료공학부

김 지 훈

ABSTRACT

Microporous materials have been attracting great interest because of their ability to interact with atoms, ions and molecules not only at their surfaces, but throughout the bulk of the material. The utility of microporous materials is manifested in their microstructures (pore size, distribution, shape, volume), which allow molecules access to large internal surfaces and cavities that enhance catalytic activity and adsorptive capacity. Owing to this structures, microporous materials are widely used in various applications such as catalysts, adsorbents, molercular sieves.

AMH-3 is a layered microporous material constructed from silicate layers and interlayer spaces occupied by strontium cations, sodium cations, and water molecules. AMH-3 is the first layered silicate with micoroporosity through eight-membered ring (8-MR) apertures along the thickness of the silicate layer as well as in the plane of the layers. Because of this unique structure, AMH-3 has three-dimensional ordered microporosity and good acid, chemical and thermal stability like zeolite and provides the ability for intercalation, pillaring, and exfoliation like layered silicate.

Synthesis and characterization of AMH-3 and its synthesis mechanism study were conducted. Field emission scanning electron microscopy (FE-SEM), X-ray diffraction (XRD), ^{29}Si magic angle spinning nuclear magnetic

resonance (MAS NMR), fourier transform infrared (FT-IR), and Raman spectroscopy were used to characterize AMH-3. A reasonable model for the synthesis mechanism of AMH-3 is proposed on the basis of experiment results. In the synthesis process, strontium and titanium act as structuring agent and assembly agent, respectively.

The ion exchange behavior of AMH-3 and the removal of heavy metals present in aqueous solutions by AMH-3 are investigated for the first time. Pristine AMH-3 and ion-exchanged AMH-3 were characterized with ICP-AES, FE-SEM, ^{29}Si CP MAS NMR and XRD. The studies on ion exchange behavior reveal that the sorption of ion by AMH-3 was found to be governed by ion exchange rather than surface adsorption, and no significant change occurred in the structure of the AMH-3 during the ion exchange. The removal of various heavy metal ions (Pb^{2+}, Cu^{2+}, Cd^{2+}, and Zn^{2+}) onto AMH-3 from aqueous solutions was conducted using a batch method. The effects of influential parameters, such as the initial metal ion concentration and contact time, on the sorption process were studied. The heavy metal ion sorption capacity and removal efficiency were mainly dependent on the difference between the effective pore size of the AMH-3 and the hydrated radius of the metal ion. The sorption isotherm data were well fitted by Langmuir (for Pb^{2+}, Cu^{2+}, and Zn^{2+}) and Freundlich (for Cd^{2+}) models. The sorption kinetics data were well fitted by a pseudo-second order kinetic model. Competitive

sorption experiments revealed an order of metal ion affinity of Pb^{2+} > $Cu2^{+}$> Zn^{2+} > Cd^{2+}. These findings indicate that AMH-3 is suitable for the efficient and selective removal of heavy metals from aqueous solutions.

In order to use as permselective barrier, the removal of the Na^{+} and Sr^{2+} cations located in the intralayer and interlayer spaces for activation of micropores and the delamination of an individual layer must be carried out. We successfully obtained delaminated AMH-3 by acid-hydrothermal treatment without the use of swelling agent. The post-treatment conditions have been optimized to find the best morphology for use as permselective barrier. The pristine AMH-3 and the delaminated AMH-3 were characterized with FE-SEM, N_2 adsorption, ICP-AES, ^{29}Si MAS NMR, FT-IR, Raman and XRD analyses. These results show that the delaminated AMH-3 has a more ordered pore structure than the pristine AMH-3 and that it retains framework crystallinity in the AMH-3 layers.

Utilizing AMH-3 with activated micropores, we sought to develop ion exchange membranes that have low vanadium crossover for use in vanadium redox flow batteries (VRBs). Nafion-based composite membrane containing delaminated AMH-3 (D-AMH-3) layer was prepared by solution casting and hot pressing. The membrane structure was analyzed by FE-SEM and EDS, revealing a sandwich-type structure that included double Nafion outer layers

and a central D-AMH-3 layer. The Nafion/DAMH-3 membrane was employed as an ion exchange membrane for VRB application, and the vanadium permeability and single cell performance were evaluated. The Nafion/D-AMH-3membrane exhibited a lowerVO^{2+} permeability compared to Nafion, resulting in higher Coulombic efficiency and lower capacity loss per cycle. The results indicated that D-AMH-3 layer is potentially suitable as a permselective barrier for reducing vanadium crossover and improving cell performance.

Sulfonated poly(ether ether ketone) (SPEEK) is a potential polymer for replacing Nafion in VRBs. However, at a high degree of sulfonation, SPEEK displays high swelling, poor mechanical stability, and high vanadium crossover. In this study, to improve membrane performance, composite membranes of SPEEK and ultrasonicated D-AMH-3 (U-AMH-3) are prepared with various U-AMH-3 contents and investigated. The physicochemical and mechanical properties, vanadium permeability, and VRB single cell performance of these SPEEK/U-AMH-3 composite membranes are evaluated using various characterization techniques. Interactions between SPEEK and U-AMH-3, and the permselective property of U-AMH-3, result in the composite membranes exhibiting good mechanical properties and low vanadium crossover. Optimal composite membranes gave a VRB that produced a higher charge–discharge capacity, higher cell efficiency, and

better capacity retention than that using Nafion. These results indicate that SPEEK-based composite membranes with improved membrane performance, lower vanadium crossover, and good single cell performance were successfully prepared by incorporating U-AMH-3.

Keywords: Microporous, Layered silicate, AMH-3, Ion exchange, Sorbent, Heavy metal ion, Ion transport, Vanadium redox flow battery

Student Number: 2008-22839

CONTENTS

LIST OF TABLES

LIST OF FIGURES

CHAPTER I

INTRODUCTION

I-1. Microporous materials

Porous materials are classified into several kinds by their pore size. According to IUPAC notation, microporous materials have pore diameters of less than 2 nm, mesoporous materials have pore diameters between 2 nm and 50 nm and macroporous materials have pore diameters of greater than 50 nm. Porous materials have been attracting great interest because of their ability to interact with atoms, ions and molecules not only at their surfaces, but throughout the bulk of the material. The utility of porous materials is manifested in their microstructures (pore size, distribution, shape, volume), which allow molecules access to large internal surfaces and cavities that enhance catalytic activity and adsorptive capacity [1]. Of the porous materials, the microporous materials can act as molecular sieves. Selective permeation of molecule can be achieved using microporous materials. Heterogeneous catalysis and adsorption processes make extensive use of microporous materials.

I-1-1. Aluminosilicates (zeolites)

Zeolites are the most prominent group of microporous materials. Zeolites are crystalline aluminosilicates with three dimensional microporous structures built of tetrahedra of SiO_4 and TO_4 (T=Al, Ti, etc.), which link to each other by sharing all the oxygen atoms to form regular pores and channels [2]. Substitution of Al for Si generates a charge imbalance, necessitating the inclusion of a cation. Owing to this structures, zeolites are widely used in various applications such as catalysts, adsorbents, molercular sieves [3].

There are two types of structures of zeolites [3]: one provides an internal pore system comprising interconnected cage-like voids; the second provides a system of uniform channels which, in some instances, are one-dimensional and in others intersect with similar channels to produce two- or three-dimensional channel systems. The two- or three-dimensional channel systems provide rapid intracrystalline diffusion, which is advantageous in adsorption and catalytic applications. The central elements of the tetrahedra in the zeolite framework can be substituted in an isomorphous manner by other tri- and tetravalent elements [4]. The trivalent elements ,such as B, Fe, Cr, Ga, etc. can be replaced into the framework instead of Al, and the tetravalent elements, such as Ge, Ti, Zr, etc., can be replaced instead of Si. The nature and the

extent of substitution of the isomorphous replacement affect the catalytic properties of zeolites.

According to the International Zeolite Association's database of July 2017, there are 235 different types of zeolite framework structures. The nomenclature of zeolites is often confusing, in spite of the fact that the International Zeolite Association has assigned a three-letter code to each structure type (Figure I-1). A typical example would be FAU, which represents the family of materials with the faujasite-type structure. Zeolites also can be distinguished by their pore sizes (small, medium, and large-pore zeolites) as shown in Figure I-2 and Table I-1 [4]. The large-pore zeolites, such as Y and ZSM-12, are formed by twelve-membered rings (12-MRs) and their pore diameter is about 7.4 Å. The medium-pore pentasil zeolites, exemplified by ZSM-5, ZSM-11, and ZSM-22, have a 10-MRs with an ellipsoidal tubular diameter of 5.5 × 5.6 Å. The structural assembly of uniform channels is an advantageous special feature of the pentasil zeolites (Figure I-3). In the case of small-pore zeolites, eight tetrahedra form a ring of diameter 4.1 Å.

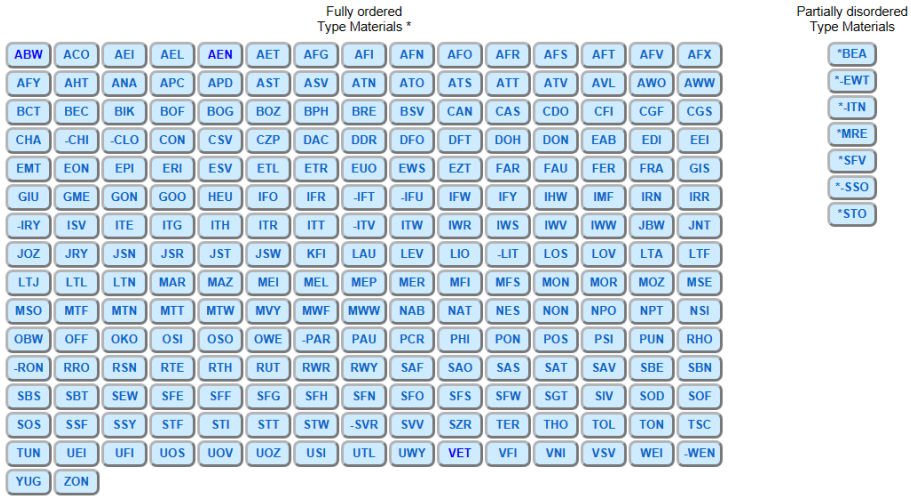

Figure I-1. Zeolite framework types assigned by international zeolite association. (http://www.iza-structure.org)

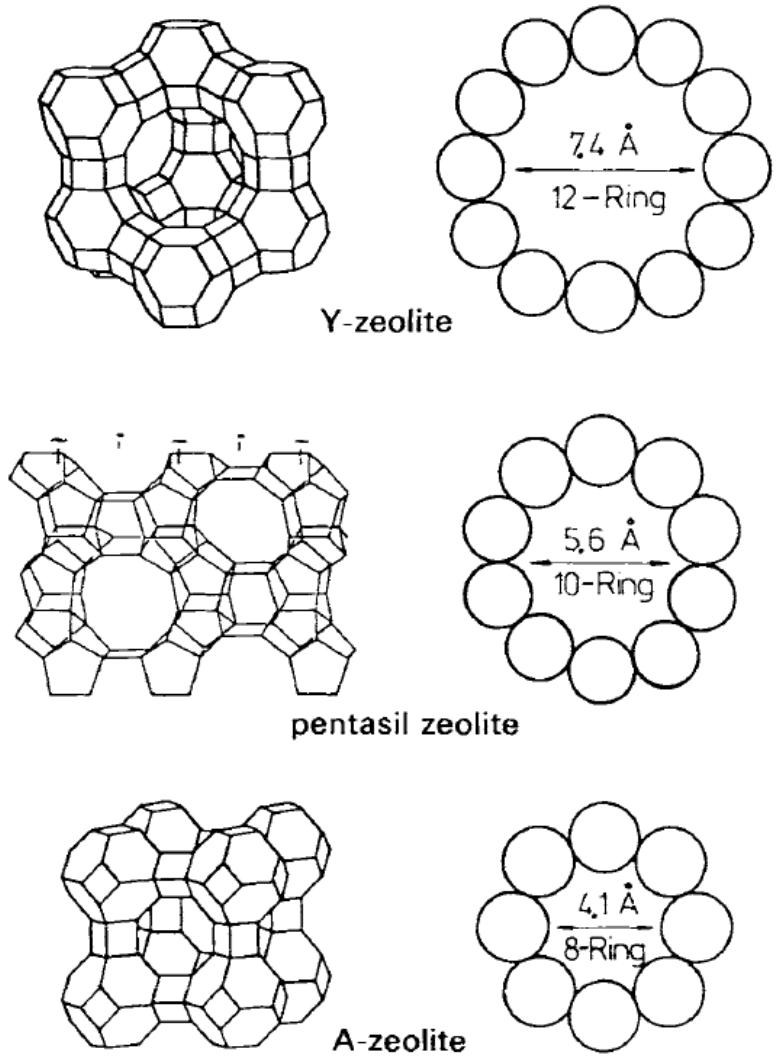

Figure I-2. Zeolite structures [4].

Table I-1. Classification of zeolites according to their pore size [4].

Small pore	Ref.	Medium pore	Ref.	Large pore	Ref.
A	[5–10]	ZSM-5	[11]	Faujasite	[5–10]
Erionite	[6–8]	ZSM-11	[6–8]	X/Y	[5–10]
Chabazite	[6–8]	ZSM-22	[12–15]	Mordenite	[6–8]
		NU-10	[12–15]	Offretite	[6–8]
		Theta 1	[12–15]	L	[6–8]
		ZSM-23	[16, 17]	Omega	[6–8]
		ZSM-48	[6–8]	ZSM-4	[5–10]
		TS-1	[18]	ZSM-12	[5–10]
		Silicalite	[19]	Z	[20]

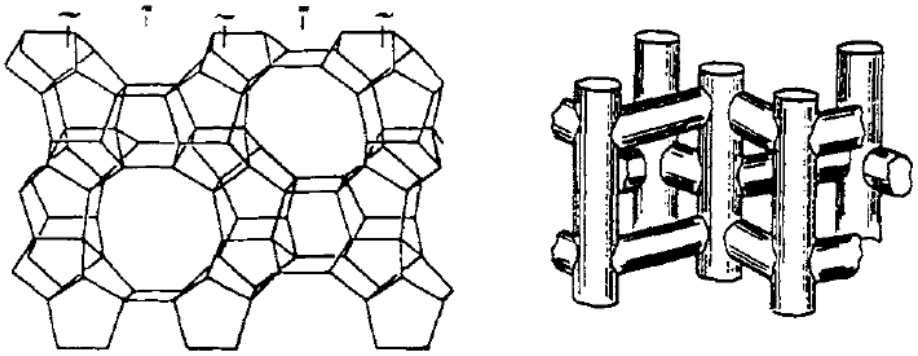

Figure I-3. Pentasil zeolites with emphasized channel system (right) [4].

I-1-2. Titanosilicates

Another class of microporous materials is those consisting of metal elements both in tetrahedral and octahedral coordination. During the last years more and more studies appeared on the synthesis of new microporous materials owing to the possibility of obtaining novel properties different from those of conventional zeolite materials. The first synthetic work of titanium-containing microporous materials was carried out by Young in 1967 [21]. Many researchers have studied titaium-containing microporous materials by incorporation of titanium into the zeoite structure [22–24].

Engelhard titanosilicate (ETS) represents a new class of microporous zeolite-type titanosilicate materials. Unlike zeolites, these new materials have frameworks that are composed of corner-sharing SiO_4 tetrahedra and TiO_6 octahedra, resulting in new structures that cannot be built by connecting only tetrahedral units, the only framework units of conventional zeolites. Because titanium is octahedrally coordinated in the framework, every titanium ion needs two counterbalancing cations to maintain electro-neutrality, while conventional zeolites require one extra framework cation to balance the single minus charge. Two important members of this family are ETS-10 [25, 26] and ETS-4 [27–30], Both of which contain $–O–Ti^{IV}–O–$ chains with Ti(IV) in octahedral coordination that exhibit quantum electron-hole confinement,

behaving as one-dimensional nanowires (Figure I-4) [31, 32]. ETS-10 has a three-dimensional 12-MRs pore system (pore size: ~8 Å) and ETS-4 has a small pore opening of ~4 Å (8-MRs). Due to the tunable pore characteristic and other distinct properties related to the framework structure, they are considered as possible new catalysts, molecular sieves, ion exchangers and other important applications.

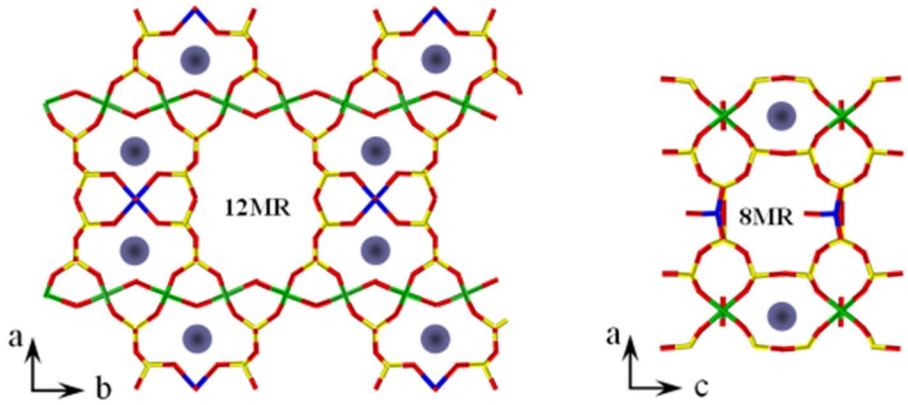

Figure I-4. ETS-4 framework [30]. Octahedrally coordinated titanium atoms that form –O–Ti–O– chains along the b direction are shown in green. The titania semioctahedra of the bridging units that are connected to four framework silicon atoms through oxygen bridges are shown in blue. Silicon and oxygen atoms are shown in yellow and red, respectively. The a-b slice (left) shows the 12-MR opening while the a-c slice (right) shows the 8-MR opening. Sodium cation sites in the 6-MR are shown.

I-2. Layered materials

Layered materials have frameworks with high aspect ratio and two-dimensionally confined nano-spaces in the interlayers and have been widely used in various fields, such as adsorbents, catalysts, ion exchangers, and fillers for polymers [33]. Many layered materials, which act as host materials, can accommodate various guest molecules in the interlayer spaces by using various interactions such as intercalation and pillaring. Surface properties (polarity and ionicity) of layered materials are important for the interactions. From the perspective of ionicity, layered materials can be classified into three types as follows: (i) cation-exchange layered materials, which have negative charge in the layers, such as layered clay minerals, metal oxides, metallosilicates, and silicates; (ii) anion-exchange layered materials, which have positive charge in the layers, such as layered double hydroxides (LDH); and (iii) neutral layered materials, such as graphite and layered chalcogenides. Conventional layered materials do not possess channel systems or open frameworks within layers, limiting their uses in conventional microporous materials applications like selective catalysis, adsorption, and separation.

I-2-1. Layered silicates

Layered silicates are built of interconnected SiO_4 tetrahedra within layers and these layers are held togeter by exchangeable cations that are often hydrated [34]. Although layered silicates are cation-exchangeable, layered silicates have some differences from layered clay minerals. Layered silicates have interlayer silanol groups and the origin of negatively charged sites are SiO^-. In the case of clay minerals, negatively charged sites arises from isomorphous substitution, such as substitution of trivalent elements with divalent elements, within the layers. The exact position of substitution sites in clay minerals is very difficult to define except for a few reports of anionic clay LDH. In contrast, the ordering of $SiOH/SiO^-$ groups of layered silicates can be defined specifically on the basis of their structures. The structure of layered silicates are usually composed of Q^3 ($(O^-/HO)Si(OSi)_3$) and/or Q^4 ($Si(OSi)_4$) units. There are many studies of natarual and synthetic layered silicates, such as magadiite, kenyaite, makatite, kanemite, and RUB-18 [35–38]. Figure I-5 shows examples of framework for various layered silicates.

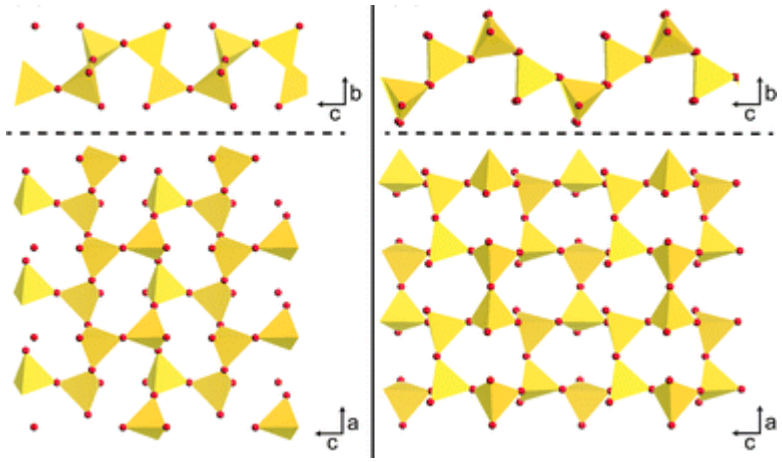

Figure I-5. Silicate frameworks of (a) kanemite and (b) makatite [33].

I-2-1-1. Non-covalent modification of layered silicates

Intercalation reactions of layered silicates are driven by hydrogen bonding, cation exchange, dipole–dipole interaction, van der Waals force, and acid–base reaction [34]. These intercalation reactions are termed as non-covalent modifications because covalent bonds are not formed by these reactions. Interlayer cations, such as alkaline metal cations, in layered silicates can be exchanged with various inorganic and organic cations. On the basis of this property, layered silicates were used as softner of water and selective adsorbent. Exchange reaction of interlayer cations with proton is important for the following intercalation processes because alkaline metal cations hinder other intercalation reactions owing to stronger interactions between the cations and SiO^- groups of interlayer surfaces. Protonated layered silicates can act as host materials. Thus, the properties of layered silicates can be changed depending on which guest molecules are intercalated. For example, by changing the size of guest molecules, one can manipulate the basal d-spacings between the layers, which often gives great controllability over size selectivity when it comes to the catalytic applications. However, it is very difficult to immobilize guest molecules with defined locations and to prevent the release of guest molecules.

I-2-1-2. Covalent modification of layered silicates

Layered silicates can be modified covalently, such as condensation, silylation, and esterification of SiOH/SiO^-groups [33]. These reactions are denoted as covalent modifications. The covalent modifications make it possible to design interlayer space, interlayer framework, and interalyer surface of layered silicates. Unlike non-covalent midifications, the density and distance of immobilized functional groups can be deliberately controlled at the angstrom level in two-dimensionally confined spaces by utilizing the structure of the host layered silicates. These covalent modifications of layered silicates make it possible to design for practical applications (Figure I-6).

I-2-2. Layered zeolitic materials

Although almost all zeolites contain three dimensional porous structures, some zeolites (or their precursors) have layered structures [39, 40]. They can be categorized as layered silicates because of their layer frameworks composed of SiO_4 tetrahedra and SiOH/SiO^-groups on the surfaces of layers. The early reports of layered zeolitic materials are EU-19, MCM-22, and precursor of FER-type zeolite (PREFER) [41–43]. There are various layered

zeolitic materials, such as ITQ-6, MCM-47, MCM-65, MCM-69, PLS-1, ERS-12, Nu-6(1), RUB-39, and UCB-1 [44–52].

A large number of active sites on the external surface of these layered materials show highly catalytic activity, high diffusion, and suppression of catalyst deactivation [53]. The presence of reactive SiOH groups on the interlayer surfaces should also widen the possibilities by incorporating various functional groups onto the interlayer surfaces. When metal species are incorporated into the layers, such as Al-ITQ-6 and Ti-ITQ-6 (layered metallosilicates), all active sites should be located on the accessible surfaces, that is advantageous for the catalytic activities [44].

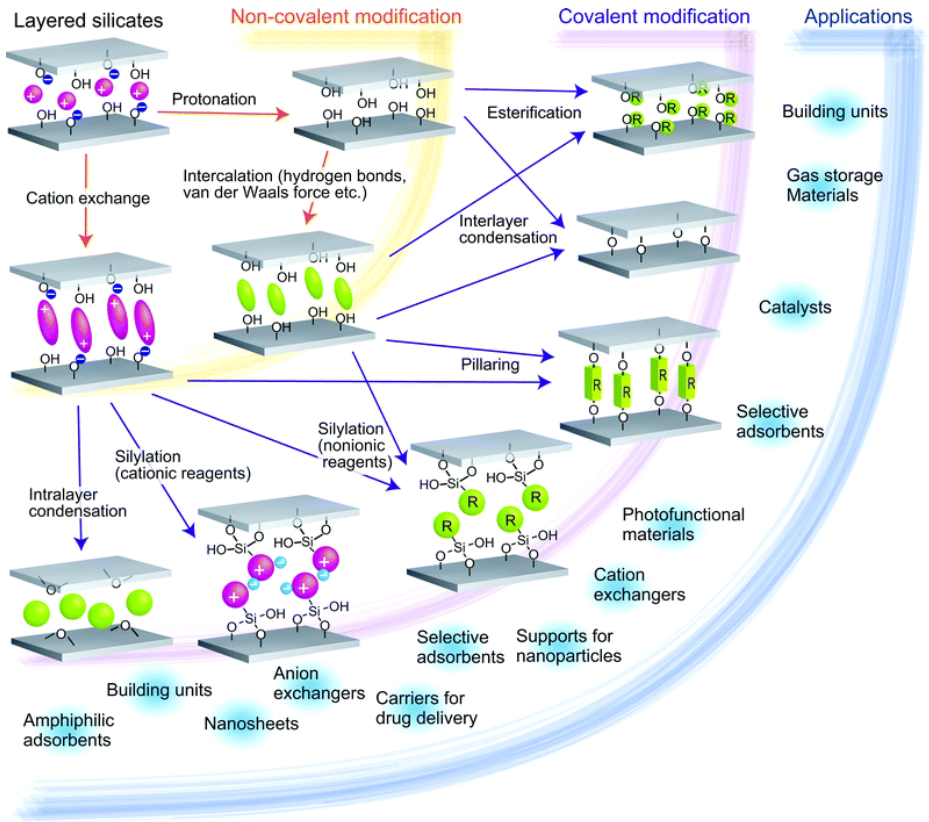

Figure I-6. Materials design of layered silicates with non-covalent and covalent modifications [33].

I-3. AMH-3

AMH-3, developed by H.-K. Jeong [54], is one of layered silicates and has characteristics of both layered silicate and zeolite in the previous sections owing to its unique framework. AMH-3 is composed of silicate layers containing 8-MRs in all three principal crystal directions. Strontium cations, sodium cations and water molecules were located in the intralayer and interlayer spaces of AMH-3. Jeong et. al reported the crystal structure illustrations of AMH-3 by using oak ridge thermal ellipsoid polt (ORTEP) program. Figure I-7. shows views of the of the crystal structure down the [010], [001], and [100] axes respectively. It can be seen that 8-MRs in all three directions are present. The layers are stacked along [100] axis, with charge-balancing cations and water molecules in the interlayer space. Figure I-7c shows that the asymmetric unit of the silicate layers is a 4-MRs containing the silicon atoms SI1, SI2, SI3 and SI4. It can be seen that the silicon atoms SI3 and SI4 are topologically identical and have the same coordination environment from the structure of the layer. These could possibly be related by a symmetry operation if AMH-3 had orthorhombic symmetry. However, the monoclinic angle deviates significantly from 90°, and the diffraction patterns could not be indexed adequately with an orthorhombic unit cell.

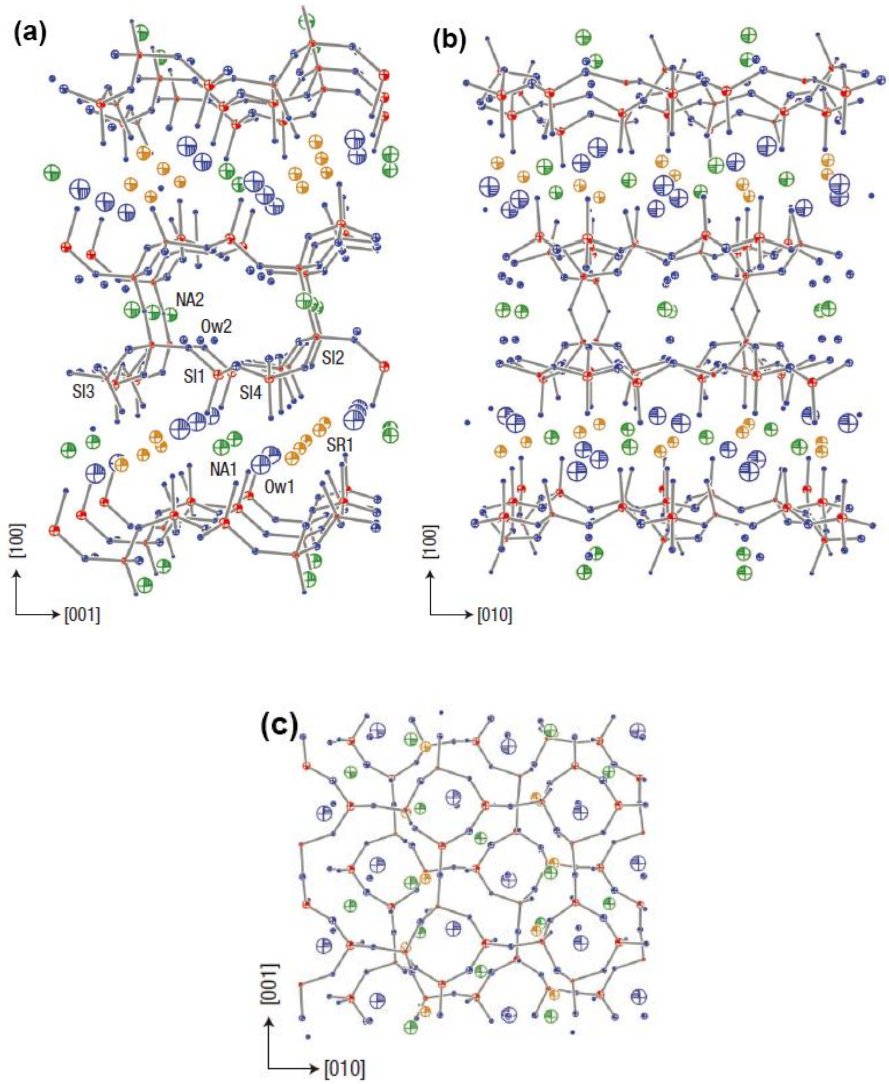

Figure I-7. Ortep views of the AMH-3 structure along three crystallographic directions [54]. Colour coding:red = Si,blue = O,green = Na, gold = Sr. The size of the spheroids is proportional to their isotropic Debye–Waller factors.AMH-3 consists of layers with 8-MRs in all three crystallographic directions,spaced by Sr cations,Na cations and water molecules.

Projections of the AMH-3 structure with the cations and water molecules removed for clarity are shown in Figure I-8. Each layer is formed by bonding together two silicate sheets containing 4-MRs and 8-MRs that provide a possible transport path from one layer to the next. Jeong et. al suggested the the close relationship of AMH-3 with two new zeolite topologies, resulting from translation or rotation of individual layers followed by bonding of the layers with each other as shown in Figure I-9. Figure I-9 leftside shows that translation of one layer approximately along [011] brings the $Si\text{-}O^-$ groups of adjacent layers into close proximity, allowing a possible interlayer condensation into a new 'small-pore' zeolite type, containing 8-MRs. Translation of the layer along [011] followed by a 180° rotation about the [100] axis (Figure I-9, rightside) leads to a second small-pore zeolite type. Because these two framework types are formed by bonding of individual layers, a number of disordered intergrowths between these two hypothetical materials are also possible. No additional silicate species need be added to perform these conversions. From these schematic of AMH-3 framework, it is comfirmed that AMH-3 has three dimensional microporosity like zeolites. Owing to its unique internal microporosity within the layers, AMH-3 can be used as a selectivity-enhancing filler in polymers.

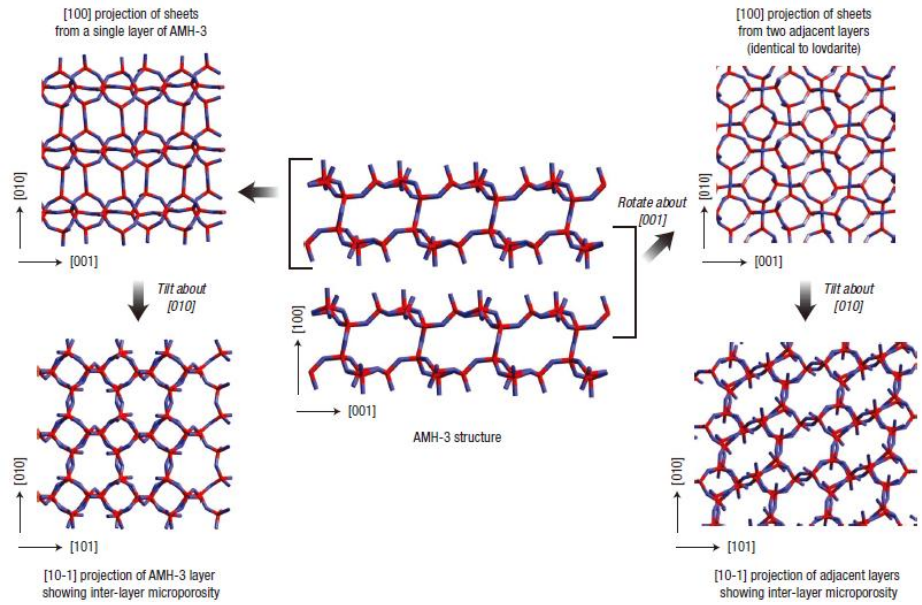

Figure I-8. Projections of the AMH-3 structure omitting cations and water molecules [54]. Top left:Projection of a single AMH-3 layer down [100]. Bottom left: Projection of the same layer along [10-1] showing 8-MRs in the layer. Top right: Projection down [100] of two sheets from adjacent layers. Bottom right: Projection of the same down [10-1] showing an interlayer transport path through 8-MRs. Red = Si, blue = O.

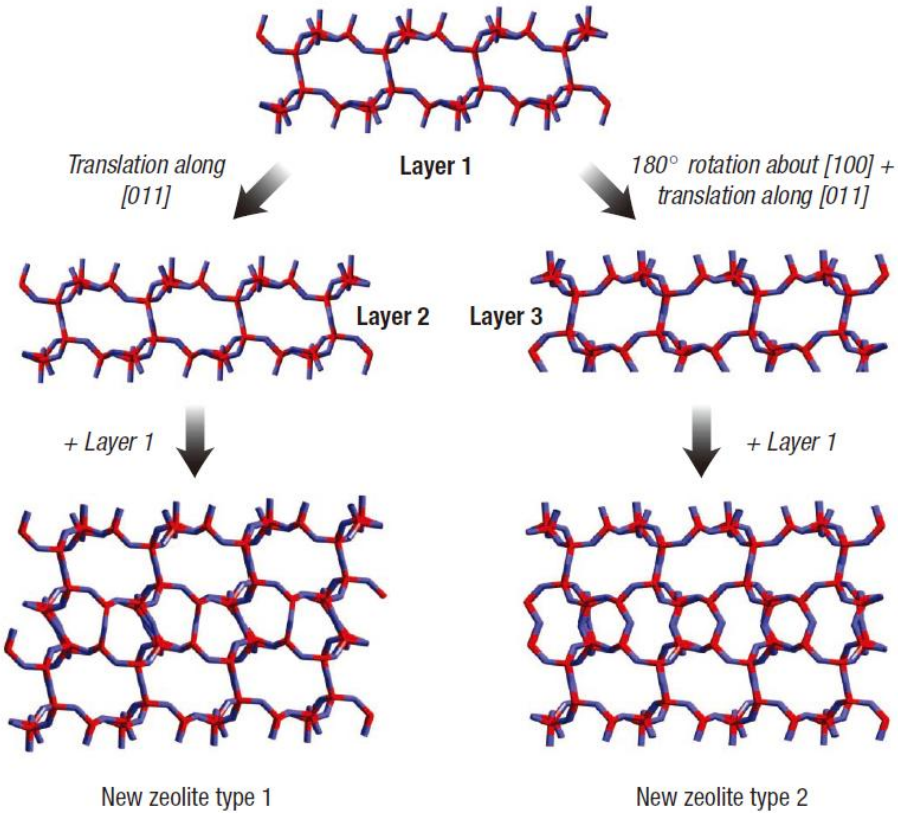

Figure I-9. Construction of two new zeolite frameworks from AMH-3 layers [54]. Left: Translation of Layer 1 along [011] leads to Layer 2. Bonding of layers 1 and 2 leads to a new zeolite (Type 1). Right: Translation and rotation of Layer 1 leads to Layer 3.Bonding of layers 1 and 3 leads to another framework (Type 2). Red = Si, blue = O.

Like other layered materials, interlayer cations (Sr^{2+} and Na^{+}) within AMH-3 can be exchanged with various inorganic and organic cations. Many researchers reported that AMH-3 was swollen by the intercalation of organic surfactants, such as quaternary alkyl ammonium ions or amine molecules [55–57]. Figure I-10 shows the SEM and TEM images of proton-exchanged AMH-3 and swollen AMH-3. It can be seen that considerable changes in the silicate structure took place by the intercalation reaction. Instead of a flat surface, the swollen AMH-3 reveals serrated edges which look like a stack of thin plates (Figure I-10c and d). Considering the unit cell dimension of AMH-3, it seems that the thickness of a single planar substructure is comparable to that of a few silicate layers [56]. These images illustrated that each of the nanoscopic substructures shown in SEM images consist of few silicate layers spaced by surfactant molecules. These studies confirmed that AMH-3 has the ability for intercalation, pillaring, and exfoliation like layered materials. By changing the intercalating materials, the basal d-spacings between the layers can be manipulated, which often gives great controllability over size selectivity when it comes to the catalytic applications.

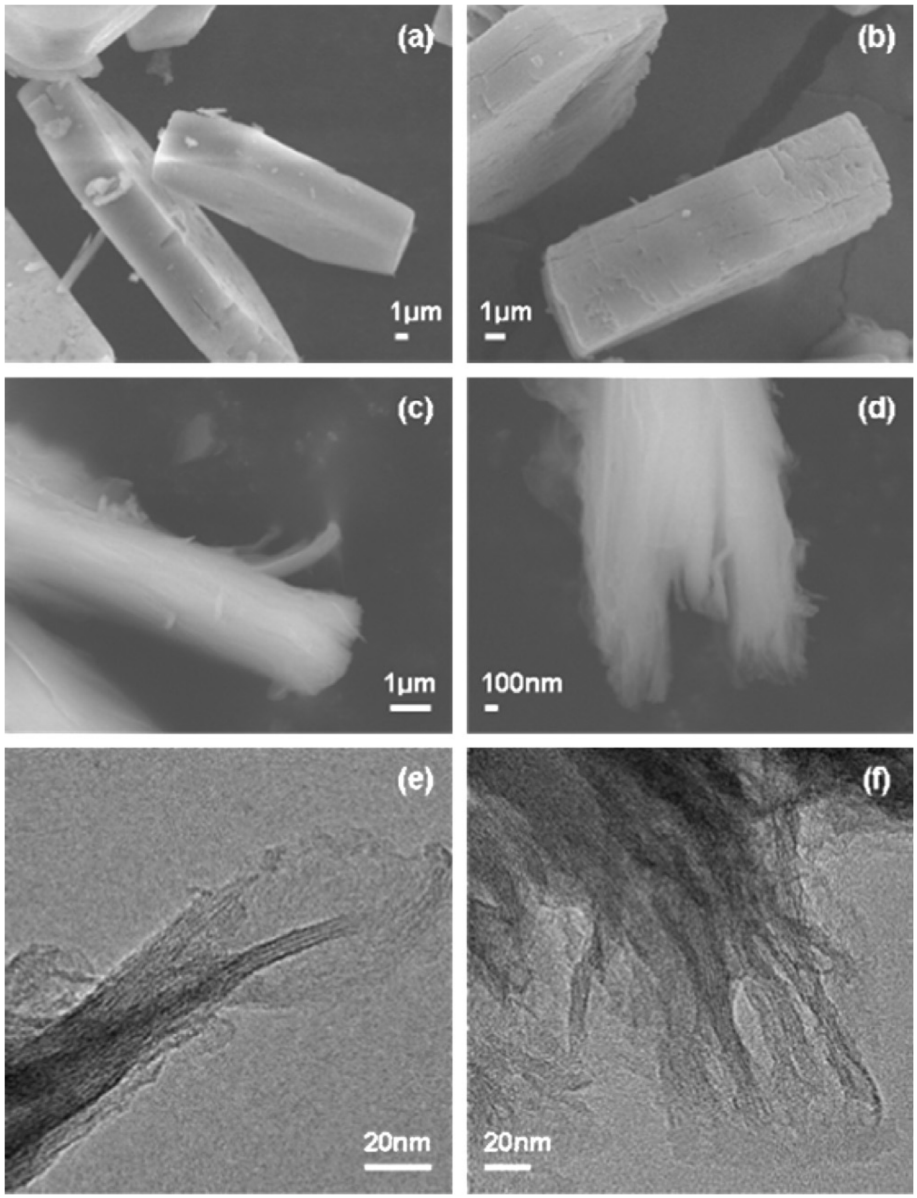

Figure I-10. SEM images of (a) original AMH-3, (b) proton-exchanged AMH-3, (c) and (d) swollen AMH-3. TEM images of swollen AMH-3 are given in (e) and (f) [56].

I-4. Research Objectives

The main objective of this study was to investigate micoroporus layered silicate AMH-3 in terms of synthesis mechanism, structural properties, and applications. Besides well-known three dimensional microporosity of AMH-3, in particular, we focused on the ion exchange capacity due to cations within AMH-3, which no one noticed. Owing to these structural properties, AMH-3 could perform effectively in sorption and molecular sieve. In this study, the synthesis mechanism and ion exchange behavior of AMH-3 were investigated, which have not been studied so far. On the basis of the ion exchange properties of AMH-3, we attempt studies of AMH-3 as sorbent for efficient and selective removal of heavy metal ions. Based on the ion exchange behavior, AMH-3 was acid-hydrothermally treated in order to activate the micropores that were occluded by cations. The acid-hydrothermal treated AMH-3 with activated micropores was incorporated to reduce the vanadium ion transport through the ion exchange membranes in vanadium redox flow batteries by selective ion transport property of AMH-3.

Chapter II: We suggested the synthesis mechanism of AMH-3 based on the synthesis mechanism of zeolites. The synthesis conditions for AMH-3 synthesis such as the molar composition of the reaction mixture and

hydrothermal time was changed. The resulting materials were characterized by X-ray diffraction (XRD), field-emission scanning electron microscopy (FE-SEM), ^{29}Si magic angle spinning nuclear magnetic resonance (MAS NMR), fourier transform infrared (FT-IR), and Raman spectroscopy. A reasonable model for the synthesis mechanism of AMH-3 is proposed and discussed in more detail on the basis of experiments.

Chapter III: The ion exchange behavior of AMH-3 was investigated by the sorption of cations onto AMH-3 under various batch conditions. The structural changes during the ion exchange were characterized by XRD and ^{29}Si MAS NMR. Since AMH-3 has high theoretical ion exchange capacity, it is expected that AMH-3 will not only efficiently remove heavy metals via ion exchange with its abundant cations, but that it also has potential for the selective removal of heavy metals owing to its uniform micropore and layered structure. The removal of various heavy metals by AMH-3 from aqueous solutions was carried out under various experimental conditions and examined the kinetics of sorption and other parameters involved.

Chapter IV: We describe a simple method to remove cations within AMH-3 for activation of micropores and delaminate the AMH-3 layer with acid-hydrothermal treatment (1 M HCl), without the use of a swelling agent. To investigate the effect of the hydrothermal treatment, AMH-3 was immersed in 1 M HCl aqueous solution at room temperature (25 ± 2 °C). The morphology

of acid-hydrothermal treated AMH-3 (D-AMH-3) and acid treated AMH-3 was characterized by FE-SEM. ^{29}Si MAS NMR, FT-IR, Raman were used to characterize the structural changes occurring during the cation removal process. For quantitative analysis of the effects of post-treatment, the variations of the cations contents were determined with ICP-AES and the specific surface area was estimated with the Brunauer-Emmett-Teller (BET) method using the nitrogen adsorption–desorption isotherm technique.

Chapter V: We developed the ion exchange membranes for use in vanadium redox flow batteries, which have the requirements of high proton conductivity and low vanadium permeability. A Nafion-based composite membrane having a D-AMH-3 layer was prepared by solution casting and hot pressing. In order to examine the effect of D-AMH-3 layer, we controlled the thickness of the Nafion/D-AMH-3 membrane, which is similar to the thickness of a neat Nafion. FE-SEM with EDX detection was used to determine the morphology of the composite membranes. Gravimetric analysis was performed to investigate the swelling behavior. The ion exchange capacity (IEC) of each composite membrane was measured with the acid-base titration method. Vanadium permeability was analyzed by inductively coupled plasma atomic emission spectrometry. The performance of each single cell was evaluated by charge–discharge test at various current densities.

Chapter VI: As in the chapter V, we prepared SPEEK-based composite membranes containing ultrasonicated D-AMH-3 (U-AMH-3) to improve the membrane properties (vanadium permeability, mechanical strength, and etc.) and VRB single-cell performance. The composite membranes were prepared using a solution casting method with various U-AMH-3 contents. FE-SEM with EDX detection was used to determine the morphology of the composite membranes and U-AMH-3 dispersion. Gravimetric analysis was performed to investigate the swelling behavior. The IEC of each composite membrane was measured with the acid-base titration method. Tensile measurements on the composite membranes were carried out using a universal test machine. Vanadium permeability was analyzed by inductively coupled plasma atomic emission spectrometry. The impedance characteristics of the composite membranes were determined by using a Solartron electrochemical impedance analyzer with ZPLOT software. The performance of each single cell was evaluated by charge–discharge test at various current densities.

CHAPTER II

SYNTHESIS OF LAYERED SILICATE AMH-3 AND ITS SYNTHESIS MECHANISM STUDY

II-1. Introduction

Layered silicates are known as high silica alkali silicates, whose frameworks are composed of only SiO_4 tetrahedra [33, 34]. Layered silicates have exchangeable ions within the interlayers. Based on these structrual properties, layerd silicates are widely used in various fields such as ion exchange, adsorption, catalysis and fabrication of nanocomposites [58–65]. Several layered silicates posess channel systems or open frameworks within the layers like zeolites [39, 40, 44–52]. AMH-3, developed by H.-K. Jeong, is the first layered silicate with micoroporosity through eight-membered ring (8-MR) apertures along the thickness of the silicate layer as well as in the plane of the layers [54]. Because of this unique structure, AMH-3 has three-dimensional ordered microporosity and good acid, chemical and thermal stability like zeolite and provides the ability for intercalation, pillaring, and exfoliation like layered silicate [55–57, 66].

AMH-3 is synthesized hydrothermally from an aqueous reaction mixture

with following molar composition: 1 TiO_2: 10 SiO_2: 14 NaOH: 2 $SrCl_2$: 675 H_2O. Although there are no titanium species within AMH-3 frameworks that are composed of only SiO_4, titanium species are necessary to synthesis of AMH-3. To elucidate this, the syntheis mechanism of AMH-3 should be investgated. Since AMH-3 has a new structure that is different from the conventional layered silicate, there is little known about how the AMH-3 forms. Similar to zeolites, AMH-3 is built of interconnected SiO_4 tetrahedra within layers. Therefore, the investigation of the synthesis mechanism of AMH-3 can refer to the synthesis mechanism of zeolites.

A typical hydrothermal synthesis of zeolite can be described in briefest terms as follows [67]:

1. Amorphous reactants containing silica and alumina species are mixed together with cation sources, usually in a basic aqueous solution (high pH).

2. The aqueous reaction mixture is heated in a sealed autoclave.

3. For some time after raising to synthesis temperature, the reactants remain amorphous.

4. Crystalline zeolite can be produced after induction period.

5. Gradually, essentially all amorphous material is replaced by an approximately equal mass of zeolite crystals.

The silica and alumina species which will make up the microporous framework are imported in an oxide form, containing Si–O and Al–O bonds. The crystalline zeolite containing Si–O–Al linkages is created during the hydrothermal reaction in the presence of a mineralizing agent. Figure II-1 shows a generalised mechanism for zeolite synthesis. A summary of principal proposals for zeolite synthesis mechanism is given in Table II-1. The synthesis mechanismm of zeolite can be most adequately explained by a mechanism based upon the solution–mediation model.

The objective of this chapter is to study the synthesis mechanism of AMH-3 based on the synthesis mechanism of zeolite. To achieve this, the synthesis conditions for AMH-3 synthesis such as the molar composition of the reaction mixture and hydrothermal time was changed. The resulting materials were characterized by X-ray diffraction (XRD), field-emission scanning electron microscopy (FE-SEM), ^{29}Si magic angle spinning nuclear magnetic resonance (MAS NMR), fourier transform infrared (FT-IR), and Raman spectroscopy. A model for the formation of AMH-3 was proposed and discussed in detail on the basis of experiments.

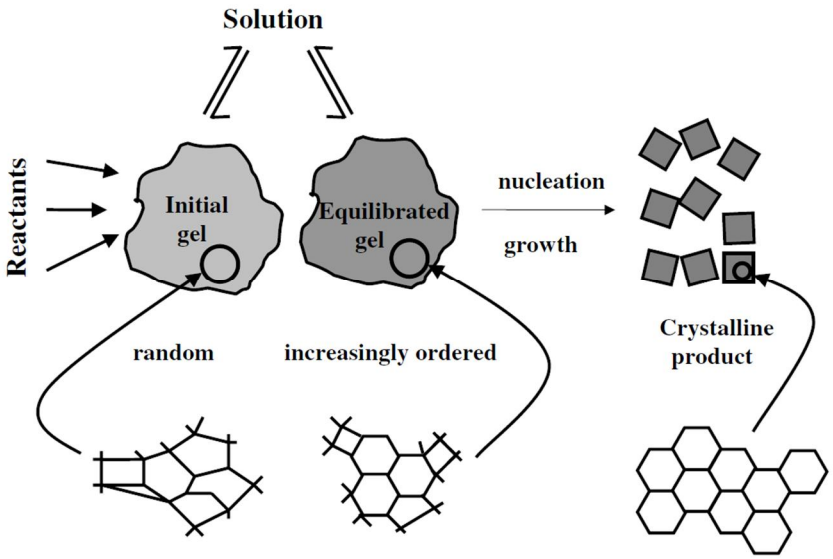

Figure II-1. A generalised mechanism for zeolite synthesis [67].

Table II-1. Summary of principal proposals for zeolite synthesis mechanism [67].

Principal system	Main features of mechanism	Schematic summary
Various low-silica phases	Condensation polymerisation of polygonal and polyhedral anions	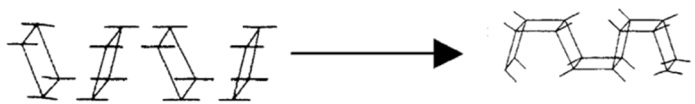
Na-X	Linkage of polyhedra (formed by M^+-assisted arrangement of anions): crystal growth mainly in the solid phase	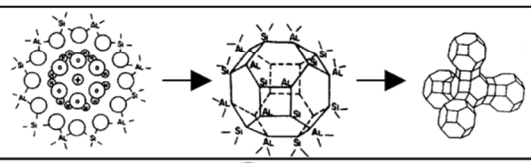
Na-A	Crystal growth from solution species	
TPA-Si-ZSM-5	Pre-organised composites, nucleation through aggregation, crystal growth layer-by-layer	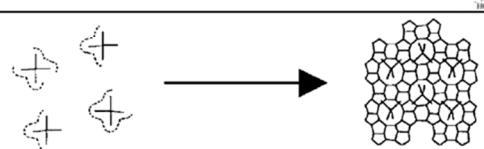
TPA-ZSM-5	Solid hydrogel phase transformation	 Silica-alumina gel

II-2. Experimental Section

II-2-1. Materials

Strontium chloride hexahydrate ($SrCl_2 \cdot 6H_2O$, 99%, Junsei), titanium trichloride ($TiCl_3$, 20%, Kanto), sodium silicate solution (26.5% SiO_2, Sigma-Aldrich), sodium hydroxide (NaOH, 98%, Sigma-Aldrich) were used as received, without further purification. Highly deionized water (18 MΩ cm^{-1}) was used in all experiments.

II-2-2. Synthesis of AMH-3

AMH-3 was synthesized by using the hydrothermal reaction of a mixture with following molar composition: 1 TiO_2: 10 SiO_2: 14 NaOH: 2 $SrCl_2$: 675 H_2O [54]. In a typical synthesis, NaOH was dissolved in deionized water. This solution was heated at 80 °C, then $SrCl_2 \cdot 6H_2O$ was added. The solution was stirred for 30 min. After 30 min of stirring, sodium silicate solution was added dropwise and stirred for 30 min. Finally, $TiCl_3$ solution was added dropwise and stirred for another 1 h. The resulting mixture was poured into a Teflon-lined stainless steel autoclave and crystallized at 200 °C for 1 day. The product contains amorphous material that was removed to yield pure AMH-3 as follows. The product was diluted with deionized water and kept for 1 h in

an ultrasonic bath, and then the suspension was decanted from the AMH-3 sediment. The AMH-3 sediment was washed with deionized water and kept for 1 h in an ultrasonic bath. This purifying procedure was repeated five times. After purifying, the AMH-3 sediment was dried overnight at 80 °C.

II-2-3. Characterization

All characterization was conducted at 25 ± 2 °C. The morphology of the materials was examined with a field emission scanning electron microscope (JEOL, JSM-6700F) equipped with an energy-dispersive spectroscope working at 6 kV. X-ray diffraction (WXRD) patterns of the materials were collected with a MAC/Sci. MXP 18XHF–22SRA diffractometer equipped with graphite monochromatized Cu-Ka radiation (k = 1.541 Å, 50 kV, 100 mA) was used as the X-ray source. ^{29}Si magic angle spinning nuclear magnetic resonance (MAS NMR) measurements were performed on a Bruker Avance II spectrometer. The recycle delay was 15 s, with approximately 500 scans required for a full 7 mm rotor spinning at 7 kHz. Fourier Transform Infrared Spectroscopy (FT-IR) spectra analyses were performed on samples pelletized with KBr powder by using a Thermo Scientific Nicolet 6700 IR spectrophotometer with a resolution of 4 cm^{-1}. Raman spectra were obtained using a DXR2xi equipped with a diode laser at 532 nm.

II-3. Results and Discussion

II-3-1. Characterization of AMH-3

Figure II-2a shows the FE-SEM image of AMH-3. It was confirmed that AMH-3 had plate-like shape and the size of AMH-3 was about 20 μm. Study on the structure of AMH-3 was characterized by XRD. A summary of the crystalline properties of AMH-3 given in Table II-2. On the basis of XRD results as shown in Figure II-2b, d-spacing values of AMH-3 were calculated using Bragg's law ($\lambda = 2d\sin\theta$). The miller indices of AMH-3 can be obtained using the following equation:

$$\frac{1}{d^2} = \frac{1}{\sin^2\beta}\left(\frac{h^2}{a^2} + \frac{k^2\sin^2\beta}{b^2} + \frac{l^2}{c^2} - \frac{2hl\cos\beta}{ac}\right)$$

These results were summarized in Table II-3. The first XRD peak at 2θ=7.79° is the (200) reflection of AMH-3 structure. The unit cell of AMH-3 includes two silicate layers and two interlayer spaces, which are aligned perpendicular to the [100] crystallographic direction [54]. The corresponding d-spacing value of 11.35 Å is the sum of a individual layer thickness and a interlayer space.

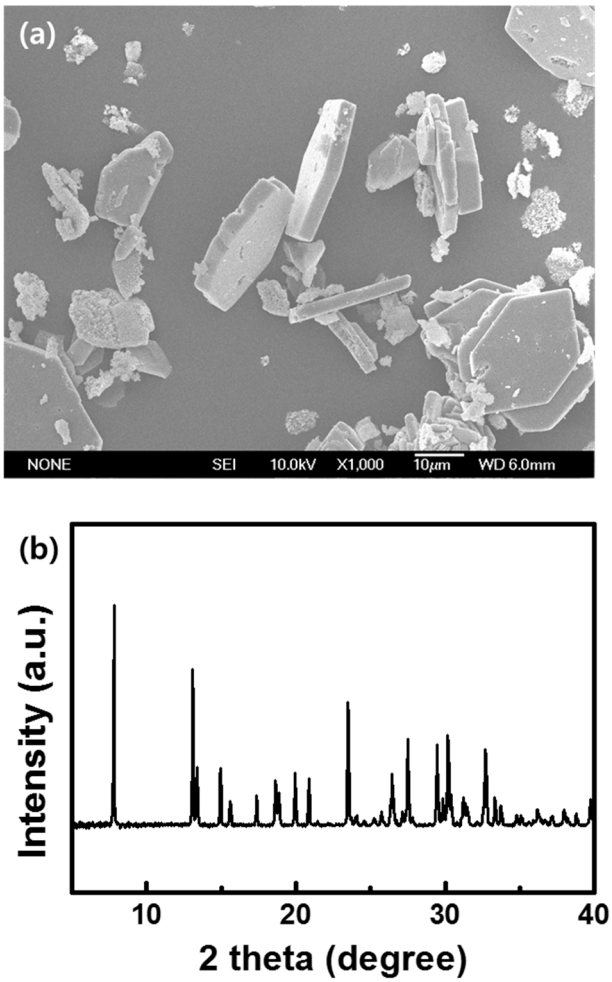

Figure II-2. (a) FE-SEM image and (b) XRD pattern of AMH-3.

Table II-2. Crystalline properties of AMH-3.

Crystalline parameters	
Cell length (Å)	a: 22.783, b: 6.9395, c: 13.581
Cell angle (θ)	α: 90, β: 92.5935, γ: 90
Symmetry	Monoclinic
Space group	C 2/c

Table II-3. Characteristic d-spacing, 2θ, and miller indices of AMH-3.

2θ (°) / d-spacing (Å) / miller indices (hkl) of AMH-3		
11.35 / 7.79 / 200	6.76 / 13.09 / 002	6.62 / 13.37 / 110
5.93 / 14.94 / 210	5.68 / 15.59 / 400	5.10 / 17.36 / 310
4.75 / 18.65 / 311	4.71 / 18.82 / 112	4.45 / 19.95 / 212
4.25 / 20.87 / 501	3.78 / 23.51 / 013	3.37 / 26.44 / 021
3.24 / 27.50 / 602	3.03 / 29.46 / 114	2.99 / 29.87 / 222
2.96 / 30.19 / 420	2.94 / 30.37 / 612	2.86 / 31.26 / 513
2.74 / 32.71 / 123	2.69 / 33.34 / 521	2.65 / 33.74 / 223
2.37 / 37.98 / 315	2.27 / 39.75 / 230	

Valuable structural information about local structure can be obtained by solid state MAS NMR spectroscopy. ^{29}Si MAS NMR spectroscopy has been known to provide the structural information on the frameworks of zeolites in terms of the connectivity of SiO_4 tetrahedra as well as the Si–O–Si bond angles [57, 67]. An analysis of the ^{29}Si MAS NMR spectrum of AMH-3 was carried out in previous studies [54, 56, 57]. As can be seen in Figure II-3a, the NMR spectrum of AMH-3 contains three peaks located at –93, –90, and –89 ppm. The crystallographic structure (Figure II-3b) reveals that Si2 is connected to four silicon atoms (Q^4 silicon atom), whereas Si1, Si3 and Si4 are connected to three silicon atoms with the fourth Si-O bond directed into the interlayer space (Q^3 silicon atoms) (Q^n represents $Si(OSi)_n(OH)_{4-n}$). Jeong et al. associate the highest chemical shift (at –93 ppm) with the Si2 Q^4 species, the next highest (at –90 ppm) with the Si1 Q^3 species, and the intense resonance at –89 ppm with the Si3 and Si4 Q^3 species, both of which have a similar coordination environment [54]. The assigned chemical shifts are several ppm lower than those of typical zeolites, consistent with the smaller Si–O–Si angles in the AMH-3 structure. Choi et al. suggested that the presence of cations imposes structural restraints, resulting in unusual bond angles [57].

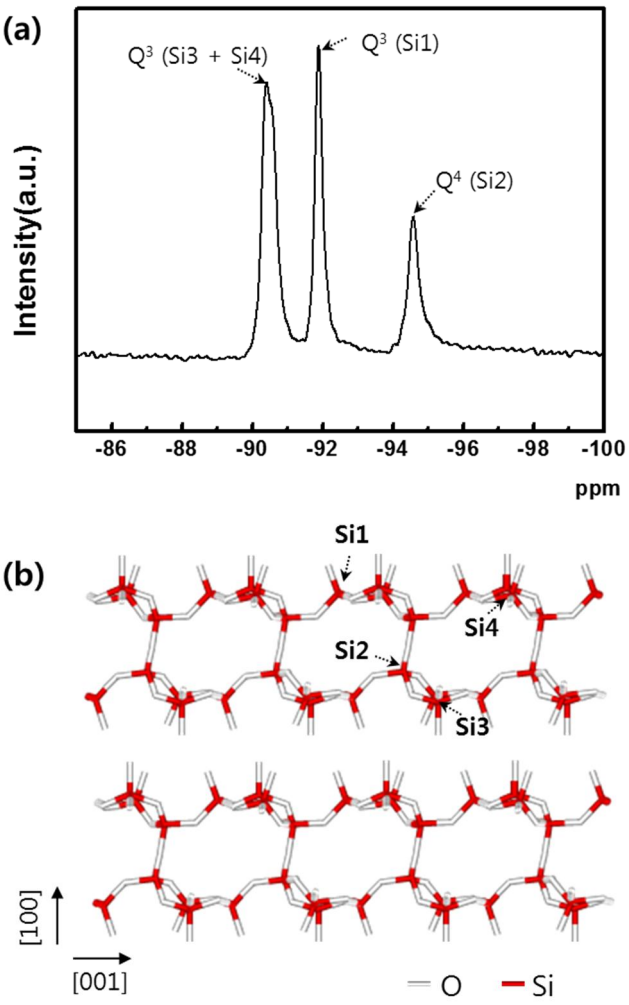

Figure II-3. (a) ^{29}Si MAS NMR spectrum of AMH-3 and (b) AMH-3 framework.

FT-IR and Raman spectroscopy were also used to characterize the structrue of AMH-3. Vibrations of the frameworks of nanoporous materials like zeolites give rise to the bands below 1300 cm^{-1} region [68]. Similar to zeolites, since AMH-3 is built of interconnected SiO_4 tetrahedra within layers, it is expected that similar assignments of vibrational bands can be possible. Figure II-4 shows the FT-IR spectrum of AMH-3. In the region between 650 and 400 cm^{-1}, the adsorption bands can be seen, which correspond to double rings in case of zeolites. Unlike zeolites, AMH-3 does not have double rings. Despite the absence of double rings in the AMH-3 framework, the bands between 650 and 400 cm^{-1} exists. These bands can be assigned to the single four-membered rings (S4R) because AMH-3 has a layer framework built of S4Rs including four silicon atoms (Si1, Si2, Si3, and Si4) [56]. The Si2 in adjacent sublayers is interconnected into Q^4 species, while the remaining three silicons (Si1, Si3, and Si4) lead to the Q^3 species being chargebalanced with Sr and Na cations. The bands between 1150 and 1050 cm^{-1} were assigned to the Q^3 external linkages. Figure II-4b shows the Raman spectrum of AMH-3. The bands below 300 cm^{-1} were assigned to Na–O stretching modes and Si–O–Si bending mode. The bands between 400 and 300 cm^{-1} were assigned to Sr–O stretching modes and pore opening modes of the 8-MRs [56]. The bands below 400 cm^{-1} mean that Na and Sr cations are strongly bound the layer, which is consistent with the ^{29}Si MAS NMR results.

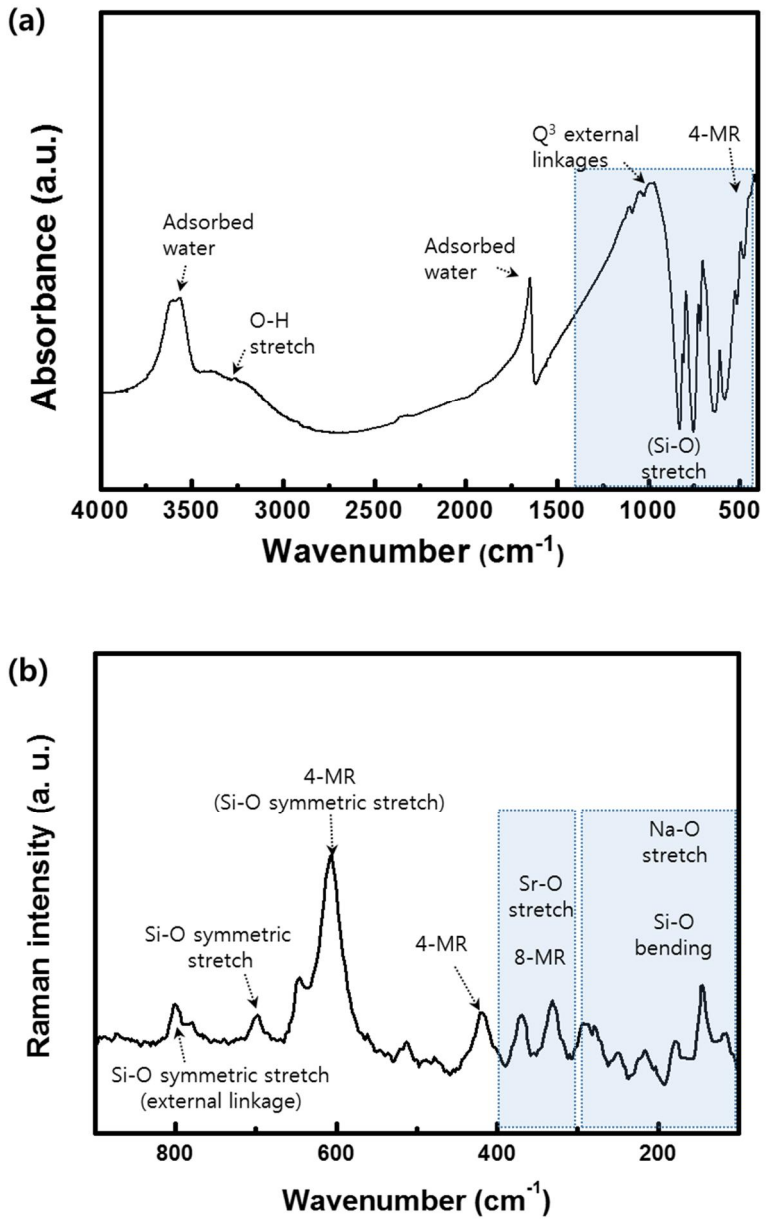

Figure II-4. (a) FT-IR spectrum and (b) Raman spectrum of AMH-3.

II-3-2. Synthesis mechanism study

The synthesis of zeolite and zeotype depend on the crystallization conditions and composition-dependent parameters. The synthesis mechanism of AMH-3 was investigated by studying the effects of titanium, strontium, and reaction time on AMH-3 synthesis. To achieve this, AMH-3 was synthesized by varing the mixture component. When the synthesis was attempted without both titanium and strontium, there was no solid particles formed, which means that the presence of titanium and strontium has a significant influence on the formation of particles. First, the variation of relative amount of titanium in the synthesis mixture was carried out. The molar composition of the mixture was x TiO_2: 10 SiO_2: 14 NaOH: 2 $SrCl_2$: 675 H_2O, where x was varied from 0 to 1. The XRD patterns of the samples prepared with various amount of titanium are shown in Figure II-5. It can be seen that the presence of titanium is essential for synthesis of AMH-3. In the absence of titanium, an unknown crystalline material was synthesized instead of AMH-3. This material could not be identified by the ICDD (International Center of Diffraction Data). From this result, it can be suggested that strontium plays a structuring role in the synthesis of crystalline material. It seems that the assembly of Si–O–Si bonds is mediated by strontium. During this cation-mediated assembly process, the initial gel for basic structural organisation may be formed. When x = 0.5, AMH-3 and the unknown crystalline material were formed.

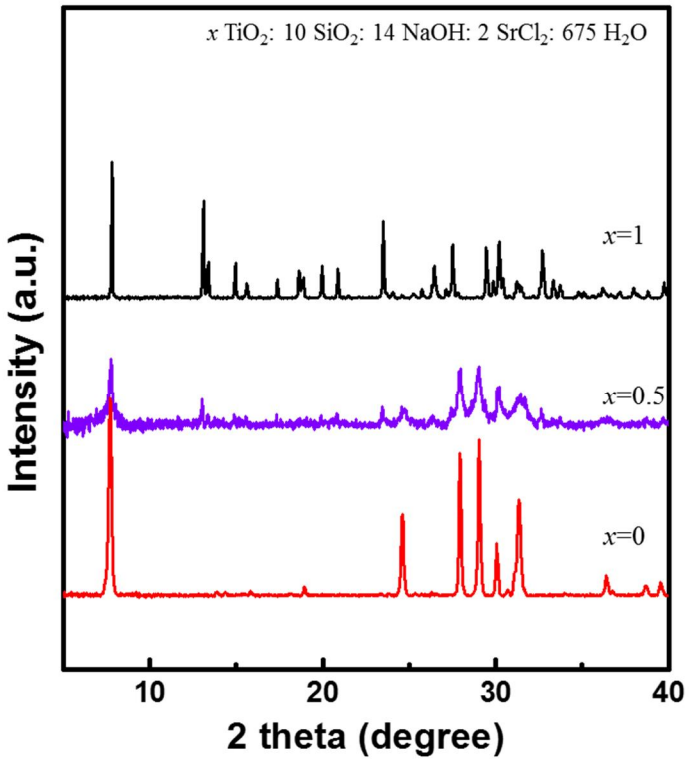

Figure II-5. XRD patterns of samples prepared with different amount of titanium.

In the FE-SEM image of the unknown crystalline material (Figure II-6b), it was confirmed that unknown crystalline material has plate-like morphology and its size is about tens to hundreds of nanometers, which is much smaller than AMH-3. It seems that titanium plays role in assembly and reordering of the initial gel formed by strontium-mediated assembly, resulting in secondary gel (semi-ordered).

Next, the variation of relative amount of strontium in the synthesis mixture was carried out. The molar composition of the mixture was 1 TiO_2: 10 SiO_2: 14 NaOH: x $SrCl_2$: 675 H_2O, where x was varied from 0 to 2. Figure II-7 shows the XRD patterns of the samples prepared with various amount of strontium. The XRD pattern of the resulting material synthesized without strontium was assigned to titanosilicate (ETS-4) that contains Ti–O bonds within framework. Unlike strontium, titanium does not act as coordination center for the assembly of Si–O bonds that form the framework composed of Si and O. When x = 1, amorphous phase was formed. At low amount of strontium, it was presumed that because all Si species do not form the initial gel (formed by strontium-mediated assembly), some Si species form another initial gel with titanium. Since both gels are mixed and affect each other, it was considered that amorphous phase was formed without growing into one crystal phase.

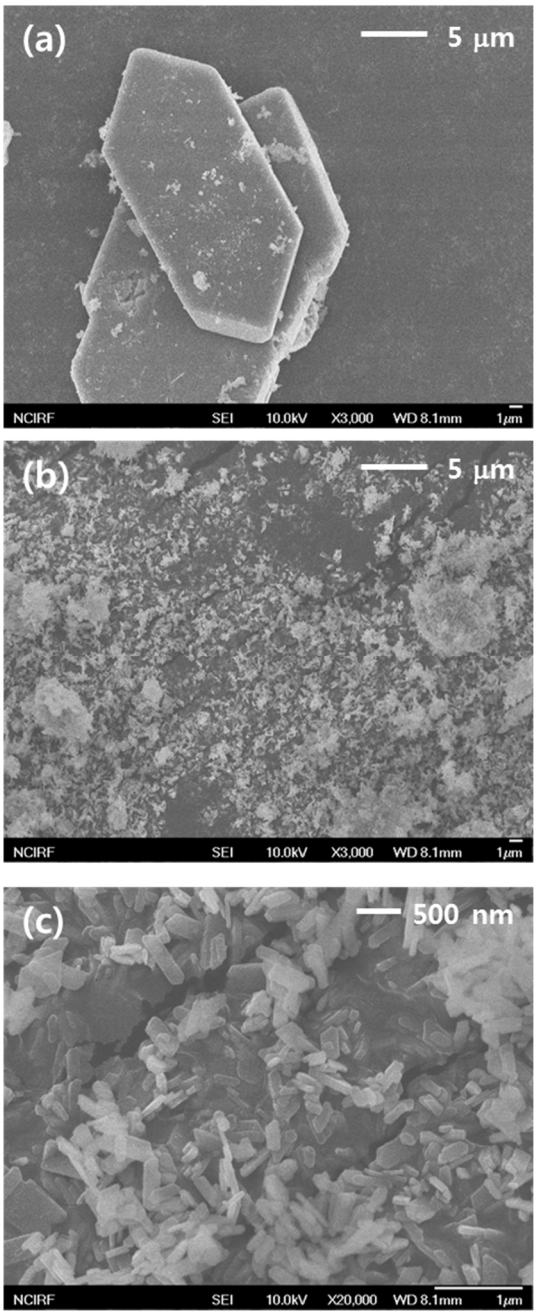

Figure II-6. FE-SEM images of (a) AMH-3, (b) unknown crystalline material (Ti=0), and (c) higher magnification image of (b).

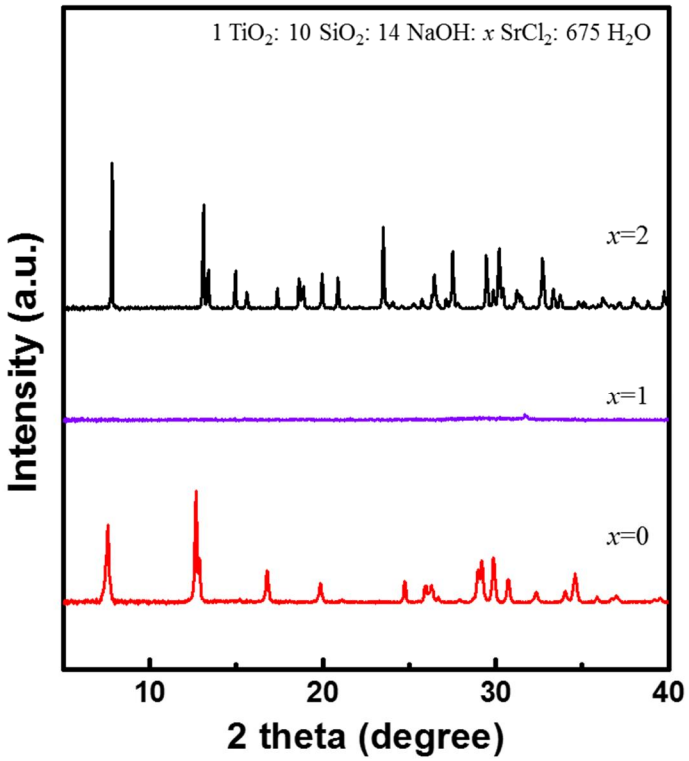

Figure II-7. XRD patterns of samples prepared with different amount of strontium.

In order to study the effect of reaction time on the formation of AMH-3, the experiments were conducted at 200 °C for various reaction time using the mixture of 1 TiO_2: 10 SiO_2: 14 NaOH: 2 $SrCl_2$: 675 H_2O. Figure II-8 shows FE-SEM images of the resulting materials with various reaction time. it was confirmed that AMH-3 was not formed within 4 h of reaction time, but formed after 6 h and the amount of AMH-3 increased as reaction time increases. Comparing Figure II-8g with Figure II-8f, the thickness and size of AMH-3 with 24 h reaction time was thicker and larger than that of AMH-3 with 6 h reaction time, which suggests that crystal growth occurred with reaction time. As shown in Figure II-9, the XRD patterns after crystallization for 2 and 4 h show only the peaks of the amorphous solid. The XRD peaks of AMH-3 increased with increasing reaction time, in agreement with the FE-SEM observation. This result indicates that there is no intermediate crystalline phase observed in the procedure of AMH-3 synthesis.

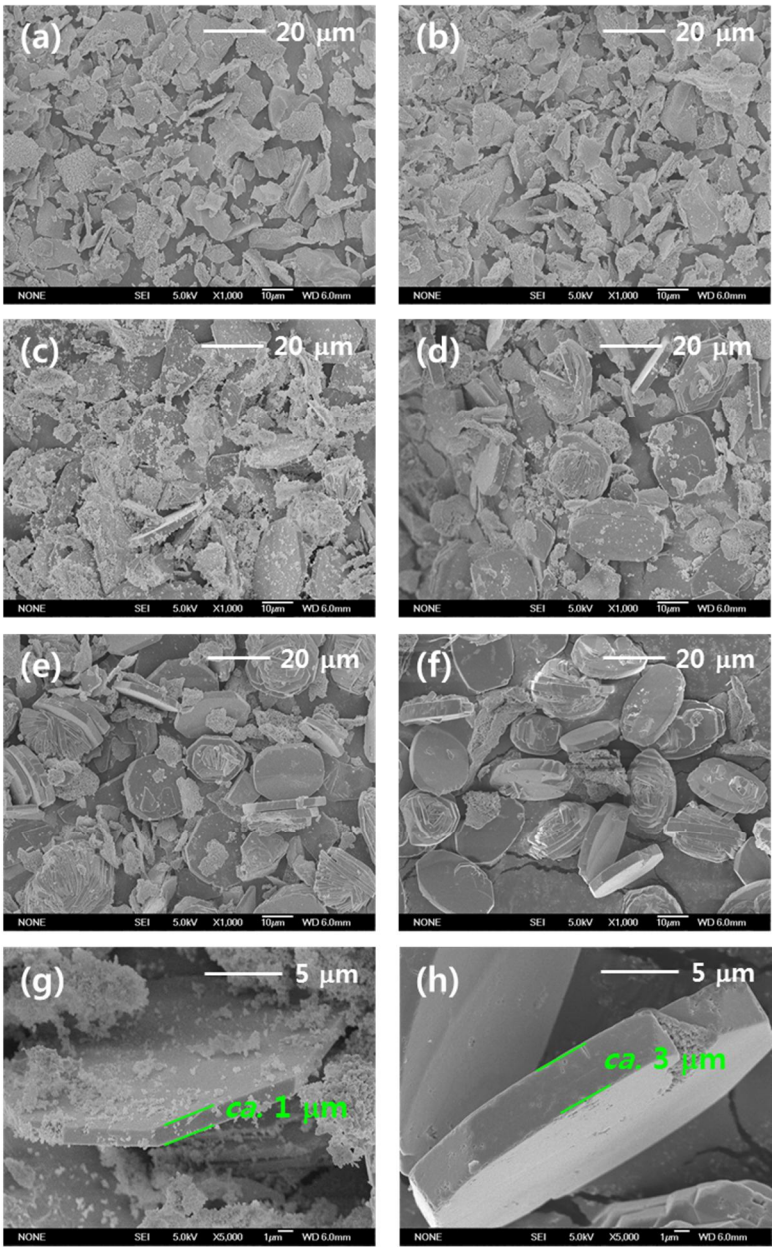

Figure II-8. FE-SEM images of the resulting materials with various reaction time; (a) 2 h, (b) 4 h, (c) 6 h, (d) 12 h, (e) 18 h, (f) 24 h, (g) higher magnification image of (c), and (h) higher magnification image of (f).

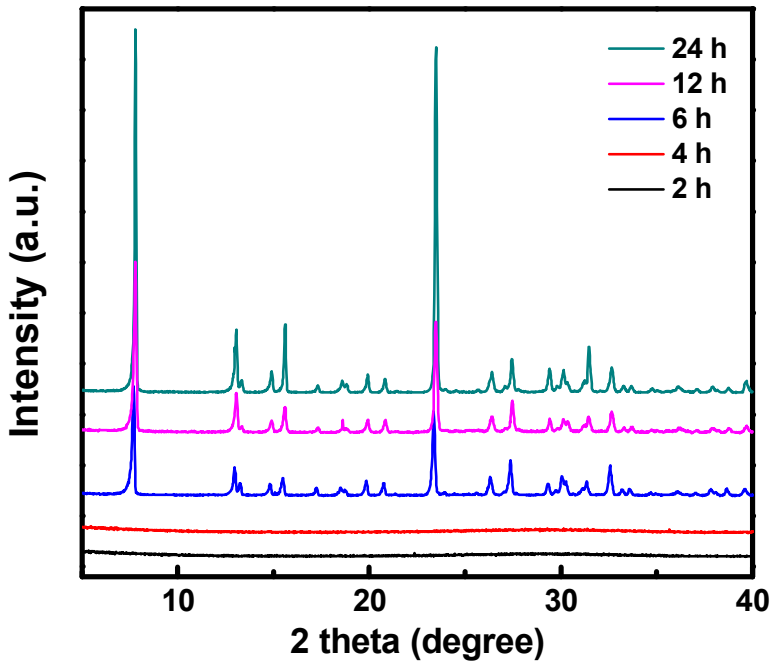

Figure II-9. XRD patterns for the resulting materials with various reaction time.

An outline of the synthesis mechanism of AMH-3 is shown in Figure II-10. In the early stage, the assembly of Si–O bonds process is mediated by hydrated strontium, which acts as coordination center for the construction of the framework. During this process, the initial gel is formed (white gel). When titanium is added, it is bound to the initial gel (purple gel). Titanium is released from the gel structure as it assemble and reorder the initial gel to form secondary gel (semi-ordered). Extensive nucleation occurs during formation of secondary gels. The nuclei develop to a critical size and then grow to small and uniform sized crystals. In this synthesis process, strontium and titanium act as structuring agent and assembly agent, respectively.

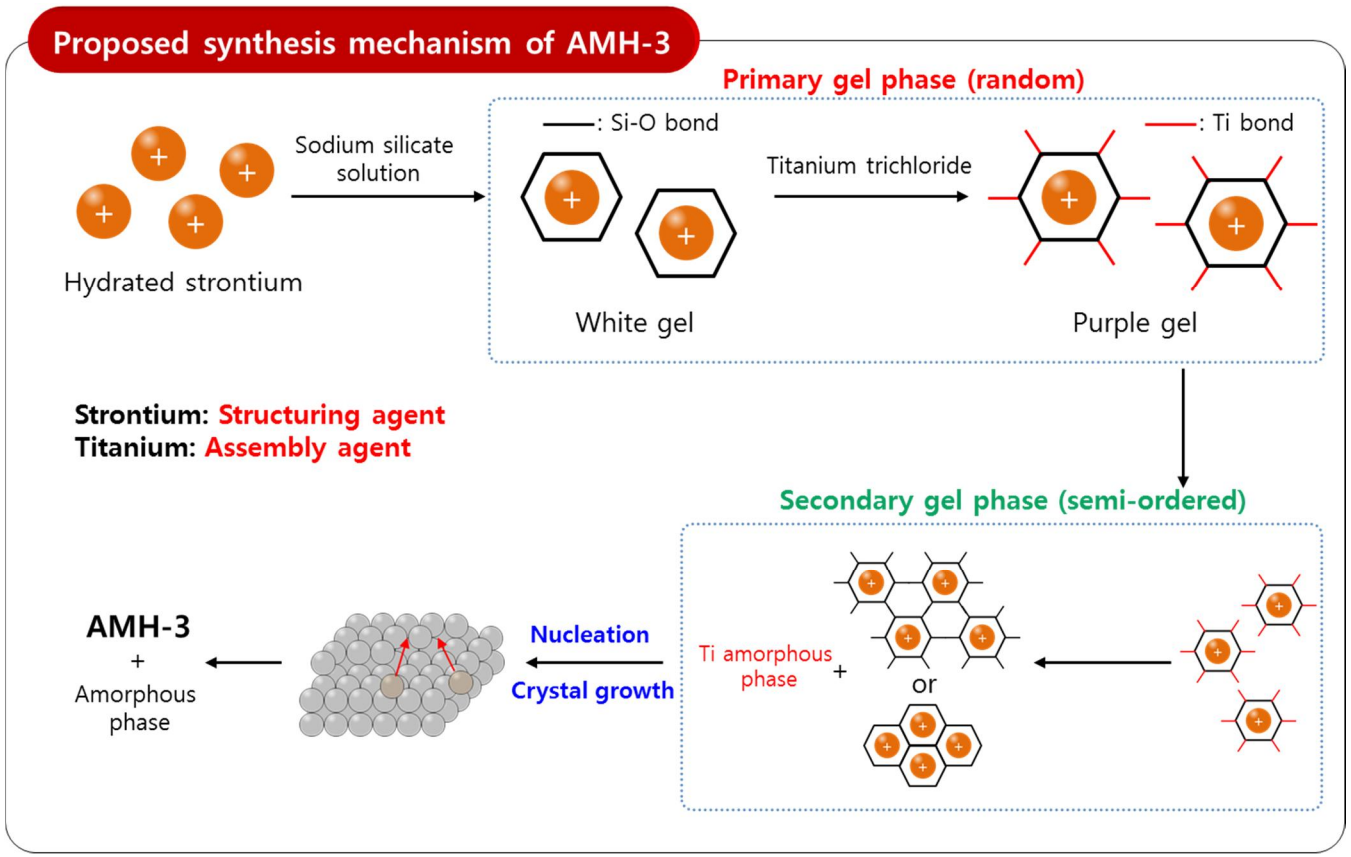

Figure II-10. Proposed synthesis mechanism of AMH-3.

II-4. Conclusion

In this study, synthesis and characterization of microporous layered silicate AMH-3 and its synthesis mechanism study were conducted. FE-SEM observation revealed that the morphology of AMH-3 was plate-like shape and its size was about 20 μm. The miller indices were calcalated based on XRD result and crystalline properties of AMH-3. ^{29}Si MAS NMR and Raman results showed that strontium and sodium were strongly bound the layer. The synthesis mechanism of AMH-3 was investigated by studying the effects of titanium, strontium, and reaction time on AMH-3 synthesis. XRD result showed that the presence of both titanium and strontium is essential to form AMH-3. In the synthesis process, strontium and titanium act as structuring agent and assembly agent, respectively.

CHAPTER III

ION EXCHANGE BEHAVIOR OF LAYERED SILICATE AMH-3 AND ITS APPLICATION AS SORBENT FOR HEAVY METAL IONS

III-1. Introduction

AMH-3 is composed of silicate layers containing eight-membered rings in all three principal crystal directions, spaced by Sr^{2+}, Na^{+}, and H_2O molecules [54]. AMH-3 possesses three-dimensional ordered microporosity from its pore structure and good acid, chemical and thermal stability from its lack of Si-O connections with any metal species such as titanium or aluminum. Because most researchers have focused on the 3-D microporosity of AMH-3, AMH-3 has been applied as a permselective barrier in gas separators [57, 69] and composite membranes for direct methanol fuel cells [70]. Besides the 3-D microporosity of AMH-3, it is notable that abundant cations exist in the pores and interlayers of AMH-3. The $Na_8Sr_8Si_{32}O_{76}\cdot 16H_2O$ unit cell formula of AMH-3 presents a theoretical ion exchange capacity of 7.30 mmol/g for

monovalent ions. Despite this excellent theoretical ion exchange capacity, no reports on the ion exchange behavior of AMH-3 and the applications exist.

The contamination of aqueous resources by heavy metals is becoming a severe environmental and public health problem because of the toxicity and non-biodegradability of heavy metal pollutants [71]. Heavy metals can be readily oxidized into ions when dissolved in aqueous solutions [72], and then easily enter the food chain through a number of pathways to cause toxic and adverse effects on ecological systems and human health [73]. Therefore, the removal of heavy metals from aqueous solutions is one of the major issues in most industries today. Various treatment methods have been developed for the purification of water and wastewater contaminated by heavy metals. Conventional treatment methods commonly used to remove metal ions from aqueous solutions include ion exchange, solvent extraction, membrane filtration, chemical precipitation, and adsorption [74–79]. Heavy metal ion exchange from the liquid phase with innocuous ionic species in a solid phase seems to be an attractive method owing to its low cost, simplicity, selectivity, and efficiency [80].

Aluminosilicate zeolites are one of the most attractive ion exchange media, and their cation exchange properties are widely used for sorbent, catalyst, and cation exchange applications [81–90]. Zeolites have a three-dimensional structure composed of tetrahedral SiO_4 and AlO_4 units connected by shared

oxygen atoms which forms ordered small pores containing H_2O molecules and abundant exchangeable cations [91]. Owing to these structural and chemical properties, zeolites possess high cation exchange capacity, element selectivity and specificity, and good thermal stability. The removal of heavy metals by ion exchange using natural and synthetic zeolites has been studied by many researchers [81–83]. However, zeolites can be dealuminated under acidic conditions, which leads to the destruction of their framework, and correspondingly decreases their removal efficiency [91].

Layered silicates such as magadiite, montmorillonite, and smectite have also been recognized as good ion exchangers [64, 91–93]. These materials have a large surface area derived from nanostructures composed of double SiO_4 tetrahedral nano-layers and cation containing interlayers, and good chemical and thermal stability. The cations in such layered silicates are exchangeable with heavy metals in aqueous solutions. In some cases, layered silicates can selectively remove heavy metals based on their uniform interlayer spacing [64]. However, layered silicates usually have low cation contents, which results in low cation exchange capacity.

Since AMH-3 has characteristics of both zeolite and layered silicate, it is expected that AMH-3 will not only efficiently remove heavy metals via ion exchange with its abundant cations, but that it also has potential for the selective removal of heavy metals owing to its uniform micropore and layered

structure. High acid and chemical stability of AMH-3 also can be helpful to remove heavy metals from acidic natural and industrial effluents. In addition, unlike other silica-based materials that have mesopores [94–97], AMH-3 do not need additional steps and costs for introducing functional groups that can adsorb heavy metals.

The objective of the present work was to study the ion exchange behavior of AMH-3 and the removal of heavy metals (Pb, Cu, Cd, and Zn) by AMH-3 from aqueous solutions under various experimental conditions and to examine the kinetics of sorption and other parameters involved.

III-2. Experimental Section

III-2-1. Materials

Strontium chloride hexahydrate ($SrCl_2 \cdot 6H_2O$, 99%, Junsei), titanium trichloride ($TiCl_3$, 20%, Kanto), sodium silicate solution (26.5% SiO_2, Sigma-Aldrich), sodium hydroxide (NaOH, 98%, Sigma-Aldrich), lead nitrate ($Pb(NO_3)_2$, 99%, Sigma-Aldrich), copper nitrate trihydrate ($Cu(NO_3)_2 \cdot 3H_2O$, 99%, Sigma-Aldrich), cadmium nitrate tetrahydrate ($Cd(NO_3)_2 \cdot 4H_2O$, 98%, Sigma-Aldrich), zinc chloride ($ZnCl_2$, 98%, Sigma-Aldrich) were used as received, without further purification. Highly deionized water (18 MΩ cm^{-1}) was used in all experiments.

III-2-2. Ion exchange study

To investigate whether the ion exchange process exists, the sorption of cations onto AMH-3 was carried out using Cu^{2+} aqueous solutions under batch conditions. The sorption of Cu^{2+} onto AMH-3 was studied as a function of its concentration at room temperature (25 ± 2 °C) by varying the initial Cu^{2+} concentration from 15 to 100 mg/L at pH 5–6. The sorption thermodynamics and kinetics of Cu^{2+} onto AMH-3 was also carried out. A summary of experimental conditions is given in Table III-1.

Table III-1. Experimental conditions.

Conditions	Thermodynamics-kinetics study	Kinetics study	Isotherms study
Concentration	10 mg/L	10 mg/L	10–200 mg/L
Time	10 min–3h	10 min–6h	12 h
Temperature	25–50 °C	25 °C	
pH		5–6	

III-2-3. Removal of heavy metal ions

The removal of heavy metal ions (Pb^{2+}, Cu^{2+}, Cd^{2+}, Zn^{2+}) by AMH-3 was studied using the batch method. All experiments were carried out at room temperature (25 ± 2 °C) and pH 5–6, each experiment was repeated at least twice; sorption isotherm and kinetic experiments were performed three times. Sorption capacity q (mg/g) and removal efficiency R (%) were calculated as follows:

$$q = \frac{(C_0 - C_e)V}{m} \quad (1)$$

$$R = \frac{(C_0 - C_e)}{C_e} \times 100 \quad (2)$$

where C_0 and C_e (mg/L) are the initial and the final concentration of the metal ion in the aqueous solution, respectively, V (L) is the volume of solution, and m (g) is the mass of the dry sorbent.

Sorption isotherm experiments were conducted by placing 10 mg of AMH-3 into 50 mL metal solutions of different initial concentrations (10–200 mg/L). After the mixtures were stirred for 12 h, they were filtered through 0.45-μm membrane filters. Sorption isotherms were determined using Langmuir and Freundlich models. The linear equations of Langmuir (Eq. (3)) and Freundlich (Eq. (4)) isotherm models can be expressed by the following

equations [35, 36]:

$$\frac{C_e}{q_e} = \frac{1}{q_m b} + \frac{C_e}{q_m} \quad (3)$$

$$lnq_e = lnK_f + \frac{1}{n} lnC_e \quad (4)$$

where C_e (mg/L) is the equilibrium concentration of the metal ion in solution, q_e (mg/g) is the amount of the metal ion at sorption equilibrium, q_m (mg/g) (saturated monolayer sorption capacity) and b (L/mg) (sorption equilibrium constant) are Langmuir constants, and K_f ((mg/g) $(L/mg)^n$) and n (unitless) are Freundlich constants.

The sorption kinetic experiments were carried out for various contact times (from 10 min to 6 h). 10 mg of AMH-3 were added to a 50 mL mixed solution containing 10 mg/L of each metal ion. The mixtures were filtered through 0.45-μm membrane filters and their metal concentration measured. The kinetics of metal ion sorption on the AMH-3 were analyzed using pseudo first-order and pseudo second-order kinetic models that are generally described as Eq. (5) and (6), respectively:

$$log(q_e - q_t) = logq_e - \frac{K_1 t}{2.303} \quad (5)$$

$$\frac{t}{q_t} = \frac{1}{K_2 q_e^2} + \frac{t}{q_e} \quad (6)$$

where q_e and q_t (mg/g) are the amount sorbed in equilibrium and at time t, respectively, and K_1 (1/min) and K_2 (g/mg·min) are rate constants.

Competitive sorption isotherms were measured to investigate the sorption properties of AMH-3 in a multi metal ion system (Pb^{2+} + Cu^{2+} + Cd^{2+} + Zn^{2+}). The experiments were conducted by following the same procedure as that described for the single metal ion sorption isotherm experiment using different initial concentrations of each metal ion (10–100 mg/L).

III-2-4. Characterization

The surface zeta-potentials were measured using a Photal ELS-8000 analyzer. The pH of the solution was adjusted to the desired value in the range 3–10 using 0.1 M HCl and NaOH. The morphology of the materials was examined with a field emission scanning electron microscope (JEOL, JSM-6700F) equipped with an energy-dispersive spectroscope working at 6 kV. Inductively coupled plasma atomic emission spectrometry (ICP-AES) measurements were performed with an Optima-4300 DV (PerkinElmer). ^{29}Si cross polarization magic angle spinning nuclear magnetic resonance (CP MAS NMR) measurements were performed on a Bruker Avance II spectrometer at room temperature (25 ± 2 °C). The recycle delay was 15 s,

with approximately 500 scans required for a full 7 mm rotor spinning at 7 kHz. X-ray diffraction (XRD) patterns of the samples were collected at room temperature (25 ± 2 °C) with a New D8 Advance (Bruker) diffractometer equipped with graphite monochromatized Cu-K_α radiation (λ= 1.541 Å) was used as the X-ray source.

III-3. Results and Discussion

III-3-1. Ion exchange behavior

The Cu^{2+} sorption capacity of AMH-3 increased with the initial concentration of Cu^{2+} to a maximum Cu^{2+} sorption capacity of 180.2 mg/g as shown in Figure III-1. Table III-2 shows the concentrations of exchangeable ions passed into the solutions from AMH-3. It was confirmed that Sr^{2+} and Na^{+} passed into the solutions, and the ratio of exchanged Sr^{2+} and Na^{+} to total sorbed Cu^{2+} was over 90%. These results indicate that the sorption process was governed by ion exchange between metal ions and Sr^{2+}/Na^{+} in AMH-3, and that the amount of sorbed metal ion was influenced by the amount of exchangeable cations in AMH-3. The variation in the contents of Na^{+}, Sr^{2+}, and Cu^{2+} within the AMH-3 were determined with ICP-AES and are summarized in Table III-3. The contents of Na^{+} and Sr^{2+} in the AMH-3 were significantly reduced and while that of Cu^{2+} was increased after the sorption of Cu^{2+} on AMH-3. The amount of increase in Cu^{2+} in the AMH-3 was similar to that of the decrease in cations and to the maximum sorption capacity of Cu^{2+} calculated from the concentration of residual ions in the experimental solution, which means that Na^{+} and Sr^{2+} in the original structure were exchanged with Cu^{2+}.

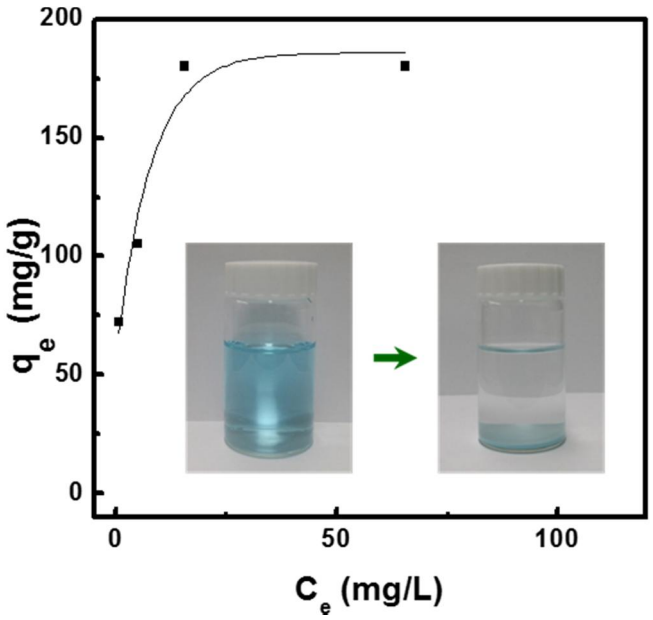

Figure III-1. Sorption isotherms of Cu^{2+} on AMH-3 plotted as equilibrium sorption capacity (q_e) vs. the equilibrium metal ion concentration (C_e) and photograph of Cu^{2+} aqueous solution before sorption (inset left) and after sorption (inset right).

Table III-2. Variation of concentrations of exchangeable ions with initial metal ion concentrations.

Initial metal concentration (mg/L)	Theoretically exchangeable ions (mg/g)		Exchanged ions (mg/g)		Sorbed Cu^{2+} onto AMH-3 (mg/g)
	Sr^{2+}	Na^{+}	Sr^{2+}	Na^{+}	
15	213.2	55.9	61.0	33.1	72.4
25			81.2	38.0	105.5
50			145.5	54.9	180.0
100			146.1	53.8	180.2

Table III-3. Cation contents (mg/g) of the samples.

Sample	Sr	Na	Cu
AMH-3 (Theoretical)	213.0	55.9	0
Pristine AMH-3	225.2	54.9	0
Cu-sorbed AMH-3	73.0	2.3	189.8

To elucidate the ion exchange behavior, the sorption thermodynamics and kinetics of Cu^{2+} onto AMH-3 was carried out. For an appropriate interpretation of experimental data, it is necessary to identify the steps that govern the overall removal rate in the sorption/ion exchange process. The ingenious mathematical treatment of Boyd et al. [98] and Reichenberg [99] to distinguish between the particle, and film diffusion and mass action controlled mechanism of exchange have laid the foundations for sorption/ion exchange kinetics. The three consecutive steps in the sorption of organic/inorganic compound by a porous sorbent are

(i) transport of the sorbate to the external surface of the sorbent (film diffusion);

(ii) transport of the sorbate within the pores of the sorbent except for a small amount of sorption, which occurs on the external surface (particle diffusion or intra-particle diffusion); and

(iii) sorption of the sorbate on the exterior surface of the sorbent.

It is generally accepted that the third process is very rapid and does not represent the rate-determining step in the uptake of sorbates. Three distinct cases occur for the remaining two steps in the overall transport:

Case I: External transport > internal transport, where rate is governed by film diffusion.

Case II: External transport < internal transport, where rate is governed by particle diffusion.

Case III: External transport ≈ internal transport, where the transport of ions to the boundary may not be possible at a significant rate, thereby, leading to the formation of a liquid film with a concentration gradient surrounding the sorbent particles.

External transport is usually rate limiting in systems, which have (a) poor mixing, (b) dilute sorbate concentration, (c) small particle size, and (d) high sorbate affinity for sorbent. In contrast, intra-particle transport limits the overall transfer for those systems that have (a) high sorbate concentration, (b) good mixing, (c) large sorbent particle size, and (d) low affinity of sorbate for sorbent [100].

Kinetic data was analyzed by the procedure given by Reichenberg [99] and Helfferich [101]. The following equations were used:

$$F = 1 - \frac{6}{\pi^2}\sum_{n=1}^{\infty}\frac{1}{n^2}\left[\frac{-D_i t \pi^2 n^2}{r_0^2}\right] \quad (7)$$

$$= 1 - \frac{6}{\pi^2}\sum_{n=1}^{\infty}\frac{1}{n^2}\exp[-n^2 Bt] \quad (8)$$

$$B = \frac{\pi^2 D_i}{r_0^2} \quad (9)$$

where F is the fractional attainment of equilibrium at time t ($F=q_t/q_e$), B is the time constant, D_i is the effective diffusion coefficient of metal ion, and r_0 is the radius of the sorbent particle, assumed to be shperical.

By applying Fourier transform and then integrating Eq. (8) for F(t) > 0.85 and F(t) ≤ 0.85, Reichenberg btained the approximations given by Eq. (3) and Eq. (4), respectively [99].

$$Bt = -\ln\frac{\pi^2}{6} - \ln(1 - F(t)) \qquad F > 0.85 \quad (9)$$

$$Bt = \left(\sqrt{\pi} - \sqrt{\pi - \frac{\pi^2 F(t)}{3}}\right)^2 \qquad F \leq 0.85 \quad (10)$$

The assumptions for these equations are:

1. F is a mathematical function of Bt and vice versa. The values of Bt may be plotted against the experimental values of t and a straight line (of B slope) passing through the origin should be obtained provided the diffusion coefficient D_i does not vary with F over the range of values involved;

2. For a given value of t, F depends only on D_i/r^2, i.e. F is independent of the concentration of solute ions;

3. For a given value of F, dF/dt and dq/dt are proportional to B.

The Bt values in Eq. (8) for values of F were obtained from Reichenberg's table [99]. The linearity test of Bt versus time plots is employed to distinguish between film and particle diffusion controlling sorption process. If the plot is a straight line passing through the origin, then the sorption rate is governed by particle diffusion mechanism otherwise it is governed by film diffusion mechanism. The Bt vs. time plots for Cu^{2+} at different temperatures were illustrated in Figure III-2. The plots were linear and pass through the origin, indicating the sorption process to be particle diffusion mechanism at all the studied temperatures. The effective diffusion coefficients were estimated from the slopes of the Bt plots using Eq. (9) and found to be 2.01×10^{-15} m^2/s (25 °C), 2.35×10^{-15} m^2/s (30 °C), 2.62×10^{-15} m^2/s (40 °C), and 3.01×10^{-15} m^2/s (50 °C). The increase of D_i with increasing temperature is mainly due to (i) the increased mobility of ions and a decrease in retarding forces acting on the diffusing ion and (ii) a consequence of forming the ion hydration shell and a reduction of the limitation for diffusion in the inner part of the pore system caused by the effective size of ion [102].

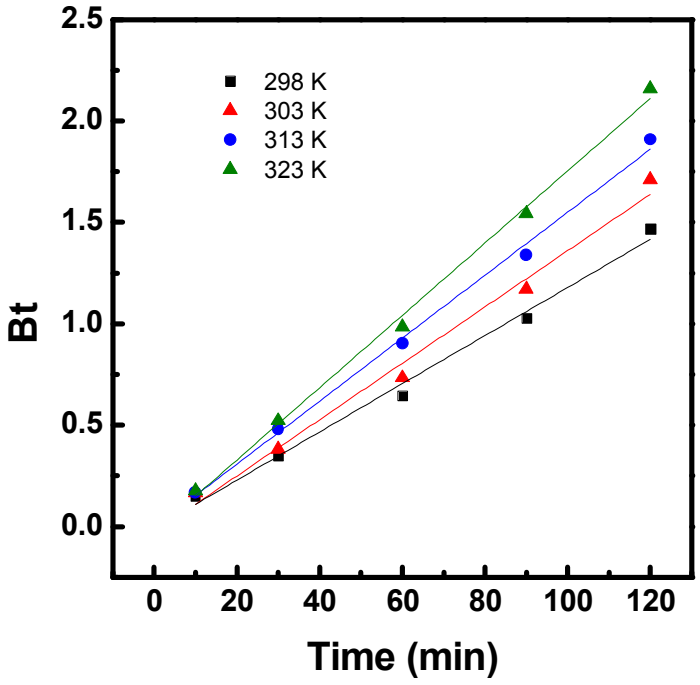

Figure III-2. *Bt* vs. time plots for the diffusion of Cu^{2+} onto AMH-3.

The activation energy E_a for the sorption of Cu^{2+} onto AMH-3 was determined using the Arrhenius equation:

$$D_i = D_0 \exp^{(-\frac{E_a}{RT})} \quad (10)$$

where, D_0 is a pre-exponential constant analogous to Arrhenius frequency factor and is found to be 2.74×10^{-13} m^2/s. The value of E_a was evaluated as 12.09 kJ/mol, which indicates that a chemical sorption process (ion exchange) consisting of weak interaction between sorbent (AMH-3) and sorbate (Cu^{2+}) and sorption process has a low potential energy.

The activation entropy ΔS^* for the sorption of Cu^{2+} onto AMH-3 was determined using the following equation:

$$D_0 = \left(\frac{2.72 d^2 kT}{h}\right) \exp\left(\frac{\Delta S^*}{R}\right) \quad (11)$$

where, k=Boltzmann constant; h=Planck constant; R=gas constant; d=distance between two active sites of the sorbent which is conventionally taken as 5 Å in inorganic ion exchangers, minerals and other adsorbents similar to carbon. The magnitude and sign of ΔS^* gives an indication whether the adsorption reaction is an associative or dissociative mechanism. The value of ΔS^* was estimated as –137.62 J/mol K. A negative value of ΔS^* suggests that the sorption process involves an associative mechanism. The sorption leads to

order through the formation of an activated complex between the sorbate and adsorbent. The negative ΔS^* values indicate the association of Cu ions with ion exchange sites in AMH-3, which leads to the formation of a stable chemical complex in the AMH-3. No significant change occurs in the internal structure of sorbent material during the sorption of ions [100, 103].

III-3-2. Characterization of ion exchanged AMH-3

The FE-SEM images of AMH-3 and Cu-exchanged AMH-3 (Cu-AMH-3) are shown in Figure III-3. Generally, ion exchangers with layered structures are less stable than exchangers with three-dimensional crystal structures because serious deformation of the layers can take place during ion exchange [104]. Similar to that of AMH-3, Cu-AMH-3 had a hexagonal plate-like shape, indicating that no deformation of the layers occurred during the ion exchange process.

^{29}Si CP MAS NMR spectroscopy was used to investigate the structural changes occurring during the ion exchange process. As shown in Figure III-4, the NMR peaks of Cu-AMH-3 were located at the similar position as those of AMH-3, with same Q^3/Q^4 ratio of approximately 3. The chemical shifts of Cu-AMH-3 are several ppm higher than those of AMH-3, which means that some cations between layers were exchanged with Cu. Ide et al. reported that a decreased NMR peak intensity was caused by substantial changes in the sorbent internal structure during the intercalation and/or exchange of cations, whereas a similar intensity after sorption meant no significant structural changes [64]. Therefore, the similar position, intensity, and integral ratio of the NMR peaks of Cu-AMH-3 to those of AMH-3 suggested that no significant change occurred in the structure of the AMH-3.

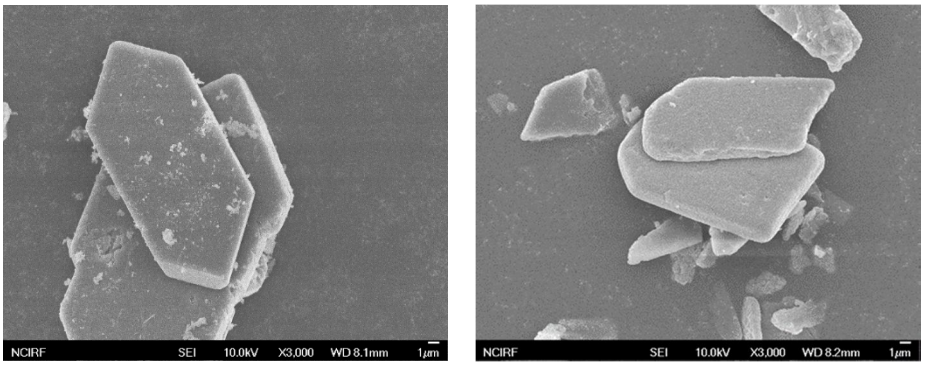

Figure III-3. FE-SEM images of AMH-3 (left) and Cu-AMH-3 (right).

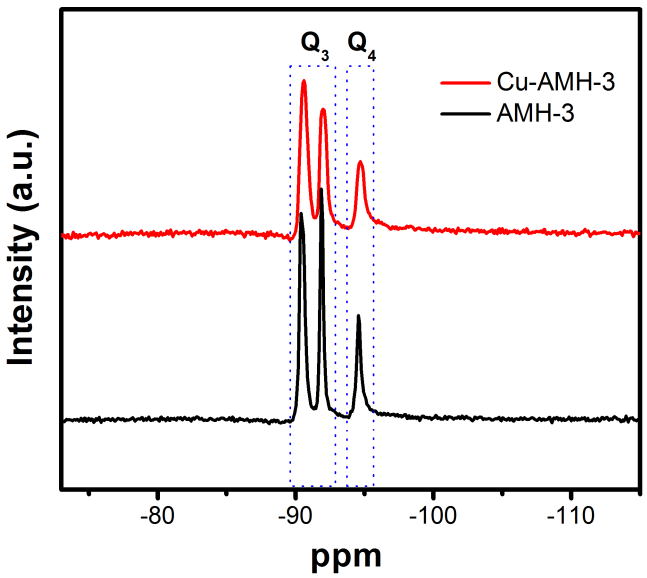

Figure III-4. ^{29}Si CP MAS NMR spectra of AMH-3 and Cu-AMH-3.

XRD was also used to characterize the structural changes occurring during the ion exchange process. Both of samples show the same XRD peak positions in Figure III-5, suggesting that the significant structural changes do not occur after the ion exchange. Beside, formation of Cu hydroxides was not observed. However, the peak intensities of Cu-AMH-3 were decreased compared to those of AMH-3. The ion exchange between Cu^{2+} and cations (Sr^{2+}, Na^{+}) located within the interlayer of AMH-3 leads to the increased distribution in basal spacing with the low uniformity of the layer alignment, resulting in the decrease of peak intensities of Cu-AMH-3.

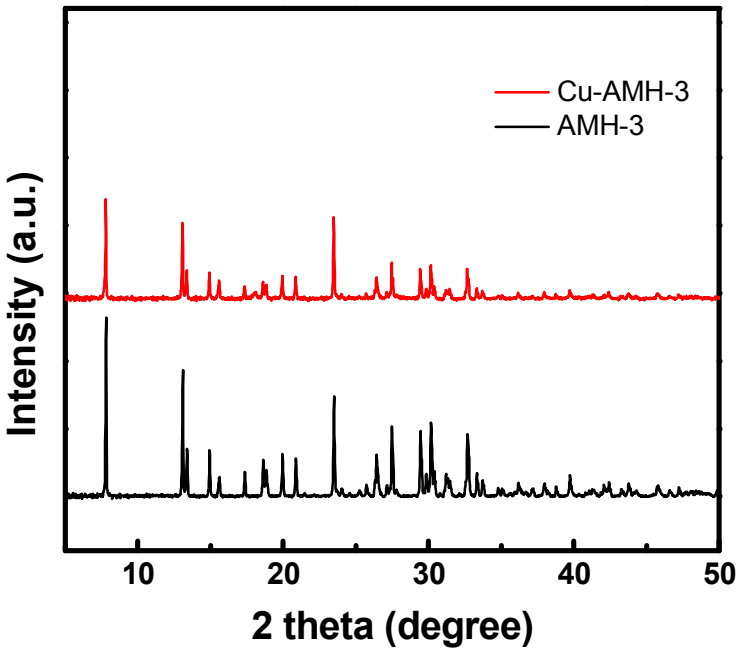

Figure III-5. XRD patterns for AMH-3 and Cu-AMH-3.

III-3-3. Removal of heavy metal ions

Sorption isotherm studies are important to elucidate how metal ions interact with AMH-3 and to investigate the maximum metal ion sorption capacities of AMH-3. The sorption capacity of metal ions by AMH-3 was found to be dependent on the initial metal concentration. As shown in Figure III-6, for all cases, the amount of metal (q_e) increased with an increase in the initial metal concentration during the same interaction time. However, the removal efficiency decreased with increasing initial metal concentration. The maximum amount of sorbed metal ions on AMH-3 reached 238.5 mg/g for Pb^{2+}, 180.3 mg/g for Cu^{2+}, 64.3 mg/g for Cd^{2+}, and 26.6 mg/g for Zn^{2+} at an initial metal concentration of 200 mg/L. Generally, at low initial metal concentration, the removal efficiency was over 90% and was barely affected by increases in initial metal concentration owing to the relatively abundant sorption sites on the sorbent. However, the removal efficiency for Cd^{2+} and Zn^{2+} was 17.9% and 21.9% at an initial metal concentration of 10 mg/L, while that for Pb^{2+} and Cu was 99.7% and 90.8%, respectively. These differences in removal efficiency may have been caused by the hydrated radius of the metal ion. AMH-3 is a microporous material with a uniform pore size and layered structure. If the hydrated radius of a metal ion is larger than the pore size of AMH-3, the hydrated metal ion could be excluded or some of the waters of hydration must be stripped from the hydrated metal ion before it can enter a

pore. The hydrated radius of the investigated metal ions is known to be 4.03 Å for Pb^{2+}, 4.19 Å for Cu^{2+}, 4.26 Å for Cd^{2+}, and 4.30 Å for Zn^{2+} [8, 9]. The above removal efficiency results indicate that the effective pore size of AMH-3 may be between the hydrated radius of Cu^{2+} and Cd^{2+}.

The sorption capacity (q_e) versus equilibrium metal concentration (C_e) curves for Pb^{2+}, Cu^{2+}, and Zn^{2+} reached equilibrium at low equilibrium metal concentration, whereas that of Cd^{2+} continuously increased with equilibrium metal concentration (Figure III-7). The calculated isotherm parameters of the Langmuir equation and Freundlich equation are listed in Table III-4. The sorption isotherms of Pb^{2+}, Cu^{2+}, and Zn^{2+} were well fitted to the Langmuir isotherm, which models monolayer coverage of the sorption surface. This model assumes that sorption occurs at homogeneous sorption sites on the sorbent. In contrast, the sorption isotherm of Cd^{2+} was well fitted to the Freundlich isotherm, which was derived to model multilayer sorption and sorption on heterogeneous surfaces. These results may be attributed to the hydrated radius of the metal ions. Based on the results of sorption capacity and removal efficiency as function of initial metal concentration, we postulate that the effective pore size of AMH-3 is similar to (or slightly smaller than) the hydrated radius of Cd^{2+}. The sorption of metal ions is controlled by three diffusion steps (step 1: from bulk solution to the film surrounding the sorbent, step 2: from the film to the sorbent surface, and step 3: from the surface to

internal sites) and the binding of the metal ions to the active sites [105]. At low initial concentration, Cd^{2+} was adsorbed onto the outer surface of AMH-3 (step 1, 2) rather than ion exchanged with cations in the pore (step 3) owing to its large hydrated radius. The sorption of Cd^{2+} onto the outer surface of AMH-3 gradually became saturated as the initial metal ion concentration was increased. After the outer surface (sorption site 1) was completely saturated with Cd^{2+} at high metal concentration, the Cd^{2+} may have tried to enter the pores (sorption site 2), resulting in a continuous increase in sorption capacity. Thus, the sorption isotherm of Cd^{2+} was well fitted by the Freundlich isotherm rather than the Langmuir isotherm. In the cases of Pb^{2+} and Cu^{2+}, the three diffusion steps occurred rapidly regardless of the metal concentration because of their smaller hydrated radius than the effective pore size of AMH-3, thereby leading to the observed high sorption capacity and reaching of equilibrium at low equilibrium metal concentration. In contrast, the third diffusion step did not occur during the sorption of Zn^{2+} owing to its larger hydrated radius, which caused a low sorption capacity of the AMH-3 for Zn^{2+}. The sorption capacities of Pb^{2+}, Cu^{2+}, Cd^{2+} and Zn^{2+} were compared with those of the other sorbents reported in literature (Table III-5). AMH-3 has a relative higher sorption capacities of heavy metals compared with most other sorbents, indicating that AMH-3 could well be used as a high performance sorbent.

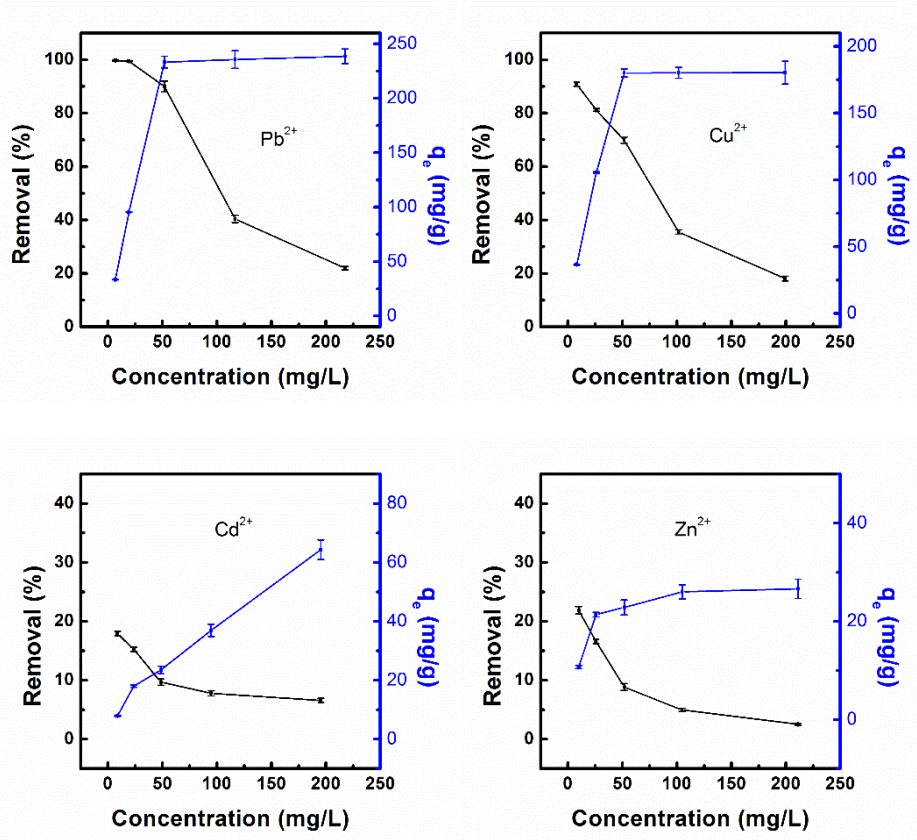

Figure III-6. Effect of the initial Pb^{2+}, Cu^{2+}, Cd^{2+}, and Zn^{2+} concentration on the percent amount of removal and on the qe of AMH-3.

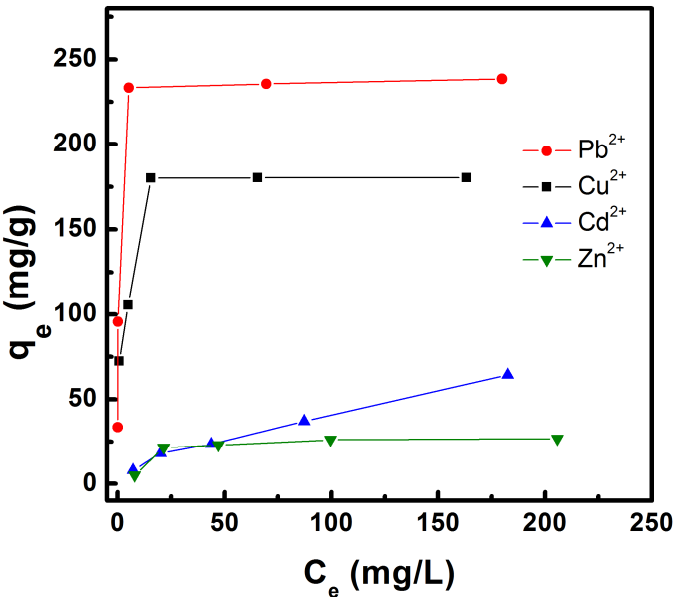

Figure III-7. Sorption isotherms of Pb^{2+}, Cu^{2+}, Cd^{2+}, and Zn^{2+} on AMH-3 plotted as q_e vs. C_e.

Table III-4. Results of sorption isotherms of heavy metals with AMH-3, following the Langmuir and the Freundlich equations.

	Langmuir			Freundlich		
	q_m (mg/g)	B (L/mg)	R^2	K_F	n	R^2
Pb^{2+}	238.66	3.7748	0.9999	108.64	4.996	0.7671
Cu^{2+}	182.15	0.6761	0.9995	84.09	5.601	0.7981
Cd^{2+}	93.37	0.0098	0.8229	2.43	1.610	0.9816
Zn^{2+}	27.97	0.1066	0.9990	7.72	3.867	0.7195

Table III-5. Comparison of heavy metals sorption capacities of various sorbents.

Sorbent	Sorption capacities (mg/g)				Reference
	Pb^{2+}	Cu^{2+}	Cd^{2+}	Zn^{2+}	
Activated carbon	26.94	4.45	3.37	–	[106]
Carbon nanotube	97.08	28.49	10.86	–	[107]
polysaccharide	73.76	21.16	24.39	17.78	[108]
Silica gel-based sorbent	87.02	36.85	57.33	31.38	[109]
Polymer modified magnetic nanoparticle	166.17	126.76	29.68	43.67	[110]
Polymer modified mesoporous silica	194.4	–	190.5	193	[95]
Hydrogel-based sorbent	201.39	54.45	93.86	–	[111]
Clinoptilolite	26.81	25.69	4.88	–	[112]
Jordanian zeolite	56.82	44.25	45.25	41.84	[113]
AMH-3	238.66	182.15	93.37	27.97	This work

The sorption kinetics is important for sorbent design, and is required for selecting optimum operating conditions for full-scale batch processes. Figure III-8 shows the results of the sorption kinetics experiments. The removal of metal ions by the AMH-3 was found to increase with contact time. The metal ion removal observed in the first 60 min was 78.5% for Pb^{2+} and 48.5% for Cu^{2+}, but only 9.8% for Cd^{2+} and 13.5% for Zn^{2+}. The maximum removal efficiencies of 99.5%, 90.8%, 17.9%, and 20.8% for Pb^{2+}, Cu^{2+}, Cd^{2+}, and Zn^{2+}, respectively, were obtained at a contact time of 6 h. The rate of sorption of heavy metals for AMH-3 was lower than that for nano-sized sorbent and polymer modified materials owing to its large particle size. There are several parameters that determine the rate of sorption, including the structural properties of the sorbent (size, surface area, porosity, and pore size), the properties of the metal ion (hydrated radius, ionic radius, and electronegativity), initial metal concentration, pH, and temperature. Because the same experimental conditions were used here with exception of the metal ion, the rate of metal ion sorption and the removal efficiency were mainly related to the hydrated radius of the metal ion. The rate of sorption and the removal efficiency were highest for Pb^{2+} owing to its smallest hydrated radius among the investigated metal ions.

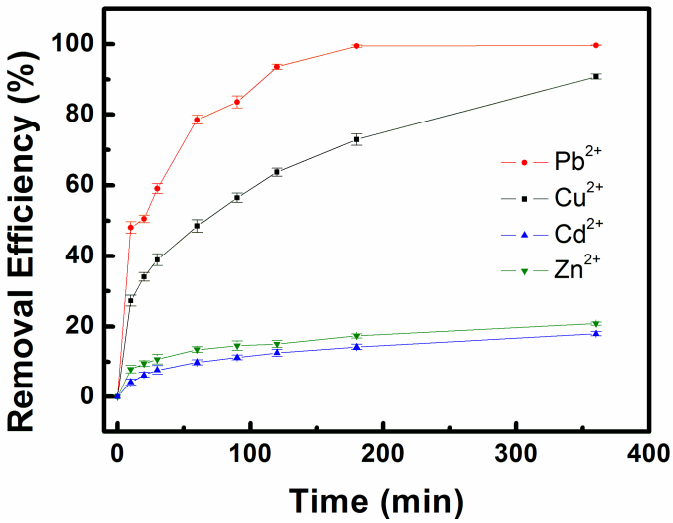

Figure III-8. Effect of the contact time on the percent amount of Pb^{2+}, Cu^{2+}, Cd^{2+}, and Zn^{2+} removal by AMH-3.

It is known that sorption processes can be dependent on and controlled with different kinds of mechanisms. To clarify the sorption process, several sorption models were applied to evaluate the obtained sorption kinetics experimental data. Herein, a pseudo-first-order kinetic model and pseudo-second-order kinetic model were used. The calculated kinetic parameters are given in Table III-6. The correlation coefficients were very high, and the experimental and calculated q_e values were very similar, which indicated that metal ion sorption on AMH-3 is well approximated by the pseudo-second-order model. Deviation occurred between the experimental and calculated q_e values for the pseudo-first-order model, and the correlation coefficients obtained were lower than those for the pseudo-second-order model. This confirmed that the pseudo-first-order model is not appropriate for predicting the sorption kinetics of metal ions on AMH-3. Therefore, the sorption of metal ions on AMH-3 may be a chemical process involving the sharing or exchange of electrons between the two species.

Table III-6. Sorption kinetic models rate constants for sorption of heavy metals on AMH-3.

	Pseudo first-order			Pseudo second-order			
	q_e (cal) (mg/g)	K_1 (1/min)	R^2	q_e (cal) (mg/g)	K_2 (g/mg min)	R^2	q_e (exp) (mg/g)
Pb^{2+}	52.33	2.99×10^{-2}	0.9046	49.36	1.55×10^{-3}	0.9911	48.40
Cu^{2+}	34.36	8.04×10^{-3}	0.9519	45.13	5.47×10^{-4}	0.9987	43.30
Cd^{2+}	6.41	8.06×10^{-3}	0.9496	8.42	2.31×10^{-3}	0.9976	7.92
Zn^{2+}	7.17	8.45×10^{-3}	0.8919	10.59	2.68×10^{-3}	0.9972	10.18

Investigating the sorption process in a multi metal system is important because natural and industrial effluents rarely contain only one kind of metal ion. The individual metal ion sorption capacity of a sorbent in a single metal system is generally lower than that in a multi metal system. Table III-7 shows the results of competitive sorption on AMH-3. Similarly to the results obtained in the single metal systems, the sorption capacity of the AMH-3 for Pb^{2+} and Cu^{2+} was higher than that for Cd^{2+} and Zn^{2+} owing to their smaller hydrated radius. Decreases in Cu^{2+}, Cd^{2+} and Zn^{2+} sorption capacity were observed when the initial concentration of the mixed metal ions was increased, which could be attributed to the higher selectivity of AMH-3 for Pb^{2+}. The competition for AMH-3 sorption sites in the presence of Pb^{2+} led to a decrease in the uptake of the other metal ions. The maximum sorption capacity, q_m (mg/g), values calculated using the Langmuir equation were in the order of Pb^{2+} (238.7) >> Cu^{2+} (182.1) >> Cd^{2+} (93.3) > Zn^{2+} (28.0) in the single metal systems, and Pb^{2+} (167.5) >> Cu^{2+} (84.0) > Zn^{2+} (7.7) > Cd^{2+} (1.9) in the multi metal system (Table III-8) The residual capacity ratios, calculated as the ratio of q_m in single and in multi metal systems, were in the order of Pb^{2+} (70.2%) > Cu^{2+} (46.1%) > Zn^{2+} (27.5%) > Cd^{2+} (2.0%). These results suggest that the coexistence of multiple metal ions reduced the sorption capacity of the AMH-3 for each metal ion owing to competition for sorption sites, and the sorption of Cd^{2+} and Zn^{2+} was more affected by the competing metal ions than Pb^{2+} and Cu^{2+}.

Table III-7. Sorption capacity (mg/g) in multi metal system.

	Initial metal concentration (mg/L)			
	10	25	50	100
Pb^{2+}	41.75	90.24	112.94	159.86
Cu^{2+}	41.19	87.72	86.18	83.37
Cd^{2+}	5.08	5.20	4.09	2.09
Zn^{2+}	8.86	9.16	8.68	7.85

Table III-8. Results of sorption isotherms of heavy metals with AMH-3 in multi metal system, following the Langmuir and the Freundlich equations.

	Langmuir			Freundlich		
	q_m (mg/g)	B (L/mg)	R^2	K_F (L/mg)	n	R^2
Pb^{2+}	167.5	0.18	0.9650	5.45	3.61	0.9769
Cu^{2+}	84.0	2031	0.9980	5.37	6.21	0.4604
Cd^{2+}	1.9	-0.07	0.9193	3.13	-2.79	0.5602
Zn^{2+}	7.7	-0.30	0.9959	2.75	-20.36	0.3397

III-4. Conclusion

In this study, the ion exchange behavior and the performance for the removal of heavy metals from aqueous solutions were investigated. The sorption of ion onto AMH-3 was governed by ion exchange rather than surface adsorption. Analysis of the thermodynamic-kinetic data revealed that the intraparticle diffusion was the determining step for the ion exchange and no significant change occured in the internal structure of the AMH-3 during the ion exchange. FE-SEM, ^{29}Si CP MAS NMR and XRD results show that no significant change occurred in the structure of the AMH-3 during the ion exchange. Single metal and multi metal sorption of heavy metals was performed in order to estimate the sorption behavior of heavy metals. The sorption isotherms of Pb^{2+}, Cu^{2+}, and Zn^{2+} were best described by the Langmuir model, while that of Cd^{2+} was best described by the Freundlich model. The sorption kinetics of all metal ions investigated were best modeled by a pseudo-second-order model. In competitive sorption, the selectivity of sorption on AMH-3 was in the order $Pb^{2+} > Cu^{2+} > Zn^{2+} > Cd^{2+}$. These sorption behaviors of heavy metals on AMH-3 were mainly dependent on the hydrated radius of the metal ions due to the microporous structure of AMH-3. Based on these results, AMH-3 may be an excellent potential sorbent for efficient and selective removal of heavy metals from aqueous solutions containing mixed metal ions.

CHAPTER IV

EFFICIENT REMOVAL OF CATIONS FROM LAYERED SILICATE AMH-3 FOR ACTIVATION OF MICROPORES

IV-1. Introduction

Layered silicates are widely used in various fields such as adsorption, catalysis, and the fabrication of nanocomposites [33–38, 114–116]. Several layered silicates have channel systems or open frameworks within layers [44–52], so these silicates can be used as permselective barriers. Of the known layered silicates, AMH-3 is an attractive candidate for preparing permselective barriers due to its 3D microporous framework and a high aspect ratio [54, 55]. However, although AMH-3 is a microporous framework material, it has been reported that AMH-3 exhibits almost no porosity when examined with N_2 adsorption and BET analysis [55, 56]. The reason for the absence of porosity under these conditions is that cations located in the intralayer and interlayer spaces block the pores [56]. Therefore, these cations must be removed from the AMH-3 if AMH-3 is to be used as the

permselective barrier. In addition, As a result of removal of cations, AMH-3 layers can be swollen or delaminated to increase their aspect ratio, which will provide good permselectivity. However, the removal of cations and the delamination of the interlayer are more difficult than for other layered materials because the Na^{+} and Sr^{2+} cations are strongly bound between the layers. Choi et al. and Kim et al. investigated an interlayer swelling method that uses swelling agents such as dodecylamine and dodecyldiamine [55–57]. However, these swelling agents have hydrophobic alkyl chains, so the resulting swollen AMH-3 is likely to be hydrophobic. The hydrophobic swelling agent is likely to interrupt the transport of water through the membrane containing the AMH-3, so the proton conductivity of the membrane is expected to be significantly lowered. A Nafion composite membrane with AMH-3 swollen by dodecylamine was investigated [117]. The swollen AMH-3/Nafion composite membrane was found to exhibit lower methanol permeability than neat Nafion. However, its proton conductivity was almost half that of neat Nafion. Therefore, AMH-3 must be swollen or delaminated without the use of a swelling agent to avoid hydrophobicity.

It has been reported that inorganic cations located between the layers of layered materials can be removed and/or exchanged with H^{+} by using acid treatment [118–120]. This exchange results in variation of the surface charge and leads to the expansion of the interlayers. Therefore, acid treatment could

be a candidate for the delamination of AMH-3 without the use of a swelling agent. However, Kim et al. have shown that complete proton exchange results in the collapse of the layered structure of AMH-3 [55]. Therefore, another post-treatment is required to maintain the AMH-3 layered structure. We chose the hydrothermal method to maintain the AMH-3 layered structure after acid treatment.

In this study, a simple method to remove cations within AMH-3 for activation of micropores and delaminate the AMH-3 layer without the use of a swelling agent will be discussed. The morphology of resulting materials was characterized by FE-SEM. ^{29}Si MAS NMR and FT-IR were used to characterize the structural changes occurring during the post-treatment process. For quantitative analysis of the effects of post-treatment, the variations of the cations contents were determined with ICP-AES and the specific surface area was estimated with the Brunauer-Emmett-Teller (BET) method using the nitrogen adsorption–desorption isotherm technique.

IV-2. Experimental Section

IV-2-1. Materials

Strontium chloride hexahydrate ($SrCl_2 \cdot 6H_2O$, 99%, Junsei), titanium trichloride ($TiCl_3$, 20%, Kanto), sodium silicate solution (26.5% SiO_2, Sigma-Aldrich), sodium hydroxide (NaOH, 98%, Sigma-Aldrich), hydrochloric acid (HCl, 37%, Sigma-Aldrich), Nafion perfluorinated ion-exchange resin (5 wt% solution in a mixture of lower aliphatic alcohols and water, Sigma-Aldrich) were used as received, without further purification. Highly deionized water (18 MΩ cm^{-1}) was used in all experiments.

IV-2-2. Removal of cations within AMH-3

A 1 g of AMH-3 was mixed with 100 mL of 1 M HCl aqueous solution. The mixed solution was magnetically stirred for 30 min, then transferred into a Teflon-lined stainless steel autoclave and heated at various temperature for 24 h. To evaluate the effects of the hydrothermal treatment, AMH-3 was immersed in 1 M HCl aqueous solution at room temperature (25 ± 2 °C) for 24 h. In this chapter, acid-treated AMH-3 is denoted A-AMH-3 and acid-hydrothermal treated AMH-3 is denoted AH-AMH-3

IV-2-3. Characterization

The morphology of the materials was examined with a fieldemission scanning electron microscope (JEOL, JSM-6700F) equipped with an energy-dispersive spectroscope working at 6 kV. Inductively coupled plasma atomic emission spectrometry (ICP-AES) measurements were performed with an Optima-4300 DV (PerkinElmer). The N_2 adsorption–desorption isotherms were measured with an ASAP2010 (Micromeritics). The specific surface area of each sample was determined by using the multiple-point Brunauer–Emmett–Teller (BET) method applied to the nitrogen desorption branch of the isotherm. ^{29}Si Magic-Angle Spinning Nuclear Magnetic Resonance (MAS NMR) measurements were performed on a Bruker Avance II spectrometer at room temperature (25 ± 2 °C). The recycle delay was 15 s, with approximately 500 scans required for a full 7 mm rotor spinning at 7 kHz. Fourier Transform Infrared Spectroscopy (FT-IR) spectra analyses were performed on samples pelletized with KBr powder by using a Thermo Scientific Nicolet 6700 IR spectrophotometer with a resolution of 4 cm^{-1}. Raman spectra were obtained using a DXR2xi equipped with a diode laser at 532 nm. Wide-angle X-ray diffraction (WXRD) patterns of the materials were collected at room temperature (25 ± 2 °C) with a MAC/Sci. MXP 18XHF–22SRA diffractometer equipped with graphite monochromatized Cu-Ka radiation (k = 1.541 Å, 50 kV, 100 mA) was used as the X-ray source.

IV-3. Results and Discussion

IV-3-1. Morphology and quantitative analysis

Figure IV-1 shows FE-SEM images of AMH-3, A-AMH-3, and AH-AMH-3. It can be seen that the interlayer space of AMH-3 has expanded; these morphologies are better than or similar to those of previously reported proton-exchanged and swollen AMH-3 [56, 57]. It is expected that our delaminated AMH-3 is unstable because there is no swelling agent binding to adjacent layers that occupies the interlayer space. However, it was previously reported that the structures of layered materials can be stabilized by hydrogen bonds without the presence of an alkali metal cation or a swelling agent [120]. Thus AMH-3 can be delaminated and the resulting morphology can be stabilized without the use of a swelling agent. The morphology of AH-AMH-3 contains more delamination than that of A-AMH-3 and A-AMH-3 has distorted flake, which means that the hydrothermal treatment plays an important role in the delamination process. We also examined the influence of HCl concentration and hydrothermal temperature on delamination process to find optimal experimental conditions. Figure IV-2 shows FE-SEM images of acid-hydrothermal treated AMH-3 with various HCl concentrations and hydrothermal temperatures. From these results, we find optimal conditions for delamination.

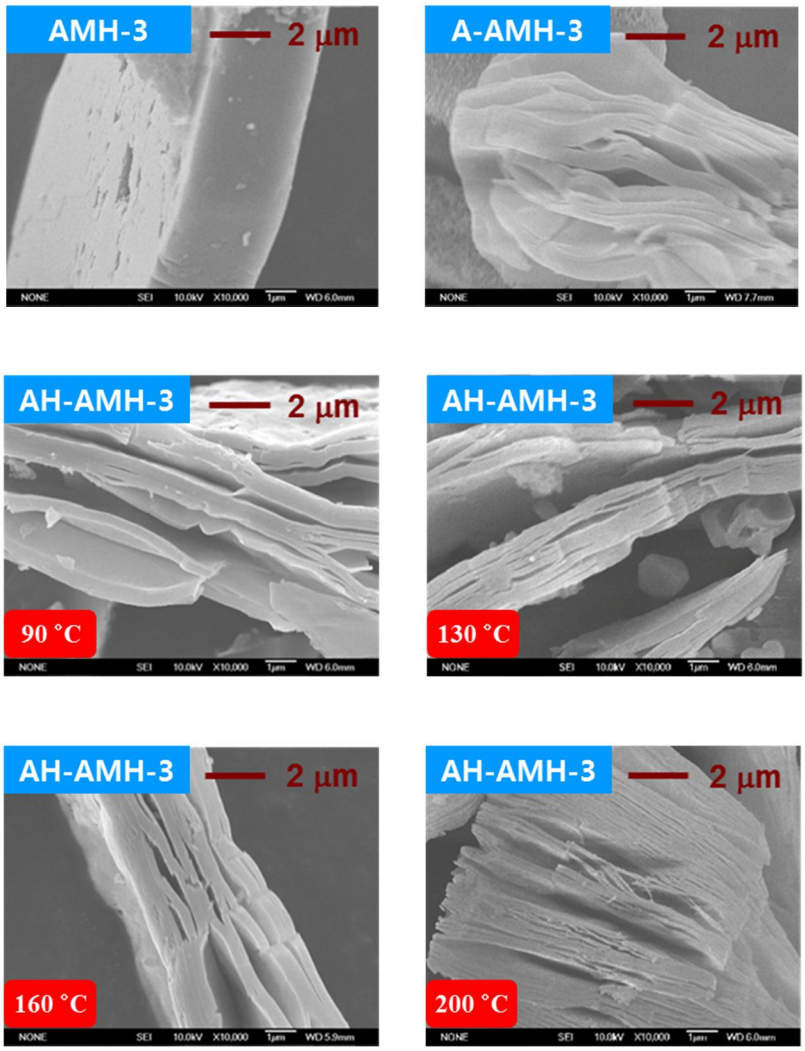

Figure IV-1. FE-SEM images of AMH-3, A-AMH-3, and AH-AMH-3 with hydrothermal reaction at various temperature.

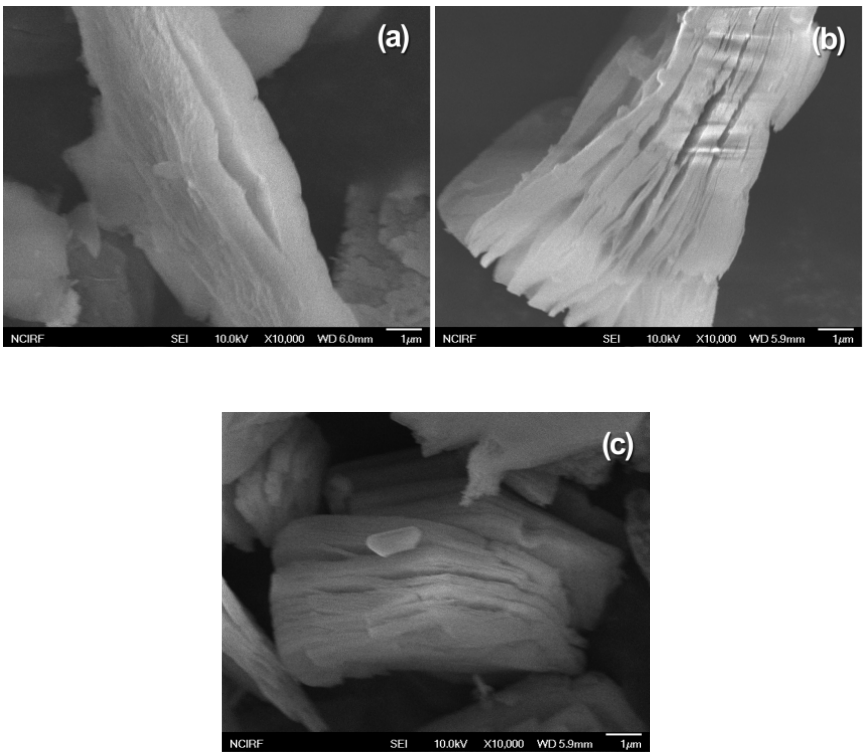

Figure IV-2. FE-SEM images of AH-AMH-3 with hydrothermal reaction at 200 °C in (a) 0.5 M HCl, (b) 1 M HCl, and (c) 1.5 M HCl

Figure IV-3 shows the nitrogen adsorption-desorption isotherms for all samples. All the isotherms of the samples except that of AMH-3 are of classical type IV with a H3-type hysteresis loop between the adsorption and desorption curves, which typically indicates the presence of mesopores according to IUPAC [121, 122]. These results indicate the interlayer mesoporosity caused by post-treatment (the acid or acid-hydrothermal treatments). The BET surface areas of the samples were found to be 19.26 m^2/g (A-AMH-3) and 117.26 m^2/g (AH-AMH-3). The BET surface area of AMH-3 was not calculated. These increases in surface area are ascribed to the removal of cations and the delamination of AMH-3. However, A-AMH-3 has a much smaller BET surface area than AH-AMH-3, which indicates that the acid-hydrothermal treatment is more effective at delamination than the acid treatment. For quantitative analysis of the effects of post-treatment, the variations of the Na and Sr contents in the regions between the AMH-3 layers were determined with ICP-AES. Our results are summarized in Table IV-1, which shows the Na and Sr contents of all the samples and those previously reported for proton-exchanged AMH-3 [56]. It is evident that the contents of Na and Sr in each sample are reduced by post-treatment. The cation contents of AH-AMH-3 are smaller than those of A-AMH-3 and proton-exchanged AMH-3 by amino acid. This results indicate that of these post-treatment methods, the acid-hydrothermal treatment is most effective in the exchange of cations.

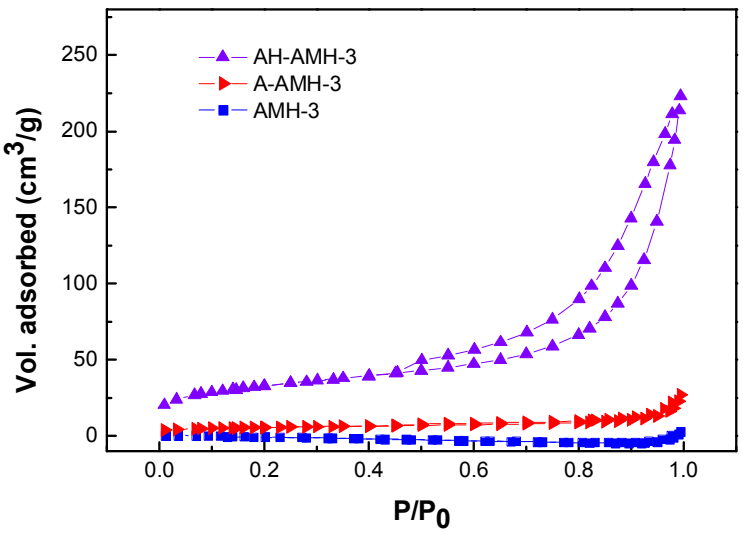

Figure IV-3. N_2 absorption isotherms of AMH-3, A-AMH-3, and AH-AMH-3.

Table IV-1. Cation contents (wt%) of the samples.

Sample	Sr	Na
AMH-3 (Theoretical)	21.30	5.59
AMH-3	22.52	5.49
A-AMH-3	2.46	0.10
AH-AMH-3	0.10	0.04
Proton-exchanged AMH-3 by amino acid [a]	3.13	0.72

[a] Previously reported data [56]

IV-3-2. Structural analysis

^{29}Si MAS NMR spectroscopy was used to characterize the structural changes that occur during the post-treatment process. An analysis of the ^{29}Si MAS NMR spectra of AMH-3 and swollen AMH-3 was carried out in a previous study [54–57]. As can be seen in Figure IV-4, the NMR spectrum of AMH-3 contains three peaks located at -89, -90, and -93 ppm, which correspond to Q^3 and Q^4 Si species as shown in the figure, with a Q^3/Q^4 ratio of approximately 3. On the other hand, the spectra of A-AMH-3 and AH-AMH-3, contain two peaks at -102 ppm (Q^3) and -112 ppm (Q^4), resulting in a Q^3/Q^4 ratio of approximately 1. As reported previously, such changes in peak position and the Q^3/Q^4 ratio are related to structural changes in the silicate materials. The Q^3/Q^4 ratio decreases from 3 for AMH-3 to 1 for A-AMH-3 and AH-AMH-3. This decrease in the Q^3/Q^4 ratio corresponds to a structural reordering and the increased condensation of the silicate framework. The reason for the decrease in the Q^3/Q^4 ratio is as follows: since the Na and Sr cations are exchanged by the acid and acid-hydrothermal treatments, negatively charged Q^3 species on the layer surfaces that are charge balanced with cations become condensed to Q^4 species. Therefore, the Q^3/Q^4 ratio changes, which reflects the structural changes that occur during the post-treatment process. Such structural changes can be explained in terms of intralayer or interlayer condensation [55–57].

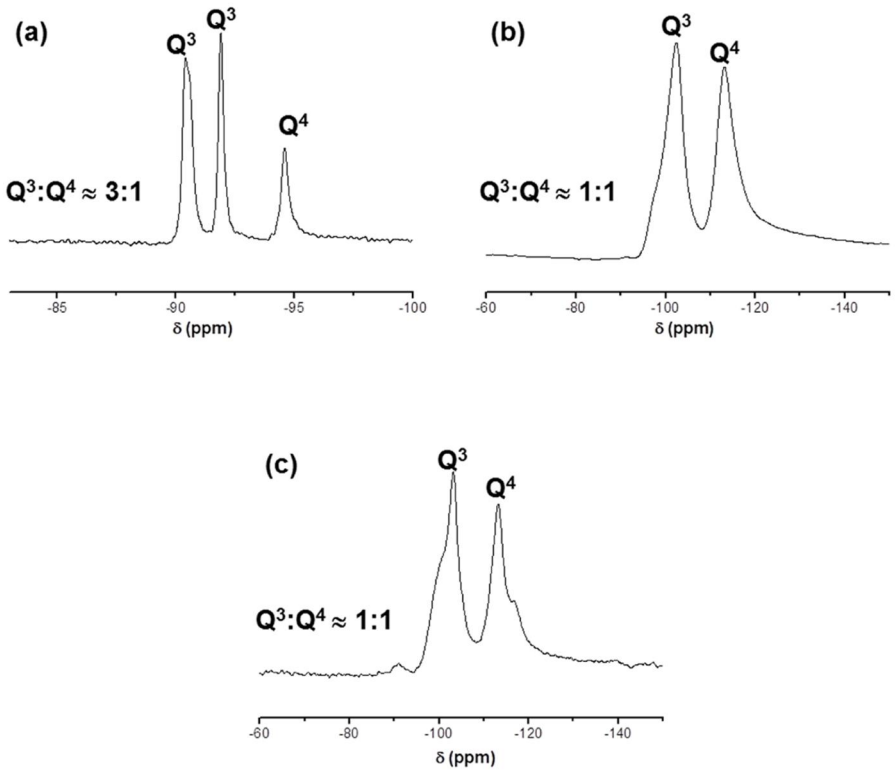

Figure IV-4. ^{29}Si MAS NMR spectra of (a) AMH-3, (b) A-AMH-3, and (c) AH-AMH-3

On the basis of the BET results obtained in this work, we suggest that in the case of AH-AMH-3, which has a large BET surface area, the Q^4 species are mainly formed by intralayer condensation of the Q^3 species in the individual layers in AMH-3 rather than by interlayer condensation between the adjacent layers. On the other hand, the small BET surface area of A-AMH-3 reflects the decreased mesoporosity of A-AMH-3 that results from interlayer condensation. Thus the hydrothermal treatment leads to intralayer condensation rather than interlayer condensation during the post-treatment process, which increases the degree of delamination (Figure IV-5). Kim et al. reported molecular models of the layers of AMH-3 and swollen AMH-3 that were obtained by measuring the Q^3/Q^4 ratios [55]. For these models, the molecular model with a Q^3/Q^4 ratio of 1 has a more ordered pore structure as shown in Figure IV-6. Therefore, after the post-treatment process AMH-3 may has a more ordered pore structure and this ordered pore structure will improve transport of water through the AMH-3 layers when AMH-3 is used as a permselective barrier.

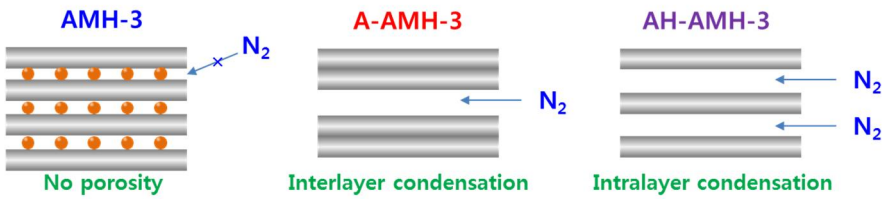

Figure IV-5. Role of hydrothermal treatment in the removal of cations within AMH-3.

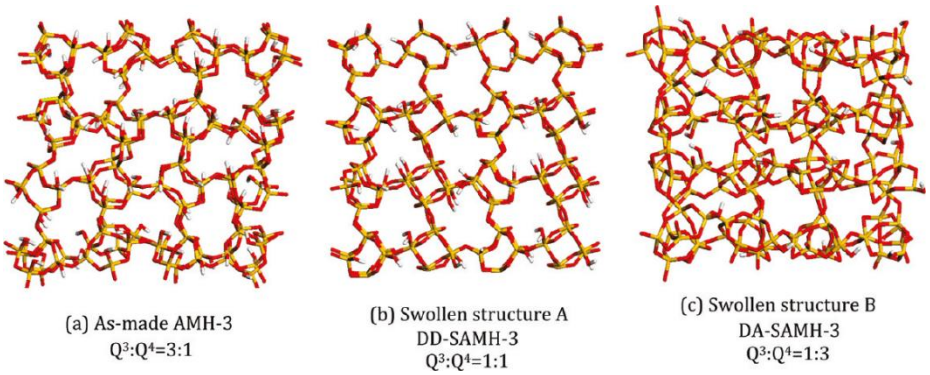

Figure IV-6. Simulated structural changes in AMH-3 during the swelling process. The figures show top views of a single layer of AMH-3 [55].

FT-IR spectroscopy was also used to characterize the structural changes occurring during the post-treatment process. The FT-IR spectra were assigned on the basis of previous assignments [55–57]. The FT-IR spectra of AMH-3, A-AMH-3, and AH-AMH-3 are displayed in Figure IV-7. In the region between 4000 and 2500 cm^{-1} of Figure IV-7, the absorption bands corresponding to the water and hydroxyl groups can be seen. The hydroxyl group bands near 3500 cm^{-1} appear after the post-treatment process, and are attributed to the hydroxyl groups from adjacent silicate layers. Hydroxyl groups that are present with water in the interlayer lead to a disordered interlayer structure [56]. As mentioned above, negatively charged hydroxyl groups also lead to a variation in the surface charge, which results in an expansion of the interlayer spaces. However, as shown in the FE-SEM images, the hydrogen bonds between the hydroxyl groups and water stabilize the structure. In Figure IV-7, the characteristic bands due to the silicate structure can be seen between 1400 and 400 cm^{-1}. The bands in the frequency range 1150–1000 cm^{-1} due to the Q^3 external linkages are replaced by a single band and broadened for A-AMH-3 and AH-AMH-3; a new band corresponding to the condensed Q^4 linkages is present near 1300 cm^{-1}. These results are consistent with the ^{29}Si MAS NMR results, and show that Q^3 species have condensed to Q^4 species during the post-treatment process. Kim et al. reported that the FT-IR bands in the range between 750 and 500 cm^{-1} are

associated with the crystallinity of the silicate frameworks and that the disappearance of these bands corresponds to the significant structural disorder that occurs as a result of the swelling process [55]. In contrast, in our approach the silicate framework bands are still present after the post-treatment process, which means that structural disorder does not arise and that the crystallinity of the silicate framework is maintained during the removal of cations. The bands below 500 cm^{-1} correspond to four-membered rings (4-MRs) and are present for all samples, which reflect the preservation of the 4-MRs within the layers.

Figure IV-8 shows the Raman spectra of AMH-3, A-AMH-3, and AH-AMH-3. The bands below 300 cm^{-1} were assigned to Na–O stretching modes and Si–O–Si bending mode. The bands between 400 and 300 cm^{-1} were assigned to Sr–O stretching modes and pore opening modes of the 8-MRs [66]. Since strontium and sodium were removed from AMH-3 structure during the post-treatment process, the bands in this region were attributed to the pore framework, not Na–O and Sr–O stretch. The bands correspond to 4-MRs (between 700 and 400 cm^{-1}) were maintained after post-treatment. As with the FT-IR results, the Raman results indicate that the crystallinity of the framework is maintained during the post-treatment process.

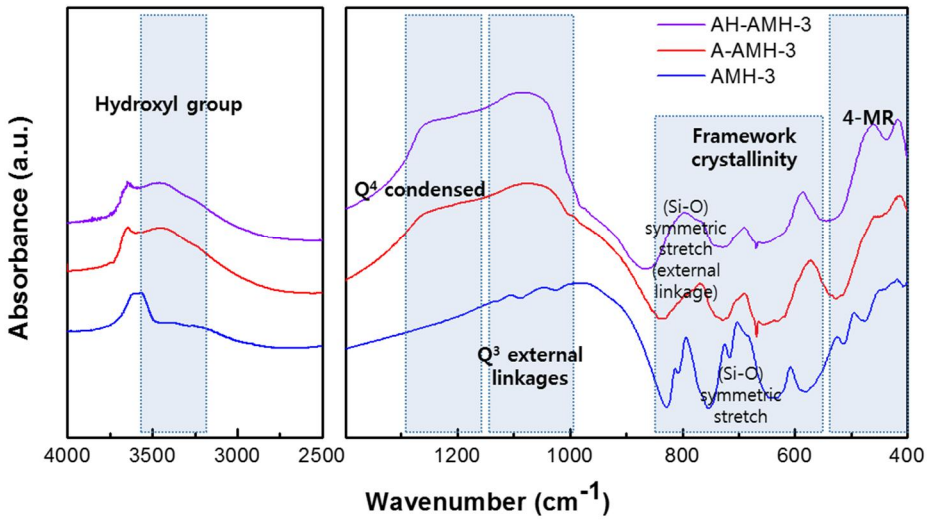

Figure IV-7. FT-IR spectra of AMH-3, A-AMH-3, and AH-AMH-3.

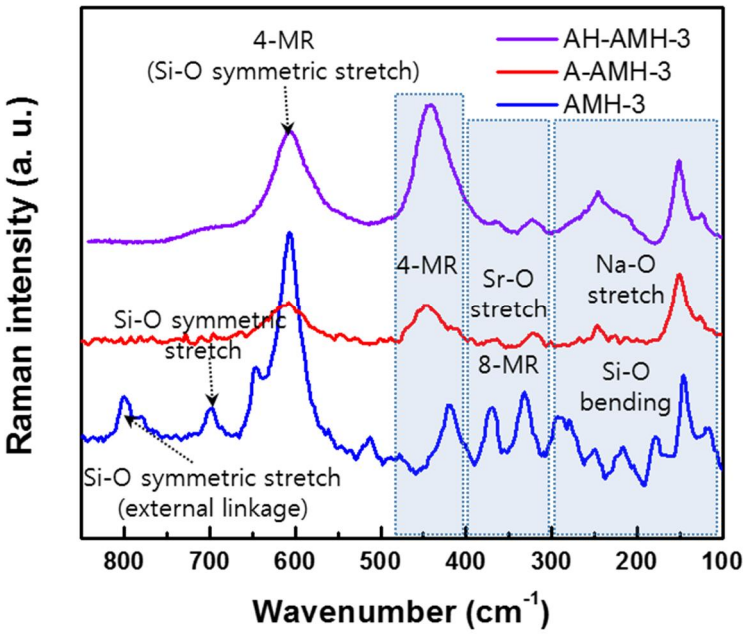

Figure IV-8. Raman spectra of AMH-3, A-AMH-3, and AH-AMH-3.

The XRD patterns of all samples are shown in Figure IV-9. Comparing the XRD patterns of the samples with that of AMH-3, it can be seen that the XRD patterns have changed and broadened. XRD is highly sensitive to the degree of order within silicate layer stacks [123, 124]. During the post-treatment process, the d-spacing distribution becomes broader and the uniformity of layer structure and alignment is decreased due to the coexistence of hydroxyl groups and water in the interlayer spaces and the variation in the surface charge; these effects result in the changing and broadening of the XRD patterns.

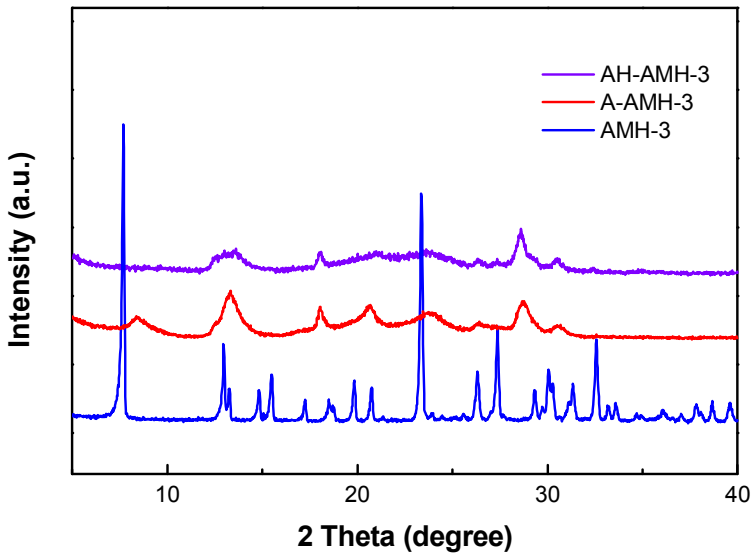

Figure IV-9. XRD patterns for AMH-3, A-AMH-3, and AH-AMH-3.

IV-4. Conclusion

We developed a simple method to remove cations within AMH-3 for activation of micropores and delaminate the AMH-3 layer by means of acid and acid-hydrothermal treatments, without the use of a swelling agent. Although hydroxyl groups and water within the interlayer space can cause disordering of the interlayer in the absence of a swelling agent, the structure of delaminated AMH-3 can be stabilized by the hydrogen bonds between them. Both post-treatments lead to structural changes due to intralayer and interlayer condensation. ^{29}Si MAS NMR, FT-IR and Raman results show that the pore structure of delaminated AMH-3 is more ordered and that the crystallinity of individual layers is almost unchanged in contrast to the significant structural disorder that occurs during swelling processes. In addition, BET analysis showed that the hydrothermal treatment leads to intralayer condensation rather than interlayer condensation during the post-treatment process, which results in an increase of the degree of delamination.

CHAPTER V

NAFION/LAYERED SILICATE AMH-3 COMPOSITE MEMBRANE WITH SANDWICH-TYPE STRUCTURE FOR VANADIUM REDOX FLOW BATTERIES

V-1. Introduction

Recently, with increasing concerns about environmental pollution and the depletion of fossil fuels, renewable energy sources such as solar power and wind energy have attracted considerable attention [125, 126]. However, since renewable energy is generated intermittently, there is a mismatch between generated power and the demand and actual consumption of power. One of solutions to this problem is ecofriendly and high-efficiency energy-storage systems (ESSs) that can match the energy supply with consumption and demand [127]. Among these ESSs, redox flow batteries (RFBs) are regarded as the most suitable candidate for these applications because of their long lifespan, flexible design, high efficiency, and short response time [128–131]. Unlike traditional batteries that store energy in electrode materials, RFBs store incoming energy in the form of two dissolved redox pairs that convert

into electricity at the electrodes. Figure V-1 shows available redox couples and their standard potentials in aqueous systems [130]. Generally, a RFB cell, shown schematically in Figure V-2, consists of two electrodes and circulating positive and negative electrolyte solutions separated by an ion exchange membrane [127]. The energy conversion between electrical energy and electrochemical energy occurs as the liquid electrolytes are pumped from storage tanks to flow-through electrodes in the cell.

Among the RFB systems, the all-vanadium redox flow battery (VRB) demonstrates excellent electrochemical activity and reversibility [132]. A VRB uses V^{2+}/V^{3+} redox couples at the anode side and a V^{4+}/V^{5+} redox couples at the cathode side, preventing the cross-mixing between the electrolytes through the ion exchange membrane. The energy conversions are ouccred via changes in vanadium valence states through the following reactions:

Cathode: $VO_2^+ + 2H^+ + e^- \underset{\text{Charge}}{\overset{\text{Discharge}}{\rightleftharpoons}} VO^{2+} + H_2O$

Anode: $V^{2+} - e^- \underset{\text{Charge}}{\overset{\text{Discharge}}{\rightleftharpoons}} V^{3+}$

Cell: $VO_2^+ + V^{2+} + 2H^+ \underset{\text{Charge}}{\overset{\text{Discharge}}{\rightleftharpoons}} VO^{2+} + V^{3+} + H_2O$

The overall electrochemical reaction gives a standard cell voltage of 1.26 V at 25°C.

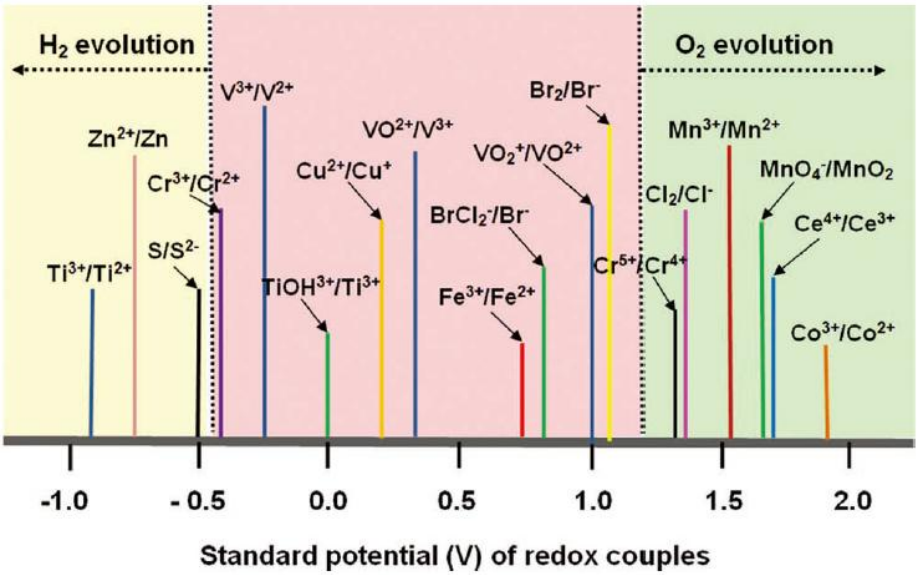

Figure V-1. Standard potential (vs. the standard hydrogen electrode) of redox couples, except the H_2 evolution potential, which is the over-potential at the carbon electrodes. Reproduced with permission [130].

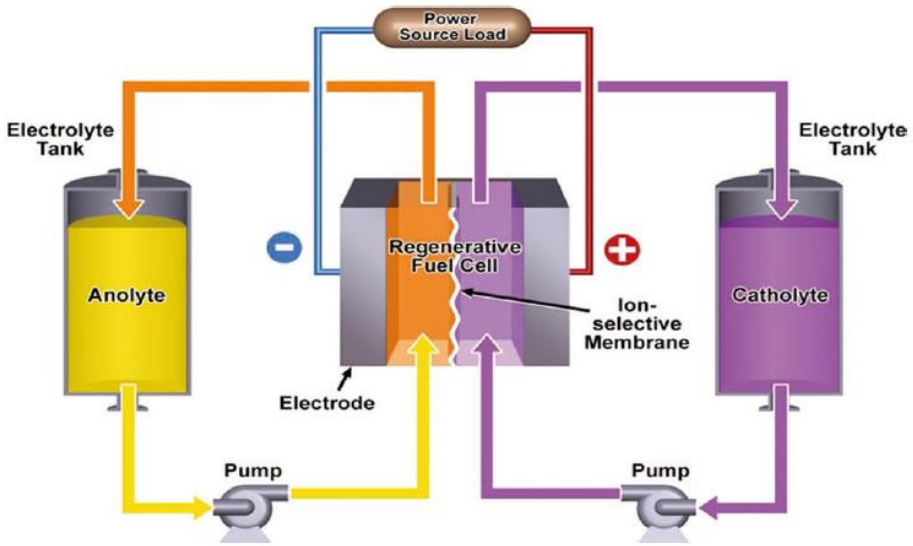

Figure V-2. Schematic of the structure of a redox flow battery [127].

Ion exchange membranes (IEMs) are a key component of VRB systems. IEMs are employed to separate the positive and negative electrolytes and allow ion transport to complete the current circuit [133, 134]. An ideal IEM should possess low vanadium ion permeability, high proton conductivity, and good chemical stability [135–137]. The membranes most commonly used in VRBs are perfluorosulfonic polymers, such as Nafion, which offers high proton conductivity and good mechanical and chemical stability under strongly acidic conditions. However, Nafion suffers from vanadium crossover during cell operation, causing a reduction of the cell efficiency of VRB system [138]. The performance of VRB may be improved by reducing vanadium crossover through Nafion. Significant efforts have been applied toward the reduction of vanadium crossover by modifying Nafion. Inorganic materials have been introduced into Nafion clusters [139–141], Nafion surfaces have been modified [138], and Nafion has been blended with other polymers [142–144]. Among these methods, the incorporation of inorganic particles such as silicon oxide and titanium oxide is a simple way to reduce the vanadium crossover. A porous material can effectively reduce the vanadium crossover among the inorganic particles while minimizing the drop in proton conductivity owing to their unique structure.

Microporous layered silicate AMH-3 is permselective and has been applied in gas separators [57, 145, 146] and direct methanol fuel cells [117, 147]. In

chapter IV, we successfully removed the cations within AMH-3 for activation of micropores in order to use as permselective barrier. In this study, a Nafion-based composite membrane having a D-AMH-3 layer was prepared by solution casting and hot pressing. The performance of Nafion in a VRB has been shown to depend on the membrane thickness [148, 149]. Thus, in order to examine the effect of D-AMH-3 layer, we controlled the thickness of the Nafion/D-AMH-3 membrane, which is similar to the thickness of a neat Nafion.

V-2. Experimental Section

V-2-1. Materials

Strontium chloride hexahydrate ($SrCl_2 \cdot 6H_2O$, 99%, Junsei), titanium trichloride ($TiCl_3$, 20%, Kanto), sodium silicate solution (26.5% SiO_2, Sigma-Aldrich), sodium hydroxide (98%, Sigma-Aldrich), hydrochloric acid (HCl, 37%, Sigma-Aldrich), Nafion perfluorinated ion-exchange resin (5 wt% solution in a mixture of lower aliphatic alcohols and water, Sigma-Aldrich) were used as received, without further purification. Nafion 117 membrane (N117) was purchased from Dupont company. Highly deionized water (18 $M\Omega\ cm^{-1}$) was used in all experiments.

V-2-2. Membrane preparation

AMH-3 was synthesized and delaminated according to the methods described in chapter IV. Nafion-based composite membrane with a D-AMH-3 layer was prepared by solution casting. N117 was swollen in ethanol solution for 1 day and then placed in glass dish. A 10 wt.% of D-AMH-3 was added into Nafion solution, then the mixture was stirred at room temperature (25 ± 2 °C) to yield a coating solution, which was slowly poured into glass dish

containing swollen N117. The filled glass dish was evaporated in an oven at 40 °C for 1 day. After drying, the filled glass dish was cooled in water, and then the membrane was peeled off. Finally, In order to form the well-ordered D-AMH-3 layer, the membrane was hot pressed between polyimide films at 130 °C and 3000 psi for 10 min. In this chapter, Nafion/D-AMH-3 membrane was termed as ND and Nafion/D-AMH-3 membrane with hot pressing was termed as NDP.

V-2-3. Characterization

The cross-section morphology of membranes was observed by a field-emission scanning electron microscope (JEOL, JSM-6700F) equipped with an energy-dispersive spectroscope. The cross-section samples were obtained by breaking membranes in liquid nitrogen.

To evaluate the water uptake and swelling ratio of the membranes, the membranes was soaked in deionized water for 24 h at room temperature (25 ± 2 °C). They were then taken out of the vessel and measured immediately after the surface was wiped with tissue paper to obtain the wet weight of the membranes. The membranes were dried under vacuum oven at 80 °C for 24 h.

The water uptake and swelling ratio of the membranes were calculated according to the following equations:

$$\text{Water uptake}\ (\%) = \frac{W_{\mathrm{w}} - W_{\mathrm{d}}}{W_{\mathrm{d}}} \times 100\% \quad (1)$$

$$\text{Swelling ratio}\ (\%) = \frac{L_{\mathrm{w}} - L_{\mathrm{d}}}{L_{\mathrm{d}}} \times 100\% \quad (2)$$

where W_{w} and W_{d} are the weight of the membrane after and before water absorption, respectively; L_{w} and L_{d} are the length of the membrane after and before water absorption, respectively.

The ion exchange capacity (IEC) of the membranes was determined by conventional titration method. Employing 50 mL saturated NaCl solution as the ion exchange agent, the amount of H^+ exchanged from the membranes was determined by titrating with 0.1 M NaOH solution, using phenolphthalein as indicator. The IEC of membranes was calculated by following equation:

$$\text{IEC}\ (\text{mmol g}^{-1}) = \frac{V_{NaOH} \times C_{NaOH}}{W_d} \quad (3)$$

where V_{NaOH} is the consumed volume of NaOH solution C_{NaOH} is the molarity of NaOH solution.

The VO^{2+} permeability measurements were carried out at room temperature (25 ± 2 °C) using a membrane-separated diffusion cell. The volume of each compartment was 100 mL, and the effective area of the membrane was 3.14 cm^2. The feed compartment was filled with 1 M $VOSO_4$ in 2 M H_2SO_4, and

the permeate compartment contained 1 M $MgSO_4$ in 2 M H_2SO_4. The VO^{2+} permeability of the membrane was determined by collecting 5 mL aliquots of a liquid sample using a syringe at prescribed time intervals. The samples extracted from the permeate compartment were analyzed by inductively coupled plasma atomic emission spectroscopy (ICP-AES; 735 ICP-OES, Agilent Technologies). The vanadium permeability (P) was calculated using the following equation:

$$V_{\mathrm{B}} \frac{\mathrm{d}C_{\mathrm{B}}(t)}{\mathrm{d}t} = A \frac{P}{L} (C_{\mathrm{A}} - C_{\mathrm{B}}(t)) \quad (4)$$

where V_B is the volume of the $MgSO_4$ reservoir, C_A is the VO^{2+} concentration in the $VOSO_4$ reservoir, C_B (t) is the VO^{2+} concentration in the $MgSO_4$ reservoir as a function of time, and A and L are the membrane cross-sectional area and thickness, respectively.

V-2-4. VRB single cell test

A VRB single cell was assembled by sandwiching a membrane between two pieces of carbon felt electrodes (XF-30A, Toyobo Co., Ltd.). The VO^{2+} solution was prepared by dissolving $VOSO_4 \cdot 3.5H_2O$ (99.9%, Wako Pure Chemical Industrials) in 2 M H_2SO_4 solution. The V^{3+} solution was prepared by the electrochemical reduction of the VO^{2+} solution. 2 M VO^{2+} and V^{3+} in 2

M H_2SO_4 solutions were used as the initial positive and negative electrolytes, respectively. The active area of the cell was 12 cm^2, and the volume of the electrolyte solution was 2.8 mL in each half cell. Charge–discharge cycling of the cell was carried out at room temperature (25 ± 2 °C) using a battery cycler (Maccor 4000). The cutoff voltages of the cell tests were selected to be 1.6 V and 0.8 V, which corresponds to ≈100% and ≈0% state of charge (SOC), respectively.

V-3. Results and Discussion

V-3-1. Membrane morphology

Figure V-3 shows cross-sectional FE-SEM images of ND and NDP membranes. The FE-SEM images confirmed that ND and NDP membranes had a sandwich-like structure comprising the double Nafion outer layers and a D-AMH-3 central layer. NDP membrane showed dense D-AMH-3 layer while ND membrane had a rough D-AMH-3 layer. This result indicate that the well-ordered D-AMH-3 layer was formed by hot-pressing process. It is known that the nominal thickness of the N117 membrane is around 180 μm. The dry thickness of ND and NDP membrane was around 180 μm, similar to that of N117. These values were expected to minimize the effect of the membrane thickness. The EDX mapping confirmed the presence of D-AMH-3 within the central layer, probably indicating the presence of a well-formed D-AMH-3 layer between the Nafion layers. The good dispersion of D-AMH-3 in the central layer may effectively reduce vanadium crossover.

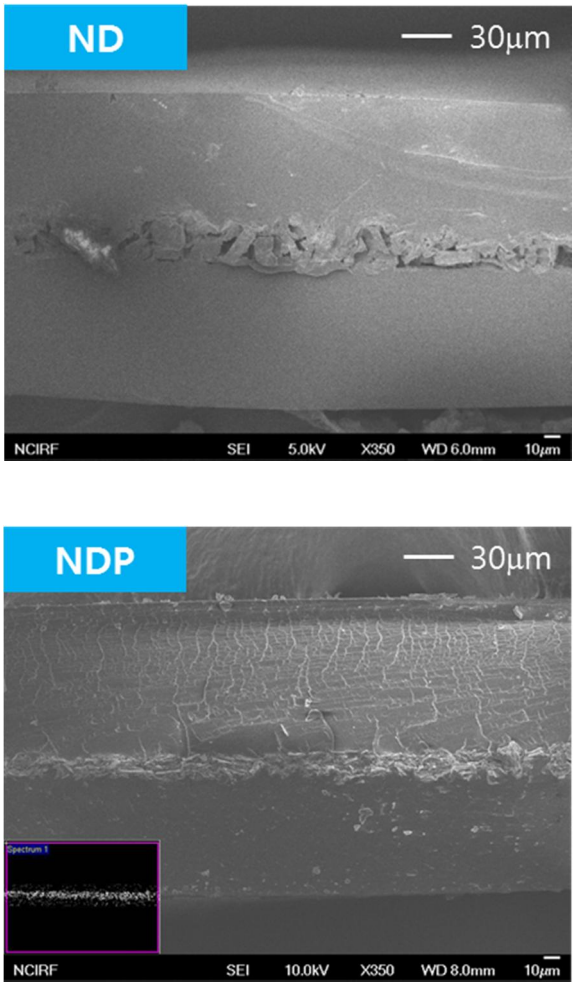

Figure V-3. FE-SEM cross-sectional images of ND and NDP membrane (inset, EDS mapping).

V-3-2. Physicochemical properties

The results of physicochemical properties such as water uptake and swelling ratio are summarized in Table V-1. The water uptake of NDP membrane was lower than that of N117. This result can be explained by the introduction of D-AMH-3 layer. The hydroxyl groups in D-AMH-3 and the sulfonic acid groups in N117 can interact to form hydrogen bonds. Hydrogen bonds reduce the site that water can be absorbed, resulting in lower water uptake of NDP membrane. Lower water uptake in NDP membrane would result in lower vanadium permeability compared with N117. The thickness swelling ratio (direction of vertical to D-AMH-3 layer) of membranes was similar, but the length swelling ratio (direction of horizontal to D-AMH-3 layer) was different, which was attributed to the D-AMH-3 layer. D-AMH-3 layer can suppress the swelling in the horizontal direction by interaction with sulfonic acid groups in N117 (Figure V-4). Since D-AMH-3 was not uniformly dispersed in the membrane, the swelling in the vertical direction was not reduced. The IEC provides an indication of the number of ion-exchangeable groups present in an ion-conducting polymer membrane. It can be seen that the IEC of NDP membrane was lower than that of N117. The intoroduction of D-AMH-3 layer into the membrane contributes to a decrease in the IEC. The reason for this is that there were no ion exchange sites, such

as SO_3^- groups, within D-AMH-3 and the exchangeable ions within D-AMH-3 were removed during acid-hydrothermal treatment.

V-3-3. Vanadium permeability

The change of VO^{2+} concentration with time for N117, ND, and NDP membrane is shown in Figure V-5. The vanadium concentration increase with time for ND and NDP membranes was lower than that for N117 membrane. It can be seen that the vanadium concentration in the compartment of the diffusion cell has a nearly linear relationship with time. The vanadium permeability of all membranes were 3.07×10^{-6} cm^2 min^{-1} for N117, 2.12×10^{-6} cm^2 min^{-1} for ND, and 8.64×10^{-7} cm^2 min^{-1} for NDP, calculated according to the equation (4). These results showed that a reduction in vanadium permeability can be achieved by D-AMH-3 layer, which acts as a permselective barrier by tortuous pathway effect. Since the pore size of D-AMH-3 is smaller than active vanadium ions (multi-hydrated state), the vanadium ions may be blocked or bypassed by the D-AMH-3 particles (Figure V-6). NDP membrane showed lower vanadium permeability than ND, which was attributed to the well-formed D-AMH-3 layer within NDP membrane. The lower vanadium permeability indicated that the coulombic efficiency of the VRB prepared with a ND membrane would be higher than that obtained using an N117 membrane.

Table V-1. Physicochemical properties of N117 and NDP membranes.

Sample	IEC (meq/g)	Water uptake (%)	Swelling ratio (%)	
			Thickness	Length
N117	0.91	18.21	8.29	11.54
NDP	0.84	14.29	10.63	3.73

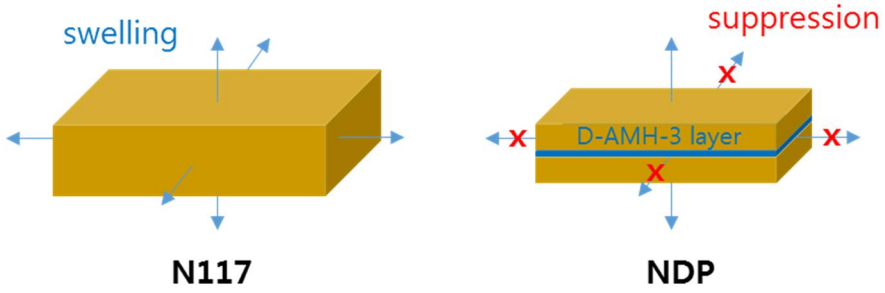

Figure V-4. Schematic of suppression of NDP membrane swelling by D-AMH-3 layer.

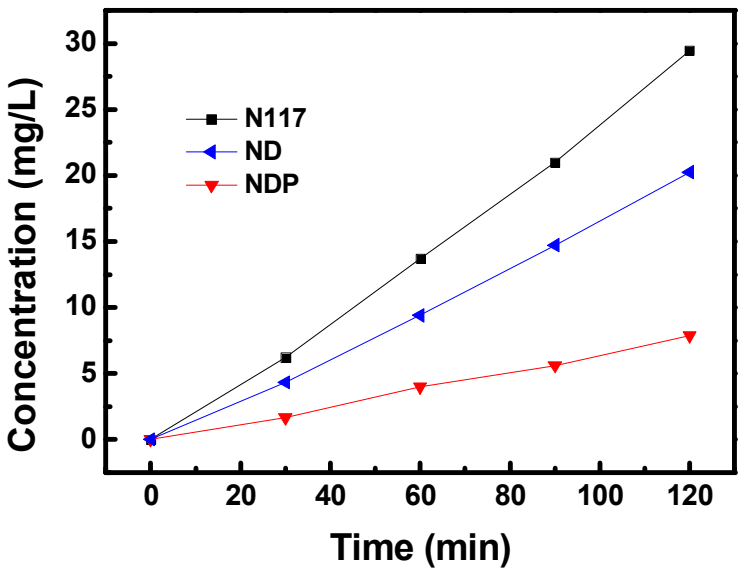

Figure V-5. Change in VO^{2+} concentration over time in the $MgSO_4$ compartment across N117, ND, and NDP membranes.

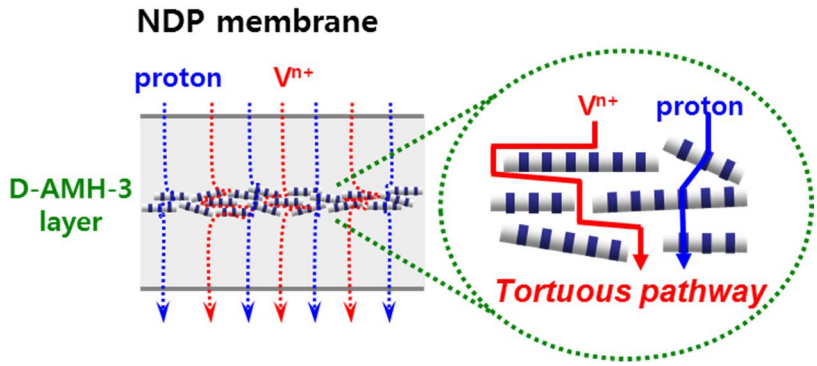

Figure V-6. Role of the D-AMH-3 layer in the vanadium crossover through NDP membranes.

V-3-4. VRB single cell performance

Figure V-7 shows the representative charge–discharge curves obtained from VRBs prepared with N117 and NDP membranes at 40 mA cm^{-2}. In general, the charge–discharge capacities are controlled by proton conductivity, vanadium permeability, cycle number, and etc. As shown, the charge and discharge capacities of the VRB with NDP were higher than those obtained from the VRB with N117, demonstrating that the NDP membrane improved the cell performance by reducing vanadium crossover.

The charge–discharge curves of VRBs assembled with N117 and NDP membranes at a current density of 20, 40, 60, 80, and 100 mA cm^{-2} are illustrated in Figure V-8 and 9. With increasing current density, the charge–discharge capacities of the VRBs with N117 and NDP decreased owing to the internal resistance (IR) drop. The VRB cell resistances calculated from IR drop values were 0.10 Ω for VRB with N117 and 0.15 Ω for VRB with NDP. Because D-AMH-3 contains very few proton-hopping sites, such as sulfuric acid groups, the cell resistance of the VRB-NDP increased. The larger IR drop of VRB with NDP led to a higher charge voltage and a lower discharge voltage than VRB with N117 at all current densities.

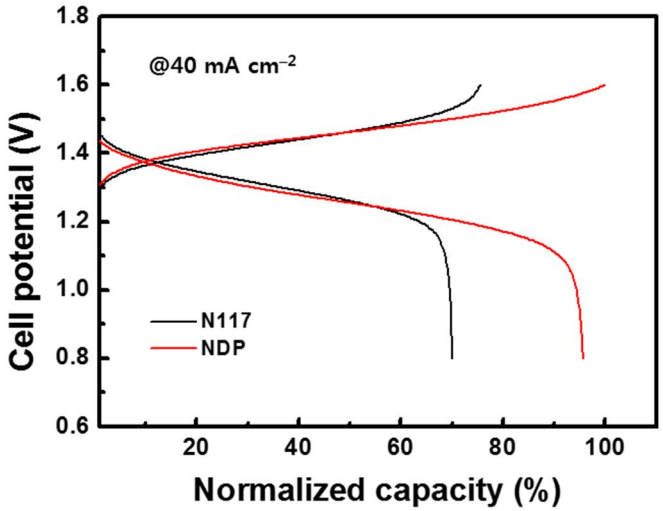

Figure V-7. Representative charge–discharge curves for VRB with N117 and NDP membranes at 40 mA cm^{-2}.

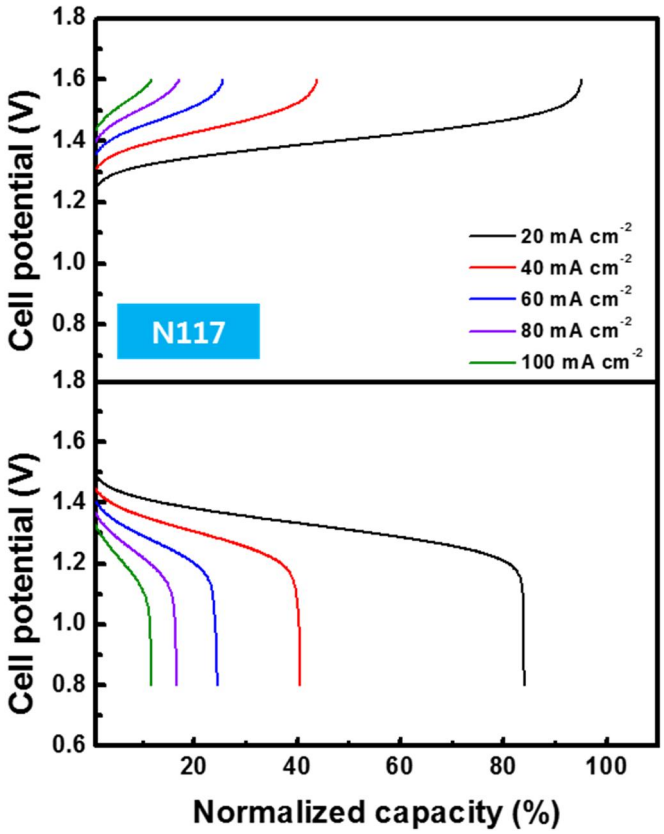

Figure V-8. Charge–discharge curves for VRB with N117 membrane at 20–100 mA cm^{-2}.

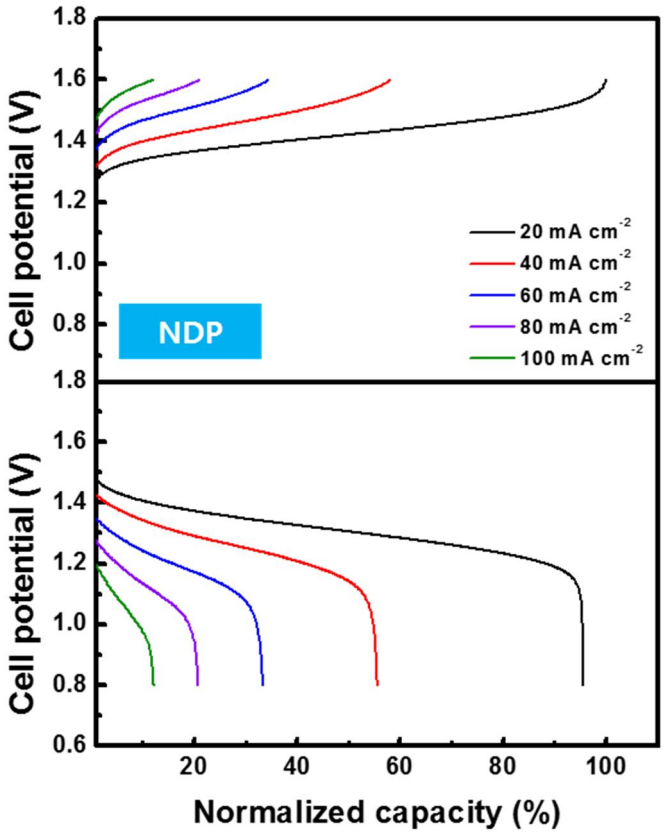

Figure V-9. Charge–discharge curves for VRB with NDP membrane at 20–100 mA cm^{-2}.

In the charge–discharge test, the coulombic efficiency (CE), voltage efficiency (VE), and energy efficiency (EE) of the VRBs at current densities from 20 to 100 mA cm^{-2} are shown in Figure V-10. The CE, VE, and EE of VRBs were calculated by following equations:

$$\mathrm{CE}\ (\%) = \frac{\int_0^t I_d dt}{\int_0^t I_c dt} \times 100\%$$

$$\mathrm{EE}\ (\%) = \frac{\int_0^t V_d I_d dt}{\int_0^t V_c I_c dt} \times 100\%$$

$$\mathrm{VE}\ (\%) = \frac{EE}{CE} \times 100\%$$

The CE values of VRBs to increase with increasing current density. As the current density increased, the charge–discharge time became shorter, which led to lower cross-mixing of the vanadium species, resulting in a higher CE. The CE values of the VRB with NDP were higher than that of the VRB with N117 at all current densities, in good agreement with the results obtained from the VO^{2+} permeability measurements. Because the VRB with NDP had a higher cell resistance than the VRB with N117, the VE values of the VRB with NDP were lower than that of the VRB with N117 at all current densities. The EE of the VRB with NDP was lower than that of the VRB with N117 at current density of 40–100 mA cm^{-2} because the cell resistance was higher. However, at a current density of 20 mA cm^{-2}, the EE of the VRB with NDP

exceeded that of the VRB with N117: 87.6% (NDP) and 82.8% (N117), due to the low vanadium species crossover and minimization of the IR drop.

The cycling performance of the VRBs prepared with either of the two membranes was investigated at 40 mA cm^{-2} over 100 charge–discharge cycles. The charge–discharge curves for the VRB with N117 and VRB with NDP over 100 cycles are shown in Figure V-11. The charge–discharge voltage of the VRB with NDP remained constant and the capacity loss of the VRB with NDP was small compared to that obtained from VRB with N117 over 100 cycles, indicating a low and stable vanadium permeation rate through the NDP membrane. As shown in Figure V-12, there is no efficiency decline after 100 charge–discharge cycles. This result indicate that the VRB-NDP showed a stable performance in vanadium solutions under strongly acidic conditions. The D-AMH-3 layer in the NDP membrane did not deform in acidic vanadium solutions because D-AMH-3 had been pre-treated with a strong acid. Figure V-13 shows the capacity loss curves of the VRB with N117 and VRB with NDP. The average capacity loss per cycle for the VRB with N117 was 0.86%, whereas the corresponding value for the VRB with NDP was 0.15%. The capacity retention of the VRB with NDP was 84.6% after 100 cycles, much higher than the value obtained from the VRB with N117 (14.3%). The low capacity retention of the VRB with N117 was attributed to high vanadium species crossover. These results indicated that the

VRB with NDP could operate longer than the VRB with N117 because the D-AMH-3 layer acted as a permselective layer to reduce vanadium species crossover.

The VRB cycling tests confirmed that the NDP membrane offered a good chemical stability in strongly acidic vanadium solutions and a long lifetime suitable for VRB systems. In addition, the sandwich structure of the NDP membrane is expected to increase the VRB operating lifetime because when one Nafion layer facing the catholyte breaks, the other Nafion layer can continue to operate. Pentavalent vanadium ions (VO_2^+) in a fully charged catholyte have highly oxidizing nature [131, 150], causing the catholyte-facing membrane to degrade during repeated cycling.

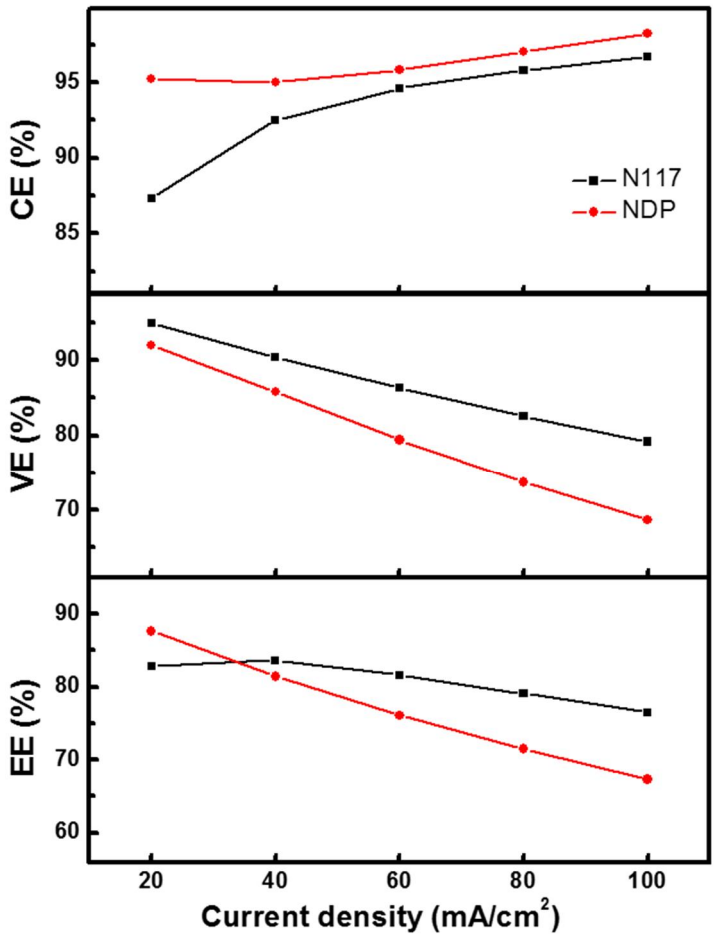

Figure V-10. Cell efficiencies of VRBs with N117 and NDP membranes at 20–100 mA cm^{-2} in the charge–discharge test.

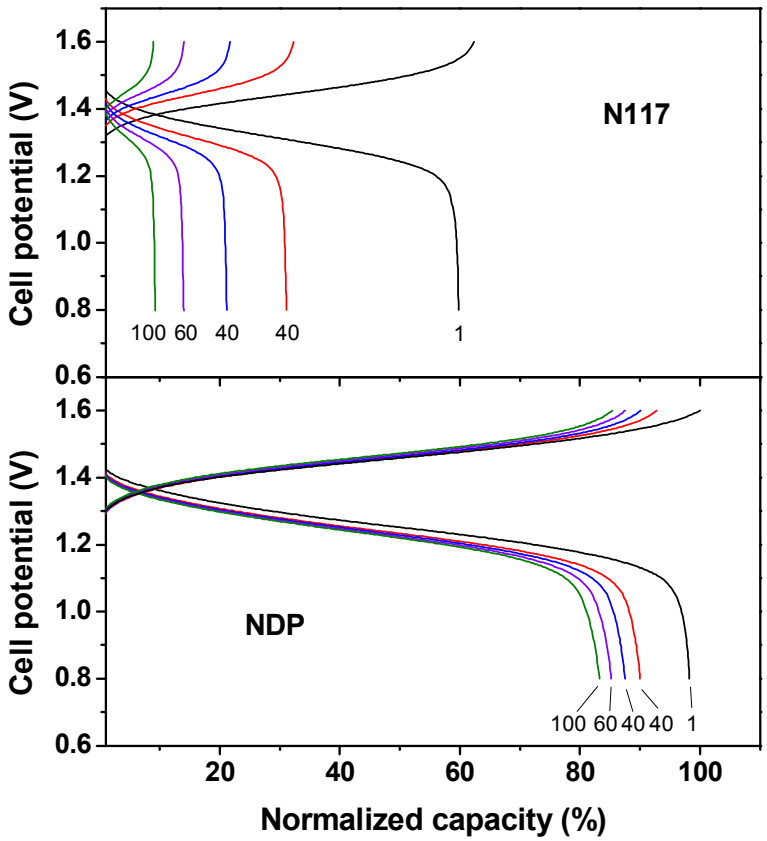

Figure V-11. Charge–discharge curves for VRBs with N117 and NDP membranes at 40 mA cm^{-2} over 100 cycles.

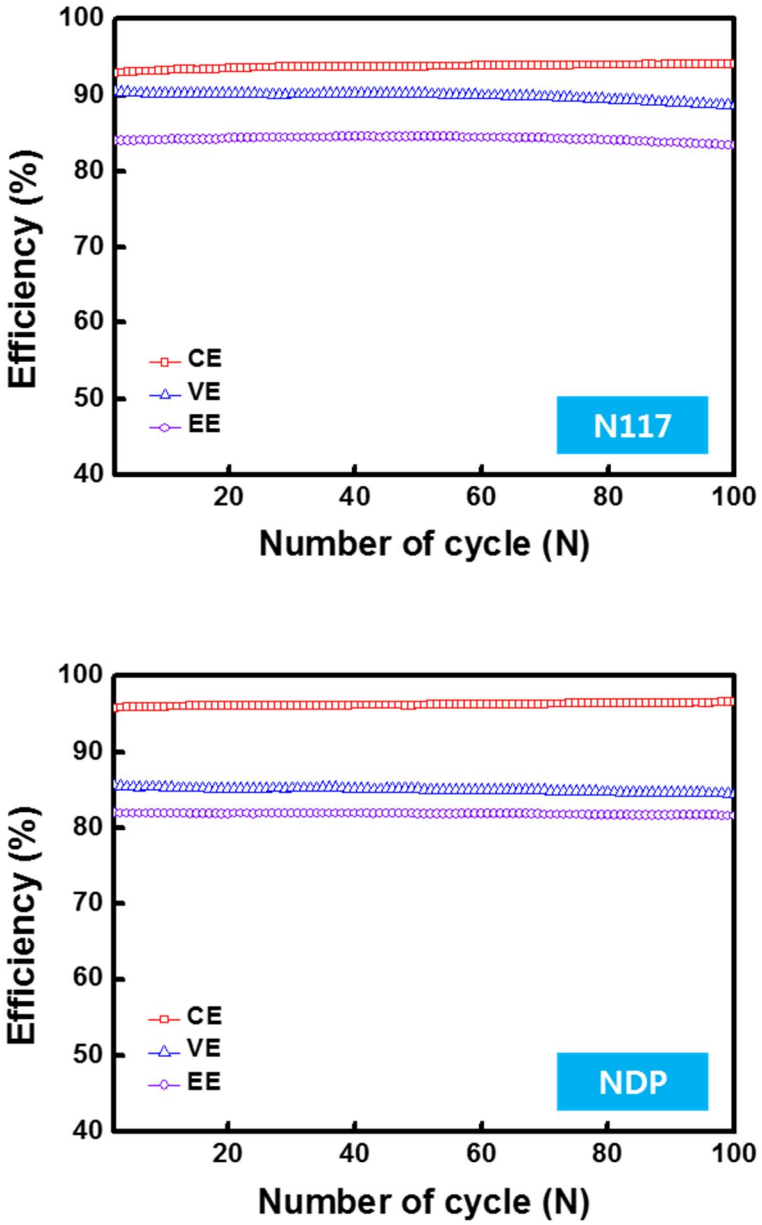

Figure V-12. Efficiency of VRBs with N117 and NDP membranes at 40 mA cm^{-2} in the cycle life test.

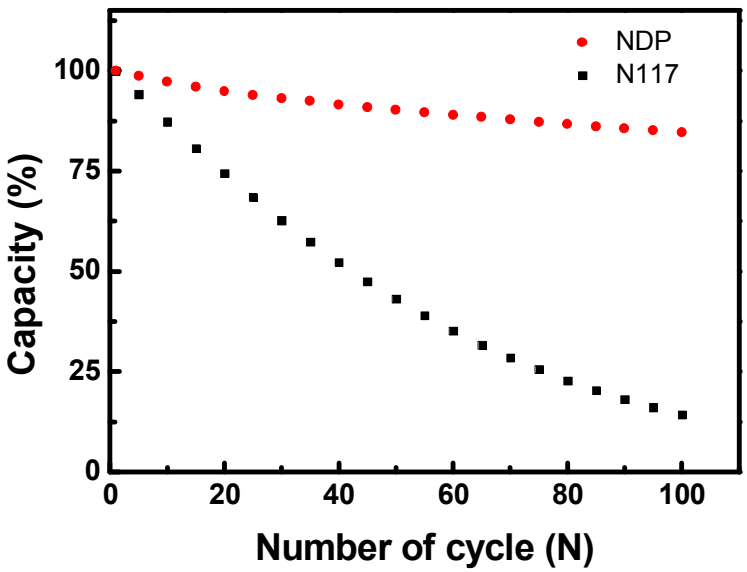

Figure V-13. Capacitiy retention of VRBs with N117 and NDP membranes at 40 mA cm^{-2} in the cycle life test.

V-4. Conclusion

A Nafion-based composite membrane with a D-AMH-3 layer was prepared by solution casting and hot pressing. FE-SEM analysis confirmed that NDP membrane had sandwich-type structure and was about 180 μm thick. The D-AMH-3 layer reduced the membrane swelling and acted as a permselective layer to reduce vanadium crossover. Although the NDP membrane delivered a slightly lower energy efficiency compared with the N117 membrane at a higher current density due to a higher cell resistance, the NDP membrane showed a lower vanadium permeability compared to the N117 membrane, thereby improving the coulombic efficiency and capacity retention in VRB single cell tests. The NDP membrane exhibited a stable performance over 100 cycles. Cell resistance may potentially be reduced by further optimizing the D-AMH-3 layer content and by modifying the D-AMH-3 surface.

CHAPTER VI

SULFONATED POLY(ETHER ETHER KETONE) COMPOSITE MEMBRANES WITH MICROPOROUS LAYERED SILICATE AMH-3 FOR IMPROVED PERFORMANCE IN VANADIUM REDOX FLOW BATTERIES

VI-1. Introduction

As mentioned chpater V, Ion exchange membranes (IEMs) are key components of VRBs, separating the positive and negative electrolytes to prevent cross-mixing and allow ion transport to complete the current circuit [151]. IEM properties strongly affect VRB performance, with ideal properties including high proton conductivity, low vanadium ion permeability, good chemical stability, and low cost [152]. Conventional IEMs used in VRBs are made from perfluorosulfonic polymers such as Nafion, which has excellent proton conductivity and chemical stability under acidic aqueous solutions [153]. However, perfluorosulfonic polymers have drawbacks of high vanadium crossover, which decreases cell efficiency in VRB systems, and

high cost, which limits large-scale applications [154].

Recently, alternative aromatic polymers, such as sulfonated poly(ether ether ketone), sulfonated poly(tetramethyldiphenyl ether ether ketone), sulfonated poly(arylene ether), sulfonated poly(fluorenyl ether ketone), sulfonated poly(phthalazinone ether ketone), and sulfonated poly(sulfone), have been investigated to suppress vanadium crossover and reduce IEM costs in VRB systems [155–174]. Among these sulfonated aromatic polymers, sulfonated poly(ether ether ketone) (SPEEK) has been widely investigated due to its high ion selectivity, low cost, and good chemical stability. Although a high degree of sulfonation (DS) is necessary for good proton conductivity, SPEEK membranes with a high DS (>75%) exhibited high swelling, poor mechanical stability, and excessive vanadium crossover. Furthermore, SPEEK membranes with a low DS (<55%) have satisfactory mechanical stability, but insufficient conductivity for good VRB performance [175].

Incorporating an organic–inorganic filler is a facile method for improving mechanical stability and reducing vanadium crossover [155–160, 165–170]. If the incorporated filler is impermeable to vanadium ions, protons will have a more direct and shorter path compared with vanadium ions. This composite membrane can enhance ion selectivity by reducing vanadium crossover. However, it is necessary to optimize the amount of filler because the properties of membranes, such as proton conductivity and water uptake can be reduced by incorporation of filler. Among composite membranes with

organic–inorganic fillers, those incorporating microporous materials, such as zeolites, can effectively reduce vanadium crossover while maintaining proton conductivity because of their well-defined structure and hydrophilic nature [176]. Zeolites have been widely used as fillers for polyelectrolytes in direct methanol fuel cells (DMFCs) [177–180]. As protons can pass through the micropores, composite membranes containing zeolites have been shown to possess low methanol crossover and relatively high proton conductivity. However, there have been few reports of composite membranes containing zeolites applied to VRBs because zeolites can be dealuminated under acidic conditions, leading to the destruction of their framework [91]. Therefore, most zeolites used for DMFC applications would be unstable in the acidic aqueous solution used in VRB systems.

AMH-3 is a microporous material that has been used as a filler in gas separators [57, 69, 145], and a polyelectrolyte in DMFCs [70, 181] and VRBs [182], owing to its unique three-dimensional microporous framework, hydrophilic nature (caused by hydroxyl groups), and good chemical stability (due to the lack of Si–O connections with any metal species, such as aluminum or titanium). In previous studies [70, 181], introducing AMH-3 into Nafion was shown to reduce methanol and vanadium crossover by forming an AMH-3 layer. However, larger-sized AMH-3 particles (approx. 20 μm) reduced the proton conductivity. Furthermore, dispersing AMH-3 within the

membrane matrix was difficult because AMH-3 sank during composite membrane preparation due to its large particle size. Grinding methods, such as ball-milling and ultrasonication, have been utilized to reduce the sizes of zeolites [180] and ETS-4 [183]. Ground particles used as a polyelectrolyte filler in DMFCs were well dispersed within the membrane matrix and reduced methanol crossover without significantly decreasing proton conductivity, meaning that microporous materials function normally after grinding.

In this study, ultrasonication was used to reduce the size of AMH-3 particles. SPEEK-based composite membranes containing ground AMH-3 (U-AMH-3) were prepared using a solution casting method. The effect of U-AMH-3 incorporation on the physicochemical and mechanical properties, and vanadium permeability, of the composite membranes, and their single cell performance, was studied. Results obtained for composite membranes were compared with those of pristine SPEEK and Nafion membranes

VI-2. Experimental Section

VI-2-1. Materials

Poly(ether ether ketone) (PEEK) (450P, Victrex), sulfuric acid (H_2SO_4, 95–98%, Sigma-Aldrich), N,N-Dimethylformamide (DMF, 98%, Sigma-Aldrich), strontium chloride hexahydrate ($SrCl_2 \cdot 6H_2O$, 99%, Junsei), titanium trichloride ($TiCl_3$, 20%, Kanto), sodium silicate solution (26.5% SiO_2, Sigma-Aldrich), sodium hydroxide (NaOH, 98%, Sigma-Aldrich), hydrochloric acid (HCl, 37%, Sigma-Aldrich) were used as received, without further purification. Nafion 117 membrane (N117) was purchased from Dupont company. Highly deionized water (18 MΩ cm^{-1}) was used in all experiments.

VI-2-2. Preparation of U-AMH-3

AMH-3 was synthesized and delaminated according to methods described in chapter IV. AMH-3 was synthesized by using the hydrothermal reaction (200 °C, 24 h) of a mixture with following molar composition: 1 TiO_2: 10 SiO_2: 14 NaOH: 2 $SrCl_2$: 675 H_2O. The delaminated AMH-3 (D-AMH-3) was prepared by the acid-hydrothermal treatment with 1 M HCl solution at 200 °C for 24 h. To prevent AMH-3 sinking within the polymer matrix due to its large size, D-AMH-3 was dispersed in deionized water and ground by

ultrasonication to reduce particle size. The ultrasonication treated D-AMH-3 was termed as U-AMH-3.

VI-2-3. Membrane preparation

Sulfonated poly(ether ether ketone) (SPEEK) was prepared by the sulfonation of PEEK in a flask under a nitrogen atmosphere. Prior to sulfonation, PEEK powder was dried in an oven at 100 °C. PEEK was dissolved into H_2SO_4 with vigorous mechanical stirring at room temperature (25 ± 2 °C) for 120 h. After the reaction, the mixture was poured into ice water with mechanical agitation to terminate the sulfonation reaction. The precipitated polymer was washed with deionized water several times until the pH value was 6–7 and then dried at 80 °C in a vacuum oven for 12 h. The degree of sulfonation in SPEEK was 0.74, as determined by ^{1}H-NMR spectroscopy according to a literature method [184].

The SPEEK/U-AMH-3 composite membranes were prepared by using a solution casting method. Typical experimental details were as follows: SPEEK (1 g) was dissolved in *N*,*N*-dimethylformamide (DMF, 10 mL) with shaking (150 rpm) to form the polymer solution. The desired amount of U-AMH-3 was added to the SPEEK solution, which was then stirred and degassed by ultrasonication. The resultant mixture was slowly poured into a

glass dish, heated at 60 °C for 4 h, and then evaporated at 60 °C in a vacuum oven for 24 h. After drying, the glass dish was cooled in water, and the membranes were obtained by peeling from the dish. The composite membranes were pretreated by soaking in 1 M H_2SO_4 for 24 h and then deionized water for 24 h to remove excess acid. The thus-pretreated composite membranes were stored in deionized water before testing. N117 was pretreated according to literature [177]. In this chapter, SU*x* denotes a SPEEK/U-AMH-3 composite membrane containing *x* wt% of U-AMH-3.

VI-2-4. Characterization

VI-2-4-1. Particle characterization

The morphology of particles was observed by a field-emission scanning electron microscope (JEOL, JSM-6700F) equipped with an energy-dispersive spectroscope. High-resolution transmission electron microscopy (HR-TEM) images of U-AMH-3 were obtained using a JEM-ARM200F instruments operated at 200 kV. The size of U-AMH-3 in DMF was analyzed by dynamic light scattering (DLS) using a photon correlation spectroscopy system (DLS-7000, Otsuka Electric) containing an Ar laser.

VI-2-4-2. Membrane characterization

The morphology of cross-section morphology of membranes was observed by a field-emission scanning electron microscope (JEOL, JSM-6700F) equipped with an energy-dispersive spectroscope. The cross-section samples were obtained by breaking membranes in liquid nitrogen.

Water uptake was defined as the ratio of water weight in wet membrane to dry membrane weight, while swelling ratio was the ratio of length increment in wet membrane to dry membrane length. The membranes was soaked in deionized water for 24 h at room temperature (25 ± 2 °C). And then they were taken out and measured immediately after removing the surface water with tissue paper to obtain the wet weight of the membranes. Then the membranes were dried under vacuum oven at 80 °C for 24 h. The water uptake and swelling ratio of the membranes were calculated by following equations:

$$\text{Water uptake}\ (\%) = \frac{W_w - W_d}{W_d} \times 100\% \quad (1)$$

$$\text{Swelling ratio}\ (\%) = \frac{L_w - L_d}{L_d} \times 100\% \quad (2)$$

The ion exchange capacity (IEC) of the membranes was determined by conventional titration method. Employing 50 mL saturated NaCl solution as the ion exchange agent, the amount of H^+ exchanged from the membranes was

determined by titrating with 0.1 M NaOH solution, using phenolphthalein as indicator. The IEC of membranes was calculated by following equation:

$$\text{IEC (mmol g}^{-1}) = \frac{V_{NaOH} \times C_{NaOH}}{W_d} \quad (3)$$

where V_{NaOH} is the consumed volume of NaOH solution C_{NaOH} is the molarity of NaOH solution.

The proton conductivity of the membranes was measured in the four-point probe conductivity cells by impedance spectroscopy using a Solartron 1225 electrochemical impedance analyzer. The impedance was measured in the frequency range 1–10^5 Hz with an AC current amplitude of 1 mA. The proton conductivity measurements were carried out on fully hydrated membranes with the cell. The proton conductivity σ was calculated by following equation:

$$\sigma \text{ (mS cm}^{-1}) = \frac{L}{AR} \quad (4)$$

where L is the thickness of the hydrated membrane, A is the membrane cross-sectional area, and R is bulk resistance calculated from the impedance plot with a ZPLOT software.

The mechanical properties of membranes were measured by a universal testing machine (UTM; 5543, Instron, USA) at a speed of 2 mm min^{-1}. The

membranes were cut into a dumbbell shape with a width of 3.5 mm. The data show the average of four independent measurements of each parameter.

VO^{2+} permeability measurements were carried out at room temperature (25 ± 2 °C) using a membrane-separated diffusion cell. The volume of each compartment was 100 mL and the effective area of the membrane was 3.14 cm^2. The feed compartment was filled with 1 M $VOSO_4$ in 2 M H_2SO_4, and the permeate compartment contained 1 M $MgSO_4$ in 2 M H_2SO_4. The VO^{2+} permeability of the membrane was determined by collecting 5 mL aliquots of liquid sample using a syringe at prescribed time intervals. Samples extracted from the permeate compartment were analyzed by inductively coupled plasma atomic emission spectroscopy (ICP-AES; ICPS-7510, Shimadzu). The vanadium permeability (P) was calculated using the following equation:

$$V_B \frac{dC_B(t)}{dt} = \mathrm{A}\frac{P}{L}(C_A - C_B(t)) \quad (5)$$

where V_B is the volume $MgSO_4$ reservoir volume, C_A is the VO^{2+} concentration in the $VOSO_4$ reservoir, C_B(t) is the VO^{2+} concentration in the $MgSO_4$ reservoir as a function of time, and A and L are the membrane area and thickness, respectively.

VI-2-5. VRB single cell test

A VRB single cell was assembled by sandwiching a membrane between two pieces of carbon felt electrodes (XF-30A, Toyobo Co., Ltd.). The VO^{2+} solution was prepared by dissolving $VOSO_4 \cdot 3.5H_2O$ (99.9%, Wako Pure Chemical Industrials) in 2 M H_2SO_4 solution. The V^{3+} solution was prepared by the electrochemical reduction of the VO^{2+} solution. 2 M VO^{2+} and V^{3+} in 2 M H_2SO_4 solutions were used as the initial positive and negative electrolytes, respectively. The active area of the cell was 12 cm^2, and the volume of the electrolyte solution was 2.8 mL in each half cell. Charge–discharge cycling of the cell was carried out at room temperature (25 ± 2 °C) using a battery cycler (Maccor 4000). The cutoff voltages of the cell tests were selected to be 1.6 V and 0.8 V, which corresponds to ≈100% and ≈0% state of charge (SOC), respectively.

VI-3. Results and Discussion

VI-3-1. Characterization of U-AMH-3

Figure VI-1 shows the mophology of AMH-3, D-AMH-3, and U-AMH-3, obsevered using a FE-SEM. It was confirmed that D-AMH-3 was exfoliated and ground by ultrasonication and that the ground D-AMH-3 flakes (U-AMH-3) and D-AMH-3 then become mixed. The size of U-AMH-3 is sub-micro meter but the morphology is irregular. HR-TEM images of U-AMH-3 are shown in Figure VI-2, revealing that the individual particels is over 200 nm and irregular rectangular shape. As shown in Figure VI-2 (b), U-AMH-3 has well-crystallized structure, which indicates that that the framework of U-AMH-3 was preserved during the ultrasonication procedure.

DLS measurements were carried out to determine the particle size distribution of U-AMH-3 in DMF. The result of number distribution is shown in Figure VI-3. Two peaks of the U-AMH-3 particle size distribution were observed, the peak located below 1 μm was corresponded to U-AMH-3 and the peak over 10 μm was corresponded to D-AMH-3 that was not exfoliated and ground by ultrasonication. The mean particle size for U-AMH-3 is 289 nm in diameter with a size distribution standard deviation of 47 nm.

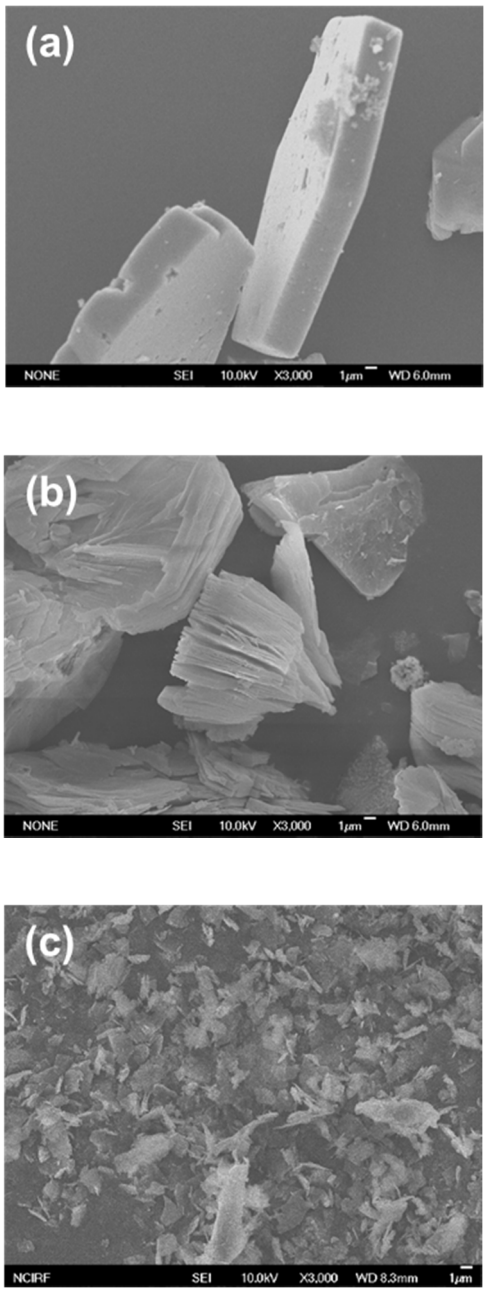

Figure VI-1. FE-SEM images of (a) AMH-3, (b) D-AMH-3, and (c) U-AMH-3

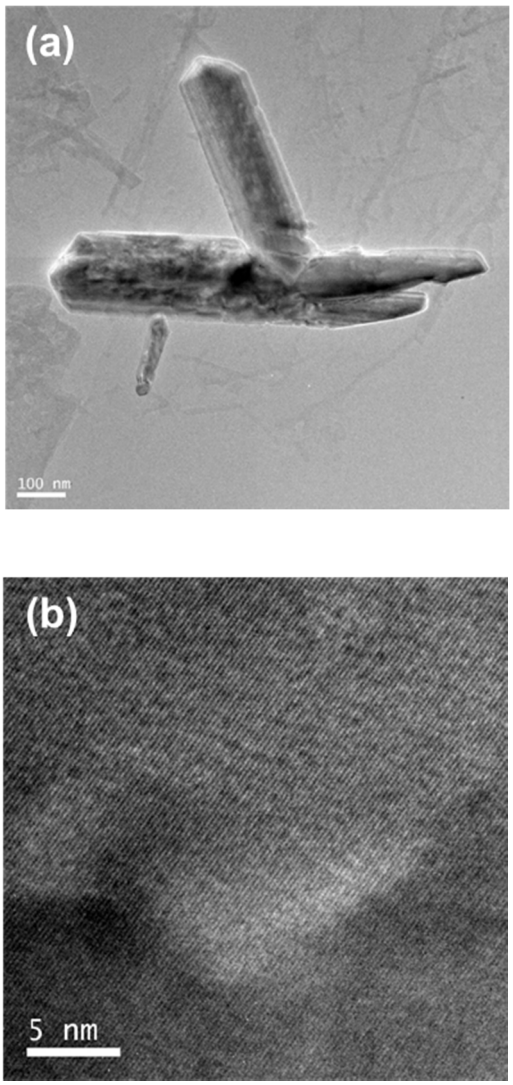

Figure VI-2. HR-TEM images of (a) U-AMH-3 and (b) higher magnification image.

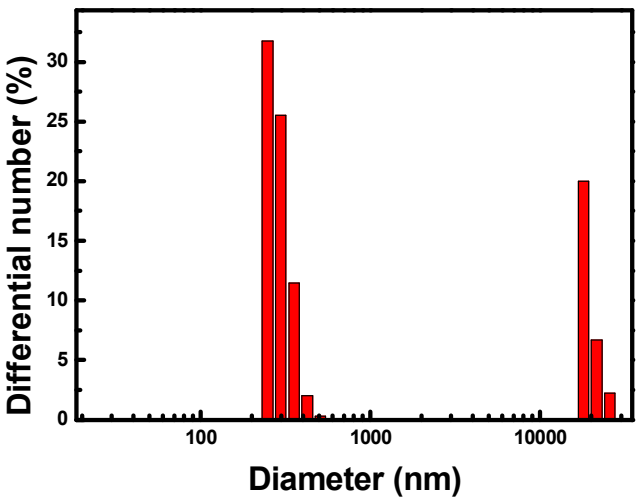

Figure VI-3. Particle size distribution of U-AMH-3.

VI-3-2. Membrane morphology

To confirm the presence and distribution of U-AMH-3 in SU composite membranes, FE-SEM observation with energy-dispersive X-ray (EDX) analysis on the cross-section of the SU composite membranes was carried out. The cross-sectional morphology and EDX results of the composite membranes are shown in Figure VI-4. FE-SEM images confirm that the SU membranes are dense and defect-free, suggesting good membrane formation. The thickness of SU membranes was about 130 μm, which was thinner than that of N117 (190 μm). EDX silicon mapping images show that the silicon was almost uniformly distributed, whicn indicates that U-AMH-3 was well-dispersed in the SPEEK matrix. The silicon distribution gradually increased with the increasing of U-AMH-3 content in the SU membranes.

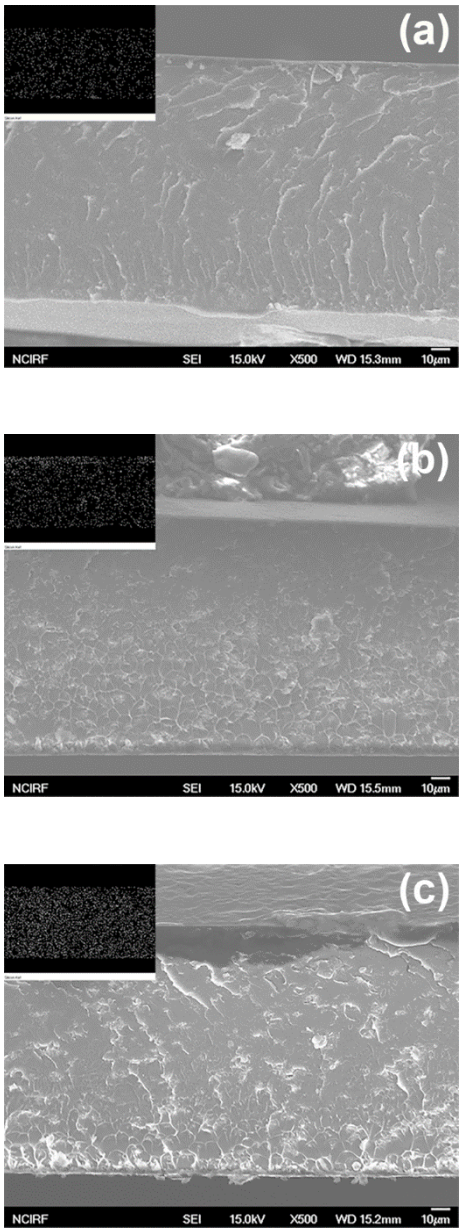

Figure VI-4. FE-SEM cross-sectional images of (a) SU1, (b) SU3, and (c) SU5 membrane (inset, EDS mapping).

VI-3-3. Physicochemical properties

The results of water uptake and swelling ratio as functions of the U-AMH-3 loading are shown in Figure VI-5. The water uptake and swelling ratio are closely related to proton conductivity and membrane stability, respectively. The water uptake of SU membranes decreased with increasing U-AMH-3 content owing to the interaction between U-AMH-3 and SPEEK. Hydrogen bonds can form between the hydroxyl groups (–OH) in U-AMH-3 and sulfonic acid groups ($–SO_3H$) in SPEEK. The incorporation of hydrophilic particles into polymer matrices leads to reduced formation of hydrophilic domains by interactions between particles and the polymer, resulting in the suppression of water absorption within composite membranes [160]. Lower water uptake in the SU membranes would result in lower vanadium permeability compared with SPEEK.

The swelling ratio of the SU membranes decreased gradually with increase in U-AMH-3 content. Similar to the water uptake results, this was attributed to the hydrogen bonds formed between U-AMH-3 and SPEEK, which suppressed the swelling of SPEEK. The lower swelling ratio of SU membranes compared with SPEEK would result in better mechanical properties and, consequently, more stable VRB performance and a lower capacity decay rate.

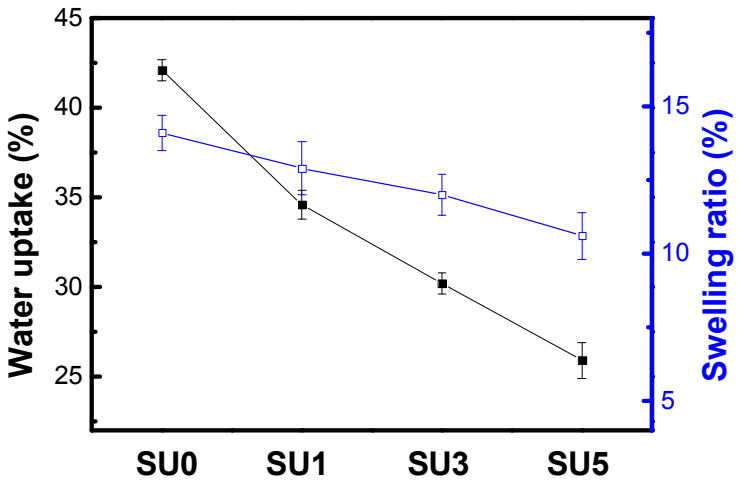

Figure VI-5. Water uptake and swelling ratio of the composite membranes as a function of the U-AMH-3 content.

The IEC (mmol g^{-1}) of each membrane was determined by using the acid–base titration method and found to be 0.91 for N117, 1.82 for SPEEK, 1.74 for SU1, 1.65 for SU3, and 1.53 for SU5. The IEC of SU membranes decreased with increasing U-AMH-3 content owing to the lower number of free SO_3H groups resulting from hydrogen bond formation with OH groups in U-AMH-3. Furthermore, there were no ion exchange sites, such as SO_3^- groups, within U-AMH-3, which caused the IEC of the SU membranes to decrease.

The mechanical properties of membranes are related to the lifetime of VRB cells because the membranes must endure not only chemical degradation, but also mechanical stress during charge–discharge cycles. Figure VI-6 shows the results of mechanical properties of all membranes. It can be seen that the SU membranes had higher tensile strength and elastic modulus than the N117 membrane, indicating that U-AMH-3 incorporation into the SPEEK matrix improved the mechanical properties. When U-AMH-3 content in the composite membranes was increased, the tensile strength and elastic modulus of the SU membranes also increased, which was attributed to interactions between SPEEK $–SO_3H$ groups and U-AMH-3 –OH groups. This result was in good agreement with the swelling behavior. A summary of the physicochemical properties of all membranes is given in Table VI-1.

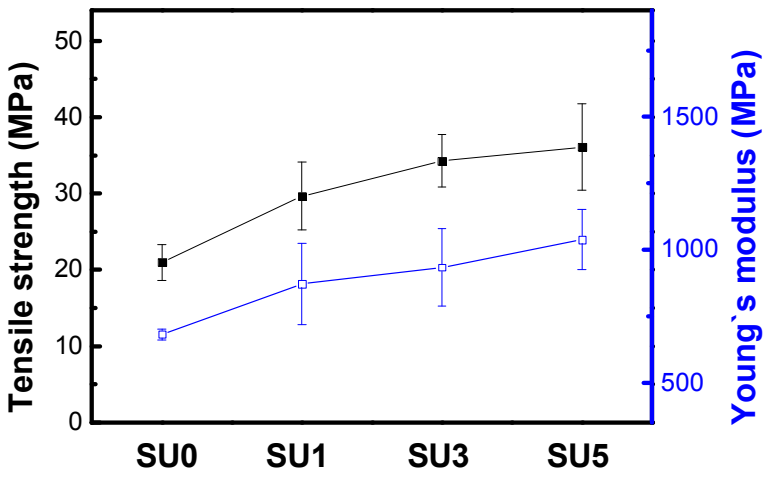

Figure VI-6. Mechanical properties of the composite membranes as a function of the U-AMH-3 content.

Table VI-1. Physicochemical property and mechanical properties of all membranes.

Sample	Water uptake (%)	Swelling ratio (%)	IEC (mmol g^{-1})	Tensile strength (MPa)	Elastic modulus (MPa)
N117	28.5	17.2	0.91	19.1	331.6
SPEEK	42.1	14.1	1.82	21.0	681.4
SG1	34.6	12.9	1.74	29.7	871.9
SG3	30.2	12.0	1.65	34.3	933.8
SG5	25.9	10.6	1.53	36.1	1037.4

VI-3-4. Proton conductivity and vanadium permeability

In general, the proton conductivity of the membrane was mainly affected by water uptake and IEC. Therefore, the proton conductivities of the SU membranes were expected to be lower than that of SPEEK. As shown in Figure VI-7, the SU1 membrane showed similar proton conductivity to that of SPEEK, and the proton conductivities of other composite membranes decreased as the U-AMH-3 content increased. It has been reported that water molecules can transport through an AMH-3 framework [66], allowing protons to also transport by a vehicle mechanism in the form of H_3O^+. With low U-AMH-3 contents, it was speculated that U-AMH-3 incorporation affected water channels interconnectivity within SPEEK through a 3D microporous U-AMH-3 framework (Figure VI-8). The hydrophilicity of U-AMH-3 also facilitated water channel interconnectivity. However, the rate of water transport through the U-AMH-3 framework was not fast, leading to longer pathways for protons at high U-AMH-3 contents, which resulted in a decrease in proton conductivity as the U-AMH-3 content increased.

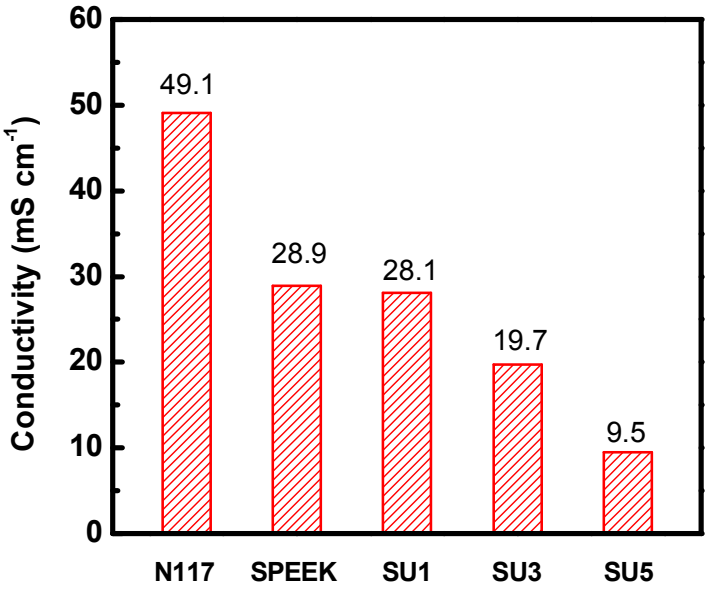

Figure VI-7. Proton conductivity of the all membranes.

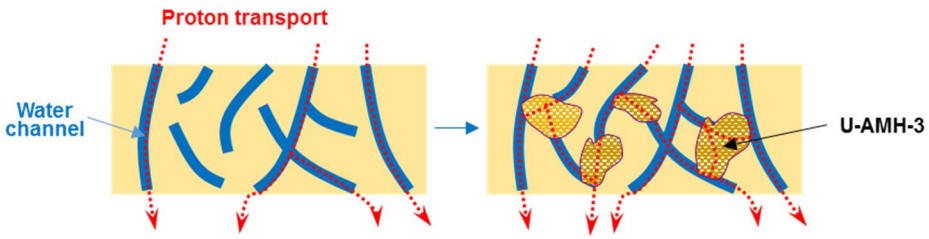

Figure VI-8. Schematic diagram representing the water channels in SPEEK (left) and in SU composite membrane (right).

The vanadium concentration in the compartment of the diffusion cell is shown in Figure VI-9 as a function of time for all membranes. A linear relationship between vanadium concentration and time was observed for all membranes. The vanadium permeability (P) was calculated for each sample according to equation (5) giving P values for N117, SPEEK, SU1, SU3, and SU5 of 30.7×10^{-7}, 18.0×10^{-7}, 12.6×10^{-7}, 9.6×10^{-7}, and 6.1×10^{-7} cm^2 min^{-1}, respectively. The vanadium permeability of SPEEK was lower than that of N117 due to its microstructure, which gave less hydrophobic/hydrophilic separation and more narrow/branched water-filled channels compared with those of N117 [156–160]. Higher U-AMH-3 contents clearly led to lower vanadium permeability in the SU membranes. This result showed that higher U-AMH-3 content resulted in more tortuous pathways for the movement of vanadium species within the membrane, which decreased the vanadium permeability of the SU membranes (Figure VI-10).

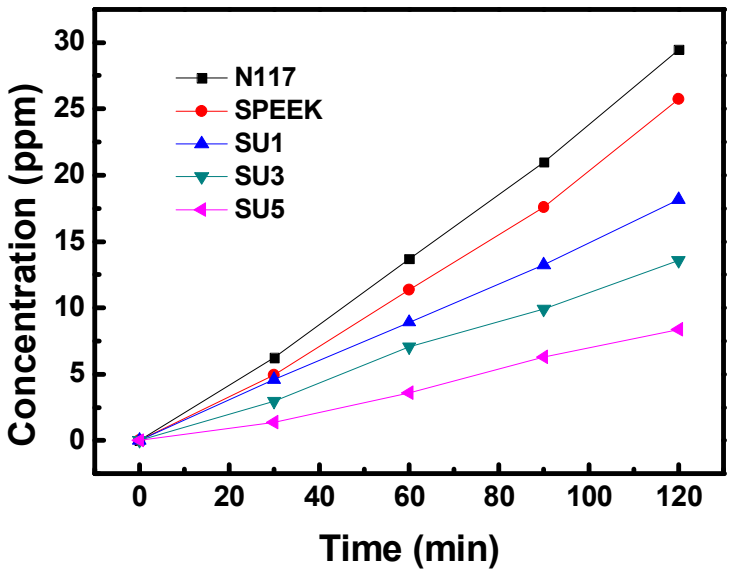

Figure VI-9. Change in VO^{2+} concentration over time in the $MgSO_4$ compartment across N117, SPEEK, and SU membranes.

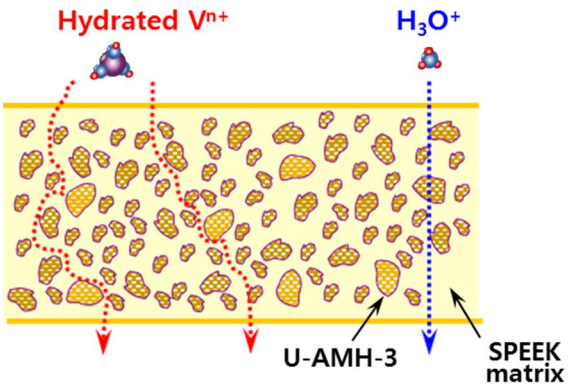

Figure VI-10. Role of the content of U-AMH-3 particles in the vanadium crossover through SU composite membranes.

To explore the possibility of using certain membranes in a VRB system, the membranes are usually evaluated in terms of the selectivity, which is defined as the ratio of proton conductivity to vanadium permeability. Generally, membranes with higher selectivities are more suitable for VRBs. The selectivities of the SU1 and SU3 membranes were higher than those of N117 and SPEEK, as shown in Table VI-2. However, the SU-5 membrane exhibited the lowest selectivity among these membranes. These behaviors were due to the decrease in proton conductivity being larger than that of vanadium permeability at higher U-AMH-3 contents. The incorporation of U-AMH-3 to SPEEK effectively decreased vanadium permeability by tortuous pathway effect, whereas higher U-AMH-3 contents resulted in a significant decrease in proton conductivity due to longer proton pathways, as mentioned above. The improved selectivities of the SU1 and SU3 membranes demonstrated their potential as alternatives to N117 in VRB systems.

Table VI-2. Proton conductivity, vanadium permeability and selectivity of all membranes.

Sample	Proton conductivity ($mS\ cm^{-1}$)	Vanadium permeability ($10^{-7}\ cm^2\ min^{-1}$)	Selectivity ($10^4\ S\ min\ cm^{-3}$)
N117	49.1	30.7	1.60
SPEEK	28.9	18.0	1.61
SG1	28.1	12.6	2.23
SG3	19.7	9.6	2.05
SG5	9.5	6.1	1.56

VI-3-5. VRB single cell performance

The charge–discharge curves of VRBs assembled from N117, SPEEK, and SU membranes at 40, 60, 80, and 100 mA cm^{-2} are shown in Figure VI-11. With increasing current density, the charge–discharge capacities of the VRBs with all membranes decreased owing to the internal resistance (IR) drop and differences in capacities between VRBs increased. The VRB cell resistances calculated from IR drop values were 0.16 Ω for N117, 0.17 Ω for SPEEK, 0.12 Ω for SU1, 0.16 Ω for SU3, and 0.27 Ω for SU5. Generally, single cell performance is related to cell resistance, proton conductivity (membrane resistance), vanadium permeability, and cycle number. The highest VRB charge–discharge capacities at all current densities were achieved with SU1, which was attributed to the low cell resistance and good balance between proton conductivity and vanadium permeability in the SU1 membrane. Although the SU5 membrane exhibited the lowest vanadium permeability among all membranes tested, the charge–discharge capacities of VRB with SU5 were the lowest at all current densities owing to lower proton conductivity and larger cell resistance.

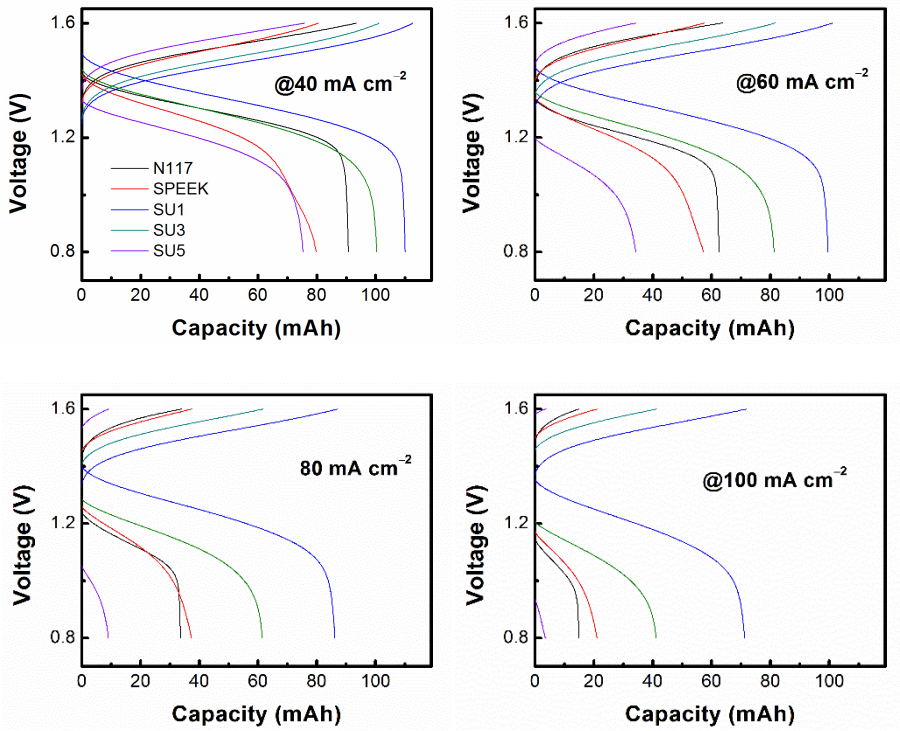

Figure VI-11. Charge–discharge curves for VRBs with N117, SPEEK, and SU membranes at 40–100 mA cm^{-2}.

Figure VI-12 shows the coulombic efficiency (CE), voltage efficiency (VE), and energy efficiency (EE) of VRBs at 40–100 mA cm^{-2} in the charge–discharge test. Regardless of the membrane used, the CE values of VRBs tended to increase with increasing current density. This was attributed to the shorter charge–discharge time, which led to less vanadium crossover during the charge–discharge process, resulting in a higher CE. The CE values of the VRBs were in the order SU5 > SU3 > SU1 > SPEEK > N117 at all current densities. The VRBs with SPEEK and SU membranes gave higher CE values than that with N117 due to lower vanadium permeability. There was a decreasing trend in VE of the VRBs with increasing current densities, owing to an increase in internal cell resistance in the VRB system. These VE values were in the order SU1 > SU3 > N117 > SPEEK > SU5 at all current densities. Despite the lower proton conductivities compared with N117, the VE values of VRBs with SU1 and SU3 were higher than that with N117. This might be due to the SU membranes (130 μm) being thinner than the N117 membranes (190 μm), resulting in smaller internal cell resistance. The VRB with SU5 gave the lowest VE, which decreased more rapidly with increasing current density than the other VRBs due to its larger cell resistance and lower proton conductivity. As shown, the EEs of VRBs with SU1 and SU3 were higher than that with N117 and SPEEK at all current densities owing to the low cell resistance and good balance between proton conductivity and vanadium

permeability, as discussed above, which demonstrated the potential for using these membranes in VRB systems.

Charge–discharge test results showed that the SU1 and SU3 membranes had good VRB single cell performance with higher charge–discharge capacity and higher cell efficiencies than N117. Therefore, to investigate the stabilities of SU1 and SU3 membranes in VRB systems, the cycle life of VRBs containing SU1, SU3, and N117 were tested at a current density of 40 mA cm^{-2}. The charge–discharge curves for these VRBs over 100 cycles are illustrated in Figure VI-13. The cell potential gap of the VRB with SU1 remained almost constant, and capacity loss in the VRB with SU3 was small compared with that with N117, indicating that the permeation of active vanadium ion species through the SU membranes was low and stable during repeated cycling. There was no decline in efficiency in the VRBs containing SU1 and SU3 after 100 cycles, as shown in Figure VI-14, meaning that these membranes were chemically stable when performing under strong acidic conditions. Figure VI-15 shows discharge capacity decline curves for VRBs during cycling. The discharge capacity decay was due to the imbalanced transfer of vanadium species, which leads to a decreased utilization ratio of vanadium species [185]. After 100 cycles, the capacity decay of VRBs containing SU1, SU3, and N117 were 25.3%, 15.3%, and 32.2%, respectively. The capacity decay rates of VRBs containing SU1 and SU3 were lower than that containing N117, indicating that SU VRBs had longer operation times

than the N117 VRB due to low and stable vanadium species crossover through the SU membranes. To summarize, the 100-cycle test confirmed that the SU membranes gave good chemical stability in strongly acidic vanadium solutions and long lifetimes suitable for application to VRBs. The costs of various membranes for VRBs are summarized in Table VI-3. Among these membranes, the SU membranes have lowest membrane cost. It can be seen that the SU membranes are also excellent in terms of cost.

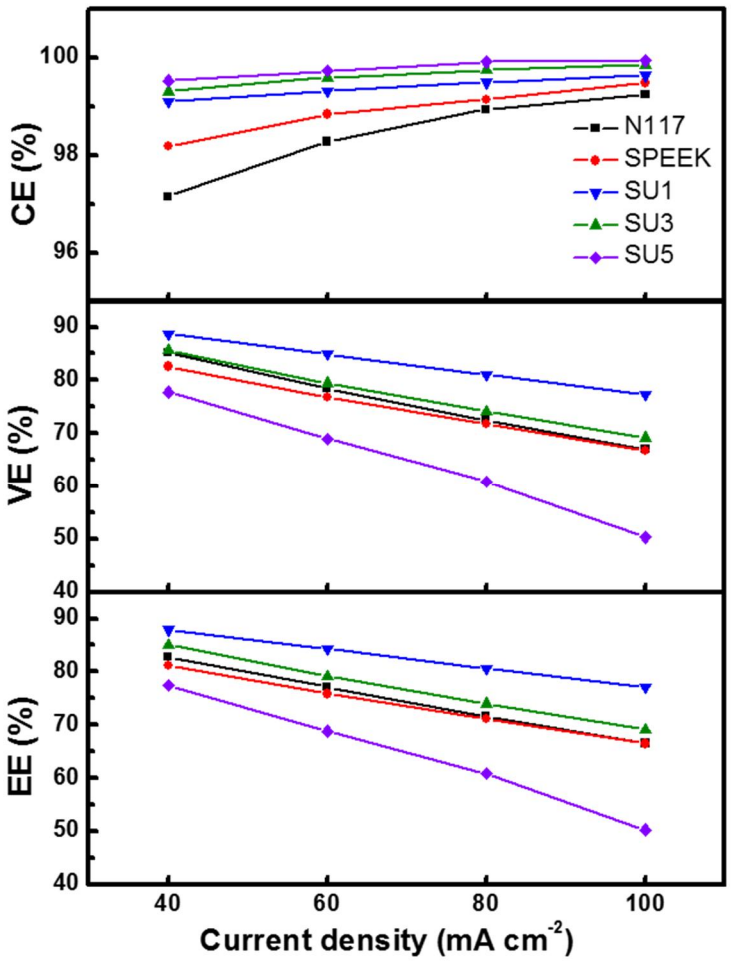

Figure VI-12. Cell efficiencies of VRBs with N117, SPEEK and SU membranes at 40–100 mA cm^{-2} in the charge–discharge test.

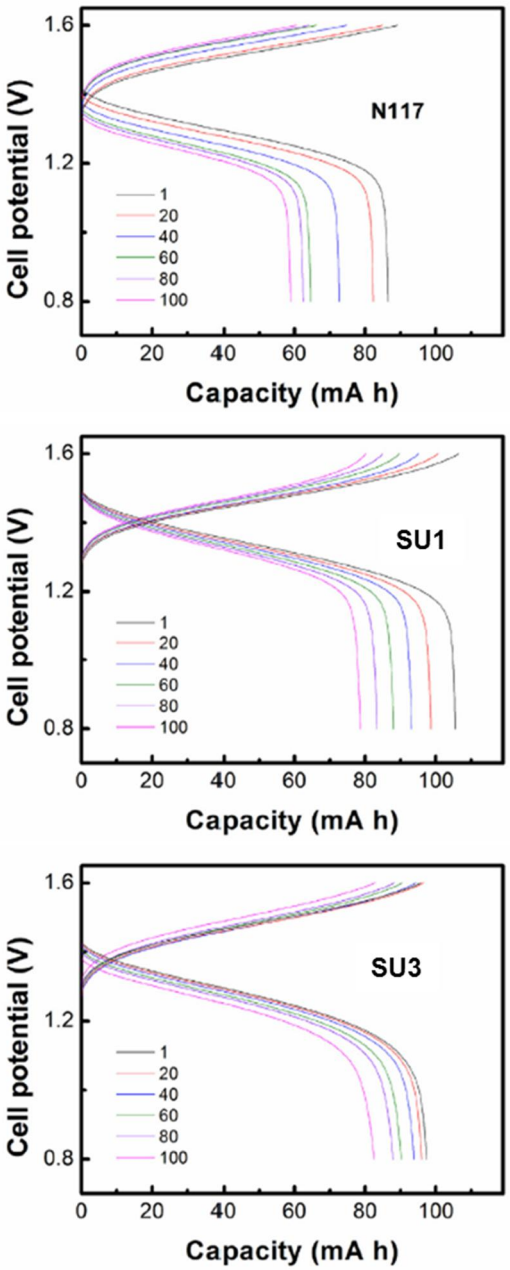

Figure VI-13. Charge–discharge curves for VRBs with N117, SU1, and SU3 membranes at 40 mA cm^{-2} over 100 cycles.

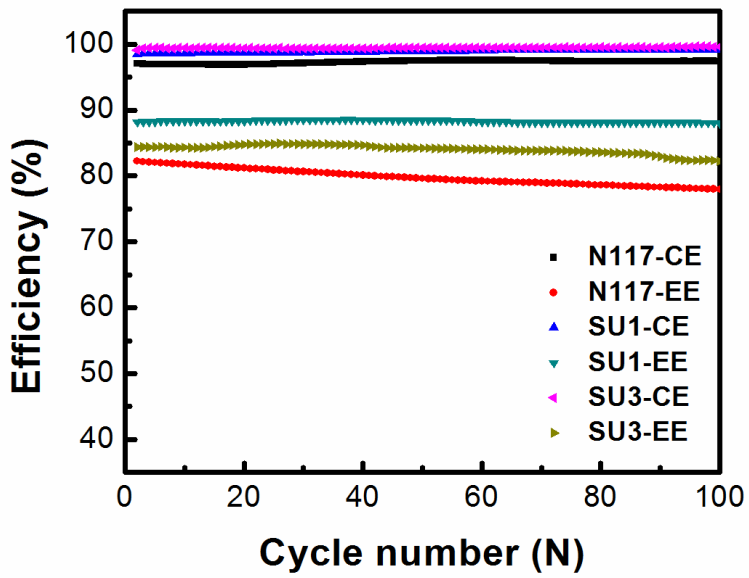

Figure VI-14. Efficiency of VRBs with N117 and SU membranes at 40 mA cm^{-2} in the cycle life test.

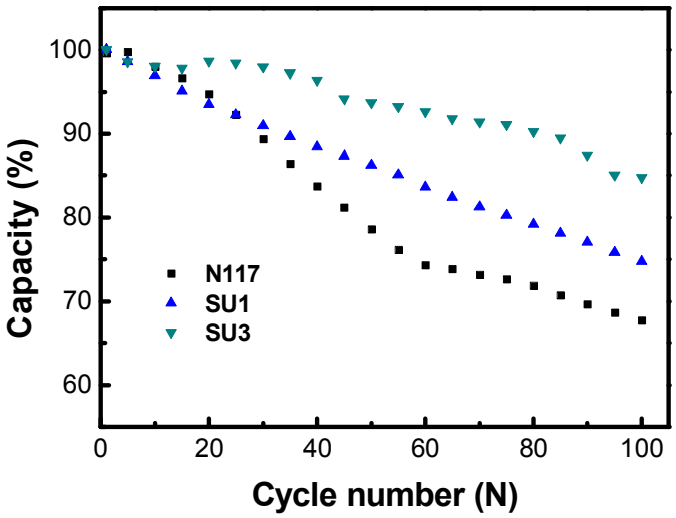

Figure VI-15. Capacitiy retention of VRBs with N117 and SU membranes at 40 mA cm^{-2} in the cycle life test.

Table VI-3. The cost of various membranes for VRBs

Membrane	Component (price)			Price (won/m^2)
Nafion 117	Membrane	1 m^2	1,700,000	1,700,000
Nafion 117/SiO_2	Membrane	1 m^2	1,700,000	1,920,000
	TEOS	2.5 L	220,000	
Nafion/D-AMH-3/Nafion (NDP in chapter V)	Membrane	40 cm^2	400,000	5,775,000
	Nafion solution dispersion	1 L	5,350,000	
	AH-AMH-3	5 g	25,000	
SPEEK/AH-AMH-3 (SU in chapter VI)	PEEK	100 g	18,000	46,000
	Sulfuric acid	2 L	10,000	
	DMF	2 L	13,000	
	AH-AMH-3	1 g	5,000	

*Excluding process cost

VI-4. Conclusion

SPEEK-based composite membranes with microporous AMH-3 were prepared by solution casting for application in a VRB system. FE-SEM analysis confirmed that the composite membranes were about 130 μm thick and that ground AMH-3 by ultrasonication method (U-AMH-3) was well dispersed in the SPEEK matrix. U-AMH-3 had effects on the membrane properties. Improved membrane performance, including swelling ratio and mechanical properties, was attributed to interactions between SPEEK and U-AMH-3. The addition of U-AMH-3 led to decrease in the proton conductivity owing to longer pathways for protons. The vanadium permeability of the composite membranes also decreased with increasing U-AMH-3 content owing to the permselective property of U-AMH-3, which resulted in improved selectivity. The optimal composite membranes exhibited high selectivity compared with N117, resulting in improved charge–discharge capacity, cell efficiency, and discharge capacity retention in VRB single cell tests. These membranes also demonstrated stable performance under VRB operating conditions over 100 cycles. Based on these results, SPEEK-based composite membranes with optimal U-AMH-3 contents show good potential for use in VRB systems.

REFERENCES AND NOTES

1. M. E. Davis, Nature 417 (2002) 813.

2. W. M. Meier, D. H. Olson, C. Baerlocher, Atlas of Zeolite Structure Types. 1996, Amsterdam: Elsevier.

3. C. T. Kresge, S. S. Dhingra, Kirk-Othmer Encyclopedia of Chemical Technology 16 (2004) 811.

4. W. Hölderich, M. Hesse, F. Näumann, Angew. Chem. Int. Ed. 27 (1988) 226.

5. L. Puppe, Chem. Unserer Zeit 4 (1986) 117.

6. D. W. Breck, Zeolite Molecular Sieves, Wiley, New York 1974.

7. R. M. Barrer, Zeoliter and Clay Minerals as Sorbents and Molecular Sieves, Academic Press, London 1978.

8. J. A. Rabo, ACS Monogr. 171 (1976) 332.

9. F. Schwochow, L. Puppe, Angew. Chern. 87 (1975) 659.

10. E. G. Derouane: Diffusional Limitations and Shape Selective Catalysis in Zeolites, Academic Press, New York, 1982, p. 101.

11. R. J. Argauer, G. R. Landolt, US-Pat. 3,702,886 (1967), Mobil Oil Corp.

12. G. T. Kokotailo, J. L. Schlenker, F. G. Dwyer, E. W. Valyocsik, Zeolites 5 (1985) 349.

13. L. M. Parker, D. M. Bibb, Zeolites 3 (1983) 8.

14. A. Araya, B. M. Lowe, Zeolites 4 (1984) 280.

15. S. A. I. Barri, G. W. Smith, D. White, D. Young, Nature 312 (1984) 533.

16. A. C. Rohrmann, Jr., R. B. La Pierre, J. L. Schlenker, J. D. Wood, E. W. Valyocsik, M. K. Rubin, J. B. Higgins, W. I. Rohrbaugh, Zeolites 5 (1985) 352.

17. P. A. Wright, J. M. Thomas, G. R. Millward, S. Ramdas, S. A. I. Barri, J. Chem. Soc. Chem. Commun. 1985, 1117.

18. M. Taramasso, G. Perego, B. Notari, US-Pat. 4410501 (August 18, 1983), Snamprogetti S.p.A.

19. E. M. Flanigen, J. H. Bennett, R. W. Grose, J. P. Cohen, R. L. Patton, R. M. Kirchner, J. V. Smith, Nature 271 (1978) 512.

20. C. C. Chu, US-Pat. 4,420,418 (1983), Mobil Oil Corp.

21. D. A. Young, US-Pat. 3,329,481, (1967), Union Oil Company of California.

22. R. Szostak, T. L. Thomas, J. Catal.100 (1986) 555.

23. R. J. Davis, Z. Liu, J. E. Tadora, W.S. Wieland, Catal. Lett. 34 (1995) 101.

24. D. M. Chapman, A. L. Roe, Zeolites 10 (1990) 730.

25. M. W. Anderson, O. Terasaki, T. Ohsuna, A. Philippou, S. P. Mackay, A. Ferreira, J. Rocha, S. Lidin, Nature 367 (1994) 347.

26. M. W. Anderson, O. Terasaki, T. Ohsuna, P. J. 0 . Malley, A. Philippou, S. P. Mackay, A. Ferreira, J. Rocha, S. Lidin, Philos. Mag. B 71 (1995) 813.

27. S. Nair, M. Tsapatsis, B. H. Toby, S. M. Kuznicki, J. Am. Chem. Soc. 123 (2001) 12781.

28. C. Braunbarth, H. W. Hillhouse, M. Tsapatsis, A. Burton, R. F. Lobo, R. M. Jacubinas, S. M. Kuznicki, Chem. Mater. 12 (2000) 1857.

29. S. Nair, H. K. Jeong, A. Chandrasekaran, C. M. Braunbarth, M. Tsapatsis, S. M. Kuznicki, Chem. Mater. 13 (2001) 4247.

30. S. M. Kuznicki, V. A. Bell, S. Nair, H. W. Hillhouse, R. M. Jacubinas, C. M. Braunbarth, B. H. Toby, M. Tsapatsis, Nature 412 (2001) 720.

31. E. Borello, C. Lamberti, S. Bordiga, A. Zecchina, C. O. Arean, Appl. Phys. Lett. 71 (1997) 2319.

32. C. Lamberti, Micropor. Mesopor. Mat. 30 (1999) 155.

33. N. Takahashi, K. Kuroda, J. Mater. Chem. 21 (2011) 14336.

34. W. Schwieger, G. Lagaly, Alkali Silicates and Crystaline Silicic Acids in Handbook of Layered Materials, Marcel Dekker, Inc., New York, 2004.

35. H. P. Eugster, Science 157 (1967) 1177.

36. K. Beneke, G. Lagaly, Am. Mineral. 68 (1983) 818.

37. R. L. Hay, Contrib. Mineral. Petrol. 17 (1968) 255.

38. K. Beneke, G. Lagaly, Am. Mineral. 62 (1977) 763.

39. W. J. Roth, D. L. Dorset, Micropor. Mesopor. Mater. 142 (2011) 32.

40. W. J. Roth, J. Čejka, Catal. Sci. Technol. 1 (2011) 43.

41. A. J. Blake, K. R. Franklin, B. M. Lowe, J. Chem. Soc., Dalton Trans. 0 (1988) 2513.

42. M. E. Leonowicz, J. A. Lawton, S. L. Lawton, M. K. Rubin, Science 264 (1994) 1910.

43. L. Schreyeck, P. Caullet, J. C. Mougenel, J. L. Guth, B. Marler, Micropor. Mesopor. Mater. 6 (1996) 259.

44. A. Corma, U. Diaz, M. E. Domine, V. Fornés, J. Am. Chem. Soc. 122 (2000) 2804.

45. A. Burton, R. J. Accardi, R. F. Lobo, M. Falcioni, M. W. Deem, Chem. Mater. 12 (2000) 2936.

46. L. D. Rollmann, J. L. Schlenker, S. L. Lawton, C. L. Kennedy, G. J. Kennedy, Micropor. Mesopor. Mater. 53 (2002) 179.

47. D. L. Dorset, G. J. Kennedy, J. Phys. Chem. B 108 (2004) 15216.

48. T. Ikeda, Y. Akiyama, Y. Oumi, A. Kawai, F. Mizukami, Angew. Chem., Int. Ed. 43 (2004) 4892.

49. R. Millini, L. C. Carluccio, A. Carati, G. Bellussi, C. Perego, G. Cruciani, S. Zanardi, Micropor. Mesopor. Mater. 74 (2004) 59.

50. S. Zanardi, A. Alberti, G. Cruciani, A. Corma, V. Fornés, M. Brunelli, Angew. Chem., Int. Ed. 43 (2004) 4933.

51. Y. X. Wang, H. Gies, J. H. Lin, Chem. Mater. 19 (2007) 4181.

52. I. Ogino, M. M. Nigra, S.-J. Hwang, J.-M. Ha, T. Rea, S. I. Zones, A. Katz, J. Am. Chem. Soc. 133 (2011) 3288.

53. M. Choi, K. Na, J. Kim, Y. Sakamoto, O. Terasaki, R. Ryoo, Nature 461 (2009) 246.

54. H.-K. Jeong, S. Nair, T. Vogt, L. C. Dickson, M. Tsapatsis, Nat. Mater. 2 (2003) 53.

55. W. Kim, S. Choi, S. Nair, Langmuir 27 (2011) 7892.

56. S. Choi, J. Coronas, J. A. Sheffel, E. Jordan, W. Oh, S. Nair, D.F. Shantz, M. Taspatsis, Micropor. Mesopor. Mater. 115 (2008) 75.

57. S. Choi, J. Coronas, E. Jordan, W. Oh, S. Nair, F. Onorato, D.F. Shantz, M. Tsapatsis, Angew. Chem. Int. Ed. 47 (2008) 552.

58. S. S. Ray, M. Okamoto, Prog. Polym. Sci. 28 (2003) 1539.

59. S. Varghese, J. Karger-Kocsis, Polymer 44 (2003) 4921.

60. S. J. Ahmadi, Y. D. Huang, W. Li, J. Mater. Sci. 39 (2004) 1919.

61. K. Ikeda, Y. Kawamura, T. Yamamoto, M. Iwamoto, Catal. Commun. 9 (2008) 106.

62. S. Pavlidou, C. D. Papaspyrides, Prog. Polym. Sci. 33 (2008) 1119.

63. B. Royer, N. F. Cardoso, E. C. Lima, T. R. Macedo, C. Airoldi, J. Hazard. Mater. 181 (2010) 366.

64. Y. Ide, N. Ochi, M. Ogawa, Angew. Chem. 123 (2011) 680.

65. Y. Ide, S. Iwasaki, M. Ogawa, Langmuir 27 (2011) 2522.

66. S. Nair, Z. Chowdhuri, I. Peral, D. A. Neumann, L. C. Dickinson, G. Tompsett, H.-K. Jeong, M. Tsapatsis, Phys. Rev. B 71 (2005) 104301.

67. S. Ramdas, J. Klinowski, Nature 308 (1984) 521.

68. E. Geidel, H. Sohlig, C. Peuker, and W. Pilz, in Studies on Surface Science and Catalysis, edited by G. Ohlmann, H. Pfeifer, and R. Fricke (Elsevier, Amsterdam, 1991), p. 511.

69. W. Kim, J. S. Lee, D. G. Bucknall, W. J. Koros, S. Nair, J. Membr. Sci. 441 (2013) 129.

70. Y. Hudiono, S. Choi, S. Shu, W. J. Koros, M. Tsapatsis, S. Nair, Micropor. Mesopor. Mat. 118 (2009) 427.

71. W. Stumm, J. J. Morgan, Aquatic Chemistry: Chemical Equilibria and Rates in Natural Waters, 3rd ed., John Wiley & Sons, Inc., New York, 1996.

72. K. N. Han, B. Y. Yu, S.-Y. Kwak, J. Membr. Sci. 396 (2012) 83.

73. U. Kumar, Sci. Res. Essays 1 (2006) 033.

74. M. Islam, R. Patel, J. Hazard. Mater. 172 (2009) 707.

75. G.-T. Wei, Z. Yang, C.-J. Chen, Anal. Chim. Acta 488 (2003) 183.

76. N. Abdullah, R. J. Gohari, N. Yusof, A. F. Ismail, J. Juhana, W. J. Lau, T. Matsuura, Chem. Eng. J. 289 (2016) 28.

77. R. Rojas, Appl. Clay Sci. 87 (2014) 254.
78. M. Zhang, Chem. Eng. J. 172 (2011) 361.
79. C. A. Christophi, L. Axe, J. Environ. Eng. 126 (2000) 66.
80. Z. Wang, Y. Feng, X. Hao, W. Huang, G. Guan, A. Abudula, J. Hazard. Mater. 274 (2014) 436.
81. A. H. Ören, A. Kaya, J. Hazard. Mater. B131 (2006) 59.
82. M. Al-Anber, Z. A. Al-Anber, Desalination 225 (2008) 70.
83. K. S. Hui, C. Y. H. Chao, S. C. Kot, J. Hazard. Mater. B127 (2005) 89.
84. J. Kim, M. Choi, R. Ryoo, J. Catal. 269 (2010) 219.
85. Q. Guo, F. Fan, E. A. Pidko, W. N. P. Van Der Graaff, Z. Feng, C. Li, E. J. M. Hensen, ChemSusChem 6 (2013) 1352.
86. J.-Y. Luo, H. Oh, C. Henry, W. Epling, Appl. Catal. B: Environ. 123–124 (2012) 296.
87. S. Teketel, U. Olsbye, K. P. Lillerud, P. Beato, S. Svelle, Appl. Catal. A: Gen. 494 (2015) 68.
88. M. Kuronen, M. Weller, R. Townsend, R. Harjula, React. Funct. Polym. 66 (2006) 1350.
89. D. Karadag, Y. Koc, M. Turan, M. Ozturk, J. Hazard. Mater. 144 (2007) 432.
90. W. Mozgawa, M. Król, W. Pichór, J. Hazard. Mater. 168 (2009) 1482.
91. S.-Y. Jeong, J.-M. Lee, Bull. Korean Chem. Soc. 19 (1998) 218.
92. S.-H. Lin, R.-S. Juang, J. Hazard. Mater. B92 (2002) 315.

93. R. Say, E. Birlik, A. Denizli, A. Ersöz, Appl. Clay Sci. 31 (2006) 298.

94. A. Shahbazi, H. Younesi, A. Badiei, Chem. Eng. J. 168 (2011) 505.

95. A. M. El-Toni, M. A. Habila, M. A. Ibrahim, J. P. Labis, Z. A. ALOthman, Chem. Eng. J. 251 (2014) 441.

96. G. Mohammadnezhad, M. Dinari, R. Soltani, New J. Chem. 40 (2016) 3612.

97. M. Dinari, G. Mohammadnezhad, R. Soltani, RSC Adv. 6 (2016) 11419.

98. G. E. Boyd, A. W. Adamson, L. S. Meyers, J. Am. Chem. Soc. 69 (1947) 2836.

99. D. Reichenberg, J. Am. Chem. Soc. 75 (1953) 589.

100. D. Mohan, K. P. Singh, Water Res. 36 (2002) 2304.

101. F. Helfferich, Ion-Exchange, McGraw–Hill, New York, 1962.

102. M. A. S. D. Barros, P. A. Arroyo, Adsorption 10 (2004) 227.

103. D. Mohan, V. K. Gupta, S. K. Srivastava, S. Chander, Colloid Surf. A-Physicochem. Eng. Asp. 177 (2001) 169.

104. D. Yang, Z. Zheng, H. Liu, H. Zhu, X. Ke, Y. Xu, D. Wu, Y. Sun, J. Phys. Chem. C 112 (2008) 16275.

105. M. Dakiky, M. Khamis, A. Manassra, M. Mer'eb, Adv. Environ. Res. 6 (2002) 533.

106. H. K. An, B. Y. Park, D. S. Kim, Wat. Res. 35 (2001) 3551.

107. Y.-H. Li, J. Ding, Z. Luan, Z. Di, Y. Zhu, C. Xu, D. Wu, B. Wei,

Carbon 41 (2003) 2787.

108. Z. Reddad, C. Gerente, Y. Andres, P. L. Cloirec, Environ. Sci. Technol. 36 (2002) 2067.

109. F. An, B. Gao, X. Dai, M. Wang, X. Wang, J. Hazard. Mater. 192 (2011) 956.

110. F. Ge, M.-M. Li, H. Ye, B.-X. Zhao, J. Hazard. Mater. 211–212 (2012) 366.

111. Q. Zhu, Z. Li, Chem. Eng. J. 281 (2015) 69.

112. M. Sprynskyy, B. Buszewski, A. P. Terzyk, J. Namieśnik, J. Colloid Interf. Sci. 304 (2006) 21.

113. H. M. Baker, A. M. Massadeh, H. A. Younes, Environ. Monit. Assess. 157 (2009) 319.

114. L.-Y. Jiang, C.-M., Leu, K.-H. Wei, Adv. Mater. 14 (2002) 426–429.

115. A. Kuhlmann, F. Roessner, W. Schwieger, O. Gravenhorst, T. Selvam, Catal. Today 97 (2004) 303.

116. L. Xu, H. Nakajima, E. Manias, R. Krishnamoorti, Macromolecules 42 (2009) 3795.

117. Y. Hudiono, S. Choi, S. Shu, W.J. Koros, M. Tsapatsis, S. Nair, Micropor. Mesopor. Mater. 118 (2009) 427.

118. M.A. Vicente, M. Suárez, J.D.D. López-González, M.A. Bañares-

Muñoz, Langmuir 12 (1996) 566.

119. C.-C. Tsai, H. Teng, Chem. Mat. 18 (2006) 367.

120. T. Ikeda, M. Uenaka, K. Komura, Y. Sugi, Chem. Lett. 39 (2010) 747.

121. K.S.W. Sing, D.H. Everett, R.A.W. Haul, L. Moscou, R.A. Pierotti, J. Rouquérol, T. Siemieniewska, Pure & Appl. Chem. 57 (1985) 603.

122. G.J. Wilson, A.S. Matijasevich, D.R.G. Mitchell, Jamie C. Schulz, G.D. Will, Langmuir 22 (2006) 2016.

123. S. Nazarenko, P. Meneghetti, P. Julmon, B.G. Olson, S. Qutubuddin, J. Polym. Sci. Part B: Polym. Phys. 45 (2007) 1733.

124. R.A. Vaia, W. Liu, J. Polym. Sci. Part B: Polym. Phys. 40 (2002) 1590.

125. B. Dunn, H. Kamath, J.-M. Tarascon, Science 18 (2011) 928

126. S. Chu, A. Majumdar, Nature 488 (2012) 294.

127. W. Wang, Q. Luo, B. Li, X. Wei, L. Li, Z. Yang, Adv. Funct. Mater 23 (2013) 970.

128. M. Rychcik, M. Skyllas-Kazacos, J. Power Sources 22 (1988) 59.

129. C. Ding, H. Zhang, X. Li, T. Liu, F. Xing, J. Phys. Chem. Lett. 4 (2013) 1281.

130. Z. Yang, J. Zhang, M. C. W. Kintner-Meyer, X. Lu, D. Choi, J. P. Lemmon, J. Liu, Chem. Rev. 111 (2011) 3577.

131. M. Skyllas-Kazacos, M. H. Chakrabarti, S. A. Hajimolana, F. S. Mjalli, M. Saleem, J. Electrochem. Soc. 158 (2011) R55.

132. P. Zhao , H. M. Zhang , H. Zhou , J. Chan , S. Gao , B. L. Yi , J. Power Sources 162 (2006) 1416.

133. H. Prifti, A. Parasuraman, S. Winardi, T. M. Lim, M. Skyllas-Kazacos, Membranes 2 (2012) 275.

134. X. Li, H. Zhang, Z. Mai, H. Zhang, I. Vanelecom, Energy Environ. Sci. 4 (2011) 1147.

135. H. Dai, H. Zhang, H. Zhong, X. Li, S. Xiao, Z. Mai, Int. J. Hydrog. Energy 35 (2010) 4209.

136. T. Mohammadi, M. Skyllas-Kazacos, J. Appl. Electrochem. 27 (1997) 153.

137. H. Zhang, H. Zhang, X. Li, Z. Mai, J. Zhang, Energy Environ. Sci. 4 (2011) 1676.

138. J. Xi, Z. Wu, X. Teng, Y. Zhao, L. Chen, X. Qiu, J. Mater. Chem. 18 (2008) 1232.

139. J. Xi, Z. Wu, X. Qiu, L. Chen, J. Power Sources 166 (2007) 531.

140. X. Teng, Y. Zhao, J. Xi, Z. Wu, X. Qiu, L. Chen, J. Membr. Sci. 341 (2009) 149.

141. X. Teng, Y. Zhao, J. Xi, Z. Wu, X. Qiu, L. Chen, J. Power Sources 189 (2009) 1240.

142. Q. Luo, H. Zhang, J. Chen, D. You, C. Sun, Y. Zhang, J. Membr. Sci. 325 (2008) 553.

143. X. Teng, C. Sun, J. Dai, H. Liu, J. Su, F. Li, Electrochim. Acta 88 (2013) 725.

144. X. Teng, J. Dai, J. Su, Y. Zhu, H. Liu, Z. Song, J. Power Sources 240 (2013) 131.

145. S. Choi, J. Coronas, Z. Lai, D. Yust, F. Onorato, M. Tsapatsis, J. Membrane Sci. 316 (2008) 145.

146. W.-G. Kim, J. Lee, D. G. Bucknall, W. J. Koros, S. Nair, J. Membrane Sci. 441 (2013) 129.

147. J. Kim, J.-D. Jeon, S.-Y. Kwak, Micropor. Mesopor. Mater. 168 (2013) 148.

148. S. Slade, S.A. Campbell, T. R. Ralph, F. C. Walsh, J. Electrochem. Soc. 149 (2002) A1556.

149. D. Chen, M. A. Hickner, E. Agar, E. C. Kumbur, J. Membrane Sci. 437 (2013) 108.

150. K.-L. Huang, X.-g. Li, S.-q. Liu, N. Tan, L.-q. Chen, Renew. Energ. 33 (2008) 186.

151. M. Kazacos, M. Skyllas-Kazacos, J. Electrochem. Soc. 136 (1989) 2759.

152. Y. Wang, S. Wang, M. Xiao, D. Han, Y. Meng, Int. J. Hydrogen Energ. 39 (2014) 16088.

153. D. Chen, S. Kim, V. Sprenkle, M. A. Hickner, J. Power Sources 231 (2013) 301.

154. F. Wang, J. M. Sylvia, M. M. Jacob, D. Peramunage, J. Power Sources 242 (2013) 575.

155. X. Ling, C. Jia, J. Liu, C. Yan, J. Membr. Sci. 415–416 (2012) 306.

156. Z. Li, L. Liu, L. Yu, L. Wang, J. Xi, X. Qiu, L. Chen, J. Power Sources 272 (2014) 427.

157. S. Liu, L. Wang, Y. Ding, B. Liu, X. Han, Y. Song, Electrochim. Acta 130 (2014) 90.

158. W. Dai, Y. Shen, Z. Li, L. Yu, J. Xi, X. Qiu, J. Mater. Chem. A 2 (2014) 12423.

159. W. Dai, L. Yu, Z. Li, J. Yan, L. Liu, J. Xi, X. Qiu, Electrochim. Acta 132 (2014) 200.

160. Z. Li, W. Dai, L. Yu, J. Xi, X. Qiu, L. Chen, J. Power Sources 257 (2014) 221.

161. S. Winardi, S. C. Raghu, M O. Oo, Q. Yan, N. Wai, T. M. Lim, M. Skyllas-Kazacos, J. Membr. Sci. 450 (2014) 313.

162. J. Xi, Z. Li, L. Yu, B. Yin, L. Wang, L. Liu, X. Qiu, L. Chen, J. Power Sources 285 (2015) 195.

163. J. Xi, W. Dai, L. Yu, RSC Adv. 5 (2015) 33400.

164. H.-Y. Jung, S. Jeong, Y. Kwon, J. Electrochem. Soc. 163 (2016) A5090.

165. C. Jia, Y. Cheng, X. Ling, G. Wei, J. Liu, C. Yan, Electrochim. Acta 153 (2015) 44.

166. B. Yin, L. Yu, B. Jiang, L. Wang, J. Xi, J. Solid State Electrochem. 20

(2016) 1271.

167. S. Park, H. Kim, J. Electrochem. Soc. 163 (2016) A2293.

168. L. Zhao, F. Li, Y. Guo, Y. Dong, J. Liu, Y. Wang, J. Kang, G. Zhou, Q. Liu, High Perform. Polym. 29 (2017) 127.

169. J. Pan, S. Wang, M. Xiao, M. Hickner, Y. Meng, J. Membr. Sci. 443 (2013) 19.

170. N. Wang, S. Peng, H. Wang, Y. Li, S. Liu, Y. Liu, Electrochem. Commun. 17 (2012) 30.

171. Z. Mai, H. Zhang, X. Li, C. Bi, H. Dai, J. Power Sources 196 (2011) 482.

172. D. Chen, S. Wang, M. Xiao, Y. Meng, Energy Environ. Sci. 3 (2010) 622.

173. D. Chen, M. A. Hickner, E. Agar, E. C. Kumbur, J. Membr. Sci. 437 (2013) 108.

174. S. Kim, J. Yan, B. Schwenzer, J. Zhang, L. Li, J. Liu, Z. Yang, M. A. Hickner, Electrochem. Commun. 12 (2010) 1650.

175. P. Krishnan, J.-S. Park, T.-H. Yang, W.-Y. Lee, C.-S. Kim, J. Power Sources 163 (2006) 2.

176. Z. Yuan, X. Zhu, M. Li, W. Lu, X. Li, H. Zhang, Angew. Chem. Int. Ed. 55 (2016) 3058.

177. Z. Chen, B. Holmberg, W. Li, X. Wang, W. Deng, R. Munoz, Y. Yan, Chem. Mater. 18 (2006) 5669.

178. X. Li, E. P. L. Roberts, S. M. Holmes, V. Zholobenko, Solid State Ionics 178 (2007) 1248.

179. H. Wu, B. Zheng, X. Zheng, J. Wang, W. Yuan, Z. Jiang, J. Power Sources 173 (2007) 842.

180. J. Wang, X. Zheng, H. Wu, B. Zheng, Z. Jiang, X. Hao, B. Wang, J. Power Sources 178 (2008) 9.

181. J. Kim, J.-D. Jeon, S.-Y. Kwak, Micropor. Mesopor. Mat. 168 (2013) 148.

182. J. Kim, J.-D. Jeon, S.-Y. Kwak, Electrochem. Commun. 38 (2014) 68.

183. J.-D. Jeon, J. Kim, S.-Y. Kwak, J. Membr. Sci. 415–416 (2012) 353.

184. E. Şengül, H. Erdener, R. G. Akay, H. Yücel, N. Baç, İ. Eroğlu, Int. J. Hydrogen Energ. 34 (2009) 4645.

185. B. Li, Q. Luo, X. Wei, Z. Nie, E. Thomsen, B. Chen, V. Sprenkle, W. Wang, ChemSusChem 7 (2014) 577.

KOREAN ABSTRACT

미세다공성 물질은 표면뿐만 아니라 물질의 전체에 걸쳐 원자, 이온 및 분자와 상호 작용할 수 있기 때문에 큰 관심을 끌고 있다. 미세다공성 물질의 유용성은 미세한 구조 (기공 크기, 분포, 모양, 부피)에 의해 나타나는데 이러한 구조로 인해 분자가 촉매 활성 및 흡착 능력을 향상시키는 큰 내부 표면 및 공동에 접근할 수 있게 한다. 이에 따라 미세다공성 물질은 촉매, 흡착제, 분자체와 같은 다양한 응용 분야에서 널리 사용된다.

AMH-3는 실리케이트 층과 Sr, Na 양이온 및 물 분자가 차지하는 층간 공간으로 구성된 층상 미세다공성 물질이다. AMH-3는 층의 평면뿐만 아니라 실리케이트 층의 두께를 따라 존재하는 8원자 고리(8-MR) 공간으로 인한 미세다공성을 갖는 최초의 층상 실리케이트이다. 이러한 구조로 인해 AMH-3는 3차원 미세다공성을 가지며 제올라이트처럼 산, 화학 및 열에 대한 안정성이 우수하며 층상 실리케이트와 같이 인터칼레이션, 필링 및 박리를 할 수 있다.

AMH-3의 합성과 특성 분석 및 이의 합성 메커니즘 연구가 수행되었다. AMH-3를 특성 분석하기 위해 전계 방출 주사 전자 현미경 (FE-SEM), X-선 회절 (XRD), ^{29}Si 고체 핵 자기 공명 (MAS

NMR), 푸리에 변환 적외선 (FT-IR) 및 라만 분광법을 사용하였다. AMH-3의 합성 메커니즘에 대한 합리적인 모델을 실험 결과에 근거하여 제안하였다. AMH-3 합성 과정에서 스트론튬과 티타늄은 각각 구조화제와 연결제로 작용한다.

AMH-3의 이온 교환 거동과 AMH-3에 의한 수용액에 존재하는 중금속의 제거가 처음으로 연구되었다. AMH-3와 이온 교환된 AMH-3는 ICP-AES, FE-SEM, ^{29}Si CP MAS NMR 및 XRD로 분석하였다. 이온 교환 거동에 관한 연구들로 AMH-3에 의한 이온의 흡착은 표면 흡착보다 이온 교환에 의한 것이며, 이온 교환 동안 AMH-3의 구조에는 큰 변화가 발생하지 않다는 것을 밝혔다. 수용액으로부터 다양한 중금속 이온 (Pb^{2+}, Cu^{2+}, Cd^{2+}, Zn^{2+})을 AMH-3으로 제거하는 것은 배치 방법을 사용하여 수행되었다. 초기 이온 농도 및 접촉 시간과 같은 영향력 있는 매개 변수가 흡착 과정에 미치는 영향을 연구하였다. 중금속 이온 흡착능 및 제거 효율은 주로 AMH-3의 유효 기공 크기와 금속 이온의 수화된 반경의 차이에 의한 것임을 확인하였다. 흡착 등온선 결과는 랭미어(Pb^{2+}, Cu^{2+}, Zn^{2+})와 프로인틀리히(Cd^{2+}) 모델에 잘 맞는 것을 확인하였다. 흡착 속도 결과는 슈도 2차 동역학 모델에 잘 맞는 것을 확인하였다. 경쟁적 흡착 실험은 Pb^{2+}> Cu^{2+}> Zn^{2+}> Cd^{2+}의 금속 이온 친화성의 순서를

나타냈었다. 이러한 결과는 AMH-3가 수용액에서 중금속을 효율적이고 선택적으로 제거하는 데 적합하다 할 수 있다.

선택적 투과용 필러로 사용하기 위해서는, 층 내부 및 층간 공간에 위치한 Na^+ 및 Sr^{2+} 양이온을 제거하여 미세기공을 활성화하고 층 분리를 해야 한다. 팽창제(swelling agent)를 사용하지 않고 산-열수 처리에 의해 층 분리된 AMH-3을 성공적으로 얻었다. 층 분리를 위한 산-열수 조건은 최적의 선택적 투과용 필러로 사용하기 위한 모폴로지를 갖기 위해 최적화하였다. AMH-3 및 층 분리 된 AMH-3는 FE-SEM, N_2 흡착, ICP-AES, ^{29}Si MAS NMR, FT-IR, Raman 및 XRD 등으로 분석하였다. 이러한 결과는 층 분리된 AMH-3가 원래의 AMH-3보다 규칙적인 기공 구조를 가지고 있으며 AMH-3의 기공 층에서 결정성을 유지한다는 것을 확인하였다.

활성화 미세기공을 가진 AMH-3을 사용하여 바나듐 레독스 흐름 전지(VRB)에 사용하기 위해 낮은 바나듐 크로스 오버를 갖는 이온 교환막을 개발하고자 했다. 층 분리 된 AMH-3 (D-AMH-3) 층을 갖는 나피온계 복합 막은 용액 주조 및 고온 가압에 의해 제조되었다. 막의 구조는 FE-SEM과 EDS로 분석하였으며 복합막은 이중 나피온 외층과 중심 D-AMH-3 층을 포함하는 샌드위치형

구조임을 확인하였다. 나피온/DAMH-3 막은 VRB 적용을 위한 이온 교환막으로 사용되었으며, 바나듐 투과도와 단일 셀 성능으로 평가되었다. 나피온/D-AMH-3 복합막은 기존 나피온에 비해 낮은 바나듐 투과도를 나타내어 더 높은 쿨롱 효율과 사이클 당 낮은 용량 손실을 보였다. D-AMH-3 층이 바나듐 혼합을 감소시키고 전지 성능을 향상시키는 선택적 투과용 필러로서 잠재적으로 적합함을 나타내었다.

Sulfonated poly (ether ether ketone) (SPEEK)는 VRB의 나피온을 대체할 수 있는 가능성이 높은 고분자이다. 그러나 높은 술폰화도의 SPEEK는 높은 팽창율, 낮은 기계적 안정성 및 높은 바나듐 투과도를 나타낸다. 본 연구에서는 막 성능을 향상시키기 위해 SPEEK와 초음파 처리 된 D-AMH-3 (U-AMH-3)의 복합막을 다양한 U-AMH-3 함량으로 제조하여 연구하였다. 이러한 SPEEK/U-AMH-3 복합막의 물리·화학적 및 기계적 특성, 바나듐 투과도 및 VRB 단일 셀 성능은 다양한 분석 기술을 사용하여 평가하였다. SPEEK와 U-AMH-3 사이의 상호 작용 및 U-AMH-3의 선택 투과성 특성은 복합막이 우수한 기계적 성질 및 낮은 바나듐 투과도를 나타내는 결과를 가져온다. 최적의 복합막은 나피온을 사용하는 것보다 높은 충·방전 용량, 더 높은 전지 효율 및 더 우수한 용량 보존율을 갖는

것으로 확인되었다. 이러한 결과는 향상된 막 성능, 낮은 바나듐 투과도 및 좋은 단일 셀 성능을 갖는 SPEEK계 복합막이 U-AMH-3을 복합함으로써 성공적으로 제조되었음을 나타낸다.

주요어: 미세다공성, 층상 실리케이트, AMH-3, 이온 교환, 흡착제, 중금속 이온, 이온 수송, 바나듐 레독스 흐름 전지

학번: 2008-22839

LIST OF PAPERS and PATENTS

PAPERS

1. J.-D. Jeon, J. Kim, S.-Y. Kwak, J. Membr. Sci. 415–416 (2012) 353–359.

2. J. Kim, J.-D. Jeon, S.-Y. Kwak, Micropor. Mesopor. Mat. 16 (2013) 148–154.

3. J. Kim, J.-D. Jeon, S.-Y. Kwak, Electrochem. Commun. 38 (2014) 68–70.

4. J. Kim, S. Yeo, J.-D. Jeon, S.-Y. Kwak, Micropor. Mesopor. Mat. 202 (2015) 8–15.

5. J. Kim, S. Oh, S.-Y. Kwak, Chem. Eng. J. 281 (2015) 541–548.

6. J. Kim, S.-Y. Kwak, Chem. Eng. J. 313 (2017) 975–982.

7. J. Kim, J.-D. Jeon, S.-Y. Kwak, Electrochim. Acta. 243 (2017) 220–227.

8. J. Kim, Y. Lee, J.-D. Jeon, S.-Y. Kwak, J. Power Sources, under revision.

PATENTS

1. 곽승엽, 김지훈, "선택적 투과가 가능한 박리된 미세다공성 층상 실리케이트 입자가 적층된 직접메탄올 연료전지용 고분자 전해질막 및 그 제조방법과 이를 사용하는 막전극 접합체 및 직접메탄올 연료전지", 대한민국 특허출원번호 10-2012-0020384 (2012. 2. 28)

2. 곽승엽, 김지훈, "미세 다공성 층상 실리케이트 입자층을 갖는 바나듐 레독스 흐름 전지용 이온교환막, 그의 제조방법 및 그를 포함하는 바나듐 레독스 흐름 전지", 대한민국 특허등록번호 10-1662647 (2016. 9. 28)